

CONTRACTOR REPORT

SAND87 — 7098
Unlimited Release
UC — 63

8024

65472

C1

Development of a Thin AlGaAs Solar Cell



8232-2//065472



00000001 -

SPIRE Corporation
Patriots Park
Bedford, MA 01730

Prepared by Sandia National Laboratories Albuquerque, New Mexico 87185
and Livermore, California 94550 for the United States Department of Energy
under Contract DE-AC04-76DP00789

Printed April 1987

Issued by Sandia National Laboratories, operated for the United States Department of Energy by Sandia Corporation.

NOTICE: This report was prepared as an account of work sponsored by an agency of the United States Government. Neither the United States Government nor any agency thereof, nor any of their employees, nor any of their contractors, subcontractors, or their employees, makes any warranty, express or implied, or assumes any legal liability or responsibility for the accuracy, completeness, or usefulness of any information, apparatus, product, or process disclosed, or represents that its use would not infringe privately owned rights. Reference herein to any specific commercial product, process, or service by trade name, trademark, manufacturer, or otherwise, does not necessarily constitute or imply its endorsement, recommendation, or favoring by the United States Government, any agency thereof or any of their contractors or subcontractors. The views and opinions expressed herein do not necessarily state or reflect those of the United States Government, any agency thereof or any of their contractors or subcontractors.

Printed in the United States of America
Available from
National Technical Information Service
U.S. Department of Commerce
5285 Port Royal Road
Springfield, VA 22161

NTIS price codes
Printed copy: A04
Microfiche copy: A01

SAND87-7098
Unlimited Release
Printed April 1987

Distribution
Category UC-63

Development of a Thin AlGaAs Solar Cell

SPIRE Corporation
Patriots Park
Bedford, MA 01730

Sandia Contract No. 47-2071

Abstract

The objective of this work was the production of ultrathin 1.7 eV top cells for a mechanical tandem stack with silicon bottom cells. The unique aspect of our work was MOCVD growth of the AlGaAs cell on a germanium substrate, subsequently completely removed by selective etching. Important results include the identification of Ge autodoping and unintentional tandem cell formation (p-n junction formation in the Ge substrate) as materials-related problems. The former was solved by GaAs backside capping of the Ge, and the latter was obviated by substrate removal. A process for bonding to a glass superstrate, substrate removal by etching, and application of a back contact grid was developed. Working solar cells of GaAs and AlGaAs with thicknesses of 5 microns have been demonstrated.

TABLE OF CONTENTS

<u>Section</u>	<u>Page</u>
Table of Contents	v
List of Illustrations	vi
List of Tables	vii
 1 INTRODUCTION	 1-1
1.1 Background and Motivation	1-1
1.2 Statement of Work	1-2
1.3 Organization of This Report	1-4
 2 MATERIALS DEVELOPMENT.	 2-1
2.1 MOCVD System.	2-1
2.2 Material Characterization	2-2
2.3 GaAs Cells on GaAs Substrates	2-4
2.4 AlGaAs Cells on GaAs Substrates	2-8
2.5 GaAs and AlGaAs Cells on Ge Substrates	2-14
2.5.1 Ge Substrate Preparation	2-16
2.5.2 Ge Autodoping	2-17
2.5.3 Unintentional Tandem Cell Formation	2-25
2.5.4 Defect Structure in Epitaxial Layers on Ge	2-31
 3 PROCESS DEVELOPMENT	 3-1
3.1 Concentrator Cell Grid Design	3-1
3.2 Concentrator Cell Front Side Processing	3-3
3.3 Ge Substrate Removal	3-4
3.4 Back Side Processing of Thin Cells	3-6
 4 TEST RESULTS	 4-1
4.1 GaAs Cells on GaAs Substrates	4-1
4.2 GaAs Cells on Ge Substrates	4-4
4.3 AlGaAs Cells on GaAs Substrates	4-9
4.4 AlGaAs Cells on Ge Substrates	4-16
4.5 Thin GaAs Cells	4-20
4.6 Thin AlGaAs Cells	4-25
 5 CONCLUSIONS	 5-1
 6 PROBLEM AREAS AND AREAS FOR FUTURE WORK	 6-1
 7 ACKNOWLEDGEMENTS	 7-1
 8 APPENDIX A: CONCENTRATOR CELL GRID DESIGN	 A-1
 9 REFERENCES	 R-1

LIST OF ILLUSTRATIONS

<u>Figures</u>	<u>Page</u>
1 Photograph of the SPI-MO CVD 450 reactor	2-3
2 Schematic of the SPI-MO CVD 450 reactor system.	2-3
3 SIMS profiles of (a) Zn and (b) Si dopants in an AlGaAs Solar Cell	2-5
4 SIMS profiles of (a) O and (b) C impurities in the AlGaAs cell of Figure 3.	2-6
5 Comparison of SIMS and Polaron measurements	2-6
6 Layer structures of the four solar cell/substrate combinations investigated	2-7
7 SIMS depth profile of oxygen in an AlGaAs solar cell, run 627	2-9
8 Oxygen concentration as a function of aluminum content in AlGaAs layers	2-8
9 AlGaAs J_{SC} as a function of oxygen impurity concentration.	2-11
10 AlGaAs solar cell J_{SC} as a function of run number.	2-13
11 Comparison of SIMS oxygen profiles for good and bad regions of an AlGaAs solar cell wafer.	2-15
12 Polaron profiles of autodoping in GaAs layers grown on Ge substrates.	2-19
13 Ge autodoping and interface trap density as a function of growth temperature.	2-20
14 Polaron profiles of GaAs layers grown on Ge wafers at (a) 650° (b) 700°	2-21
15 Ge autodoping as a function of temperature	2-23

LIST OF ILLUSTRATIONS

<u>Figures</u>	<u>Page</u>
16 SIMS profiles of Ge in AlGaAs solar cells grown on (a) Ge (b) GaAs	2-24
17 Doping profile in a Ge substrate after growth of a 5 micron GaAs layer at 650°C	2-27
18 Doping profile in a Ge substrate after growth of a GaAs solar cell at 700°C	2-28
19 Doping profile in a Ge substrate after growth of an AlGaAs solar cell at 800°C	2-29
20 Material properties of Ga and As in Ge as a function of temperature	2-30
21 TEM micrograph of an isolated threading dislocation in GaAs grown on Ge	2-32
22 Photograph of the 1 cm diameter grid pattern on a thin AlGaAs cell	3-2
23 Grid shadow loss as a function of line width.	3-5
24 GaAs one-sun cell with efficiency of 20.3%	4-2
25 Internal quantum efficiency for a GaAs concentrator cell.	4-3
26 Comparison of GaAs solar cells grown on GaAs and Ge	4-5
27 Log I-V for the solar cells of Figure 26	4-6
28 3-terminal cell structure used for GaAs cells on Ge	4-7
29 Efficiency vs. concentration for AlGaAs cell 628B-S2A	4-10
30 Open circuit voltage vs. concentration for 628B-S2A	4-11
31 Fill factor vs. concentration for AlGaAs cell 628B-S2A	4-12
32 Log I-V of cell 628B-S2A	4-12
33 Open circuit voltage vs. concentration for 628B-S2A	4-13
34 Internal QE & Reflectance measured by Sandia for 628B-S2A	4-15

LIST OF ILLUSTRATIONS

<u>Figures</u>	<u>Page</u>
35 I-V curve at 16 suns for AlGaAs on Ge concentrator cell 822C-S1C . . .	4-17
36 External QE for two AlGaAs cells grown on the same substrate	4-19
37 I-V characteristics of GaAs cell before and after Ge substrate removal	4-21
38 Log I-V of the cell in Figure 37	4-22
39 Measured transmission spectrum through a thin GaAs cell	4-23
40 Transmission spectrum calculated for the cell of Figure 39	4-24
41 Transmission spectrum calculated for a thin AlGaAs cell with AR	4-26
42 Photographs of the completed thin AlGaAs concentrator cell (a) front, b) back	4-28
43 One-sun I-V curves before and after removal of the Ge substrate	4-29
44 Log I-V characteristics of cell 822C-S1A from Figure 43	4-30

LIST OF TABLES

<u>Tables</u>	<u>Page</u>
1 Layer structure for GaAs cells grown on GaAs substrates by MOCVD	2-4
2 Parameters input to the grid design model	3-1
3 Results of concentrator grid design	3-3
4 Concentrator cell front side processing	3-4
5 Comparison of J_{sc} for GaAs cells grown on GaAs & Ge.	4-8
6 Comparison of Spire and Sandia measurements at 1 sun for 628B-S2A . . .	4-9
7 Comparison of AlGaAs concentrator cells 628B-S2A and 628A-SIB. . . .	4-16
8 Comparison of AlGaAs solar cell J_{sc} for Ge and GaAs substrates	4-18
9 One sun test results for 1.65 eV AlGaAs concentrator cell 822C-SIA . . .	4-27

SECTION I

INTRODUCTION

1.1 BACKGROUND AND MOTIVATION

The practical efficiency limits for silicon and gallium arsenide solar cells are rapidly being approached.⁽¹⁾ To further improve efficiency, combinations of solar cells responsive to different regions of the solar spectrum have been proposed. Conceptually the simplest of these approaches is the monolithic tandem cell, in which two or more solar cell materials of different bandgaps are grown one on top of the other. The top cell absorbs and collects short wavelength photons, passing the remainder of the spectrum to the cell(s) below it. In the simplest embodiment the cells are connected in series, both optically and electrically. Despite several years of intensive research, the high-efficiency monolithic tandem cell has remained an elusive goal. Principal problems concern the epitaxial growth of mismatched semiconductors and low-resistance connections between cells in the stack.

To avoid these problems another approach has been developed in which the top and bottom cells are individually optimized and then mechanically stacked. An optimum bandgap combination of 1.1 and 1.7 eV can be achieved with highly developed silicon solar cells on the bottom and AlGaAs cells on the top. A major advantage of the mechanically stacked approach is that other solar cell materials with the proper bandgaps could replace the Si or AlGaAs, should increased efficiencies warrant a change. Another advantage of this approach is the availability of two electrical connections for each subcell, simplifying electrical testing and providing some efficiency advantage under changing air mass conditions over the two-terminal monolithic tandem cell. The advantages are traded off against increased mechanical complexity and possible optical losses from reflection and grid shadow between the cells.

While high-efficiency AlGaAs cells have been grown on lattice-matched GaAs substrates,⁽²⁾ the substrates block light that should be passed to the bottom cell. It is therefore necessary to completely remove the substrate, leaving an AlGaAs cell of approximately 5 micron thickness. Some success has been reported using glass superstrates and buried AlGaAs etch-stop layers, but problems remain with the yield of this process.⁽³⁾

To overcome the problems with substrate removal our approach has been to use germanium instead of GaAs substrates. Ge is closely matched to GaAs and AlGaAs in lattice constant and thermal expansion properties, and has been used as a substrate for high efficiency GaAs solar cells.⁽⁴⁻⁶⁾ While Ge is also an opaque substrate, it can be removed in a completely selective manner by etching in hydrogen peroxide. The problem of etchant penetration through pinholes in an AlGaAs etch stop layer, as has been reported for cells on GaAs substrates, is thus obviated.

1.2 STATEMENT OF WORK

The objective of this work has been the development of technology for fabrication of a thin AlGaAs solar cell with an efficiency of 17% at 400 suns. The cell is required to have a bandgap of 1.7eV and be transparent to sub-bandgap photons. Our approach is based upon MOCVD growth of AlGaAs on Ge substrates.

The research program was divided into the following tasks. Significant achievements were realized under each task, as briefly described below.

Task 1 - Cell Design

This task included investigation of both GaAs and AlGaAs cell designs on germanium substrates. The cell structure was a conventional p-on-n heteroface design. The goal of this task was the specification of layer thicknesses and doping levels, grid pattern design, and antireflection coating design.

Accomplishments: Cell designs were completed for both GaAs and AlGaAs cells. A grid pattern optimized for 500 suns operation was designed and photomasks were generated. A tantalum pentoxide antireflection coating was designed for optimum efficiency in conjunction with the AlGaAs window layer.

Task 2 - GaAs Cell Development

As a first step in the development of the thin AlGaAs cell, GaAs cells were to be grown on Ge and GaAs substrates. The development of concentrator cell grid technology, ohmic contact metallizations, and antireflection coatings was to be demonstrated on GaAs cells. The delivery of GaAs concentrator cells to Sandia constituted the first program milestone.

Accomplishments: GaAs solar cells were fabricated on both Ge and GaAs substrates. GaAs concentrator cells with an efficiency of 19.0% were delivered to Sandia. The formation of an unintentional p-n junction in the Ge substrate during GaAs cell growth was identified as a complication in the use of Ge substrates. While this particular problem was solved by removing the Ge substrate, testing of the cells with the substrate intact resulted in degraded efficiency from low fill factors. The best efficiency achieved for a GaAs cell on a Ge substrate at one sun was 16.4%.

Task 3 - AlGaAs Cell Development

The third task involved the development of MOCVD growth of $\text{Al}_{0.2}\text{Ga}_{0.8}\text{As}$ active layers for AlGaAs solar cells. AlGaAs solar cells were to be grown on Ge and GaAs substrates. The delivery of AlGaAs concentrator cells to Sandia was the second program milestone.

Accomplishments: AlGaAs solar cells were fabricated on both Ge and GaAs substrates. 1.69 eV AlGaAs concentrator cells were delivered to Sandia with an efficiency of 13.7% at 242 suns.

Task 4 - Substrate Removal Studies

Development of substrate removal procedures constituted the final task. Procedures for bonding the cell to a glass superstrate, removing the substrate, and applying ohmic contacts were to be developed. The delivery of thin AlGaAs cells bonded to a cover glass was the final milestone of the program.

Accomplishments: Processing procedures for superstrate attachment, substrate removal, back ohmic contact grid formation, and back antireflection coating were demonstrated. A thin (5 micron) GaAs cell was produced and delivered to Sandia. Its efficiency actually improved when the substrate was removed, from 14.2% to 15.2% at one sun. This cell had parallel finger grid patterns on both sides and was transparent to below-bandgap light. A thin AlGaAs cell was also produced and delivered to Sandia. This cell demonstrated the complete process, with concentrator cell grid patterns and antireflection coatings on both sides of the 5-micron cell. Although the initial efficiency of the cell was low due to poor diffusion lengths in this particular MOCVD run, the cell did maintain its efficiency through the complete process, proving feasibility of the approach.

1.3 ORGANIZATION OF THIS REPORT

The report is divided into three main technical sections: Section 2 - Materials Development, Section 3 - Process Development, and Section 4 - Test Results. Section 2 addresses the materials issues involved in the MOCVD growth of GaAs and AlGaAs solar cells on Ge and GaAs substrates. This section contains information on the MOCVD growth system, the solar cell layer structures, and special problems associated with heteroepitaxial growth on Ge substrates. Section 3 covers the development of processing procedures for the thin AlGaAs concentrator cell. It includes design of the 500 suns concentrator grid pattern, processing of the solar cell prior to bonding to the superstrate, and the substrate removal and back side fabrication processes for the thin cell. Section 4 describes test results for the various types of cells produced during the program. The evolutionary progression starts with GaAs cells grown on GaAs substrates and continues through thin AlGaAs concentrator cells. Section 5 summarizes the results of the program. Section 6 discusses the key issues raised during the program and areas for future work.

SECTION 2

MATERIALS DEVELOPMENT

2.1 MOCVD SYSTEM

Spire has developed an MOCVD reactor specifically for GaAs and AlGaAs crystal growth. This reactor (the SPI-MO CVDTM 450), shown in Figure 1, was used for all crystal growth in the program. A schematic of the reactor is shown in Figure 2.

Operating Parameters

Some typical operating parameters of the SPI-MO CVDTM 450 are as follows:

1. Composition: Full range of GaAs to AlAs and GaP to GaAs.
2. Doping: n-type (SiH₄) 10^{15} to 10^{19} cm⁻³
p-type (DMZn) 10^{15} to 5×10^{19} cm⁻³
3. Growth Rate: 0.006 to 0.5 micron/min.
4. Uniformity: Thickness: Better than $\pm 5\%$
Doping: Better than $\pm 10\%$
5. Growth Area: 100 cm²
6. Background (undoped) GaAs: n-type, 1×10^{14} cm⁻³
7. Typical System Output: 2 to 4 runs per shift

Specifications

1. Reaction Chamber: Vertical geometry, water-cooled fused silica vessel with automatic drain and pump-purge features.
2. Susceptor: SiC-coated ultrapure graphite; variable speed rotation.
3. Wafer Loading Area: HEPA-filtered air flow chamber
4. Baseplate: Pneumatically positioned, water-cooled, stainless steel with provisions for susceptor rotation and positive double O-ring vacuum seal.
5. Temperature Control: RF heated with rotating thermocouple and feedback controller for $\pm 1^\circ\text{C}$ accuracy.

6. Gas Delivery System: 316 stainless steel fittings and seamless tubing, all cleaned and passivated; all welded and face-seal connections; pneumatic bellows valves; stainless steel line filters; "zero-dead-space" manifold with 4-port bellows valves.
7. Gas Control: Computer-driven electronic mass flow controllers and tied-diaphragm line regulators.
8. Arsine Dryer: GaInAl-type dessicator system for removal of oxygen and water vapor from the arsine gas line (installed after the end of the program).
9. Liquid-Source Regulation: Large-volume cooling baths for MO sources with 0.01°C regulation; pumpout capability for bubbler changing; upstream liquid traps; connection pieces supplied to accommodate various cylinder configurations.
10. System Control: Programmable process controller linked to IBM personal computer with dual floppy-disk storage and printer; full manual override.
11. Gas Analysis: Residual Gas Analyzer system for real-time analysis of trace contaminants in the reaction chamber (installed after the end of the program).
12. Safety Interlocks: Cooling water for baseplate and belljar; vacuum seal and position of baseplate; process chamber door lock; exhaust line backpressure; low air pressure; toxic-gas-monitor input; system fault alarm.

2.2 MATERIAL CHARACTERIZATION

To characterize the doping profiles of the as-grown material, a Polaron profile plotter was routinely used for all growth runs. Problems were encountered in reliably measuring the heavily-doped cap layer and the high-aluminum-content window layer, so these layers were first removed by selective etching. SIMS (Secondary Ion Mass Spectroscopy) was also used extensively to check the dopant profiles, including the window and cap layers. In addition, SIMS was used to characterize AlGaAs

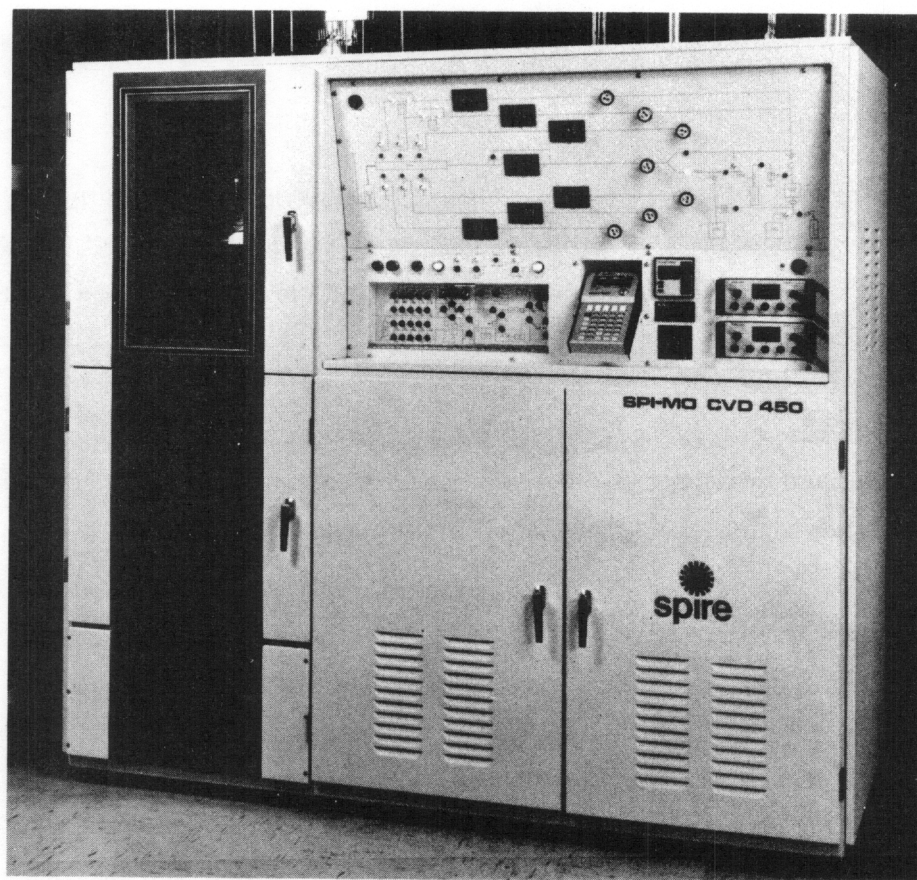


FIGURE 1. PHOTOGRAPH OF THE SPI-MO CVDTM 450 REACTOR.

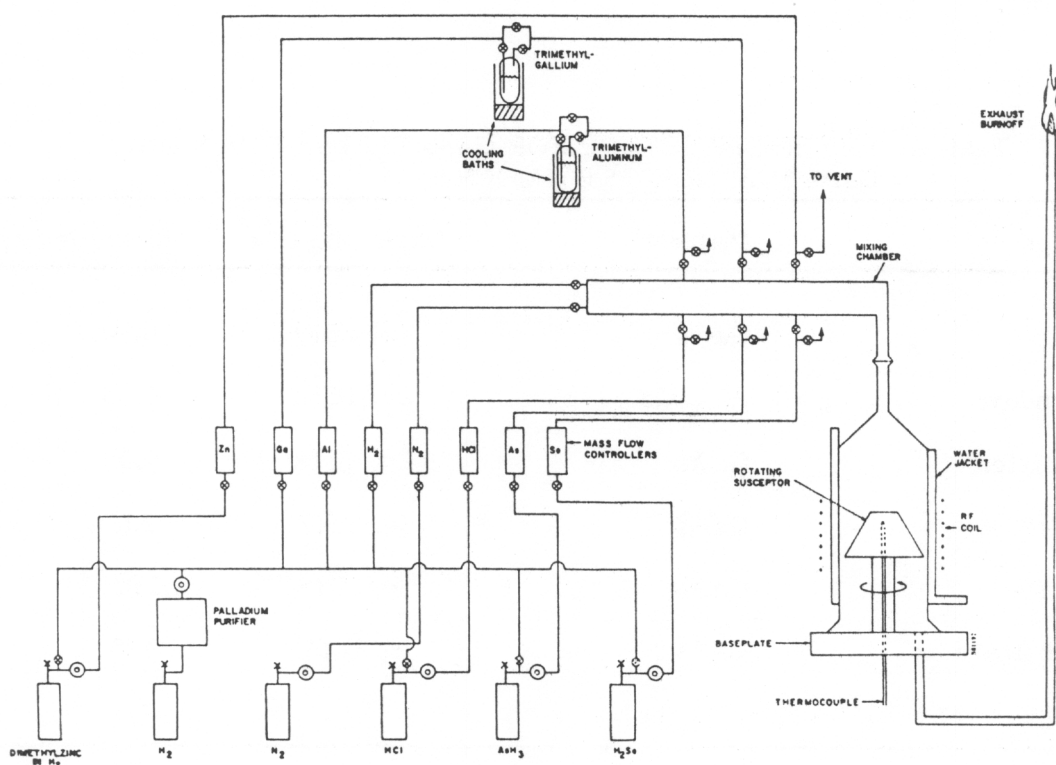


FIGURE 2. SCHEMATIC OF THE SPI-MO CVDTM 450 REACTOR SYSTEM.

contamination by O and C, and to investigate Ge autodoping of the layers when Ge substrates were used. Typical SIMS profiles of Zn and Si dopants for an AlGaAs cell are shown in Figure 3, and O and C impurity profiles are shown in Figure 4. Agreement between SIMS and Polaron measurements was usually within a factor of 2 in the base and emitter layers of the cells, although wider variations were encountered. Figure 5 compares SIMS and Polaron measurements for all cell runs in which both were measured. Generally the agreement was better for n-type layers, as expected from the difficulty in profiling heavily doped p-type layers with the Polaron profiler.

2.3 GaAs CELLS ON GaAs SUBSTRATES

Of the solar cell/substrate combinations investigated in this work, the most developed growth technology and the simplest from a materials standpoint is the baseline GaAs solar cell on a GaAs substrate. A typical layer structure for this cell is given in Table 1 and shown in Figure 6(a). Growth temperatures were typically 700°C for the GaAs layers and 750°C for the AlGaAs window layer. Typical growth rates were 4.0 micron/hour for the buffer, base and emitter layers, and 2.0 micron/hour for the window and cap layers. Flow ratios of the Group V to Group III elements were 10:1 at 700°C and 15:1 at 750°C.

Table 1. LAYER STRUCTURE FOR GaAs CELLS GROWN ON
GaAs SUBSTRATES BY MOCVD

Layer	Material	Doping (cm ⁻³)	Thickness (μm)
Cap	GaAs	Zn, 8E19	0.30
Window	Al _{0.87} Ga _{0.13} As	Zn, 1E18	0.15
Emitter	GaAs	Zn, 2E18	0.50
Base	GaAs	Se, 2E17	2.0
Buffer	GaAs	Se, 2E18	2.0
Substrate	GaAs	Si, 2E18	400

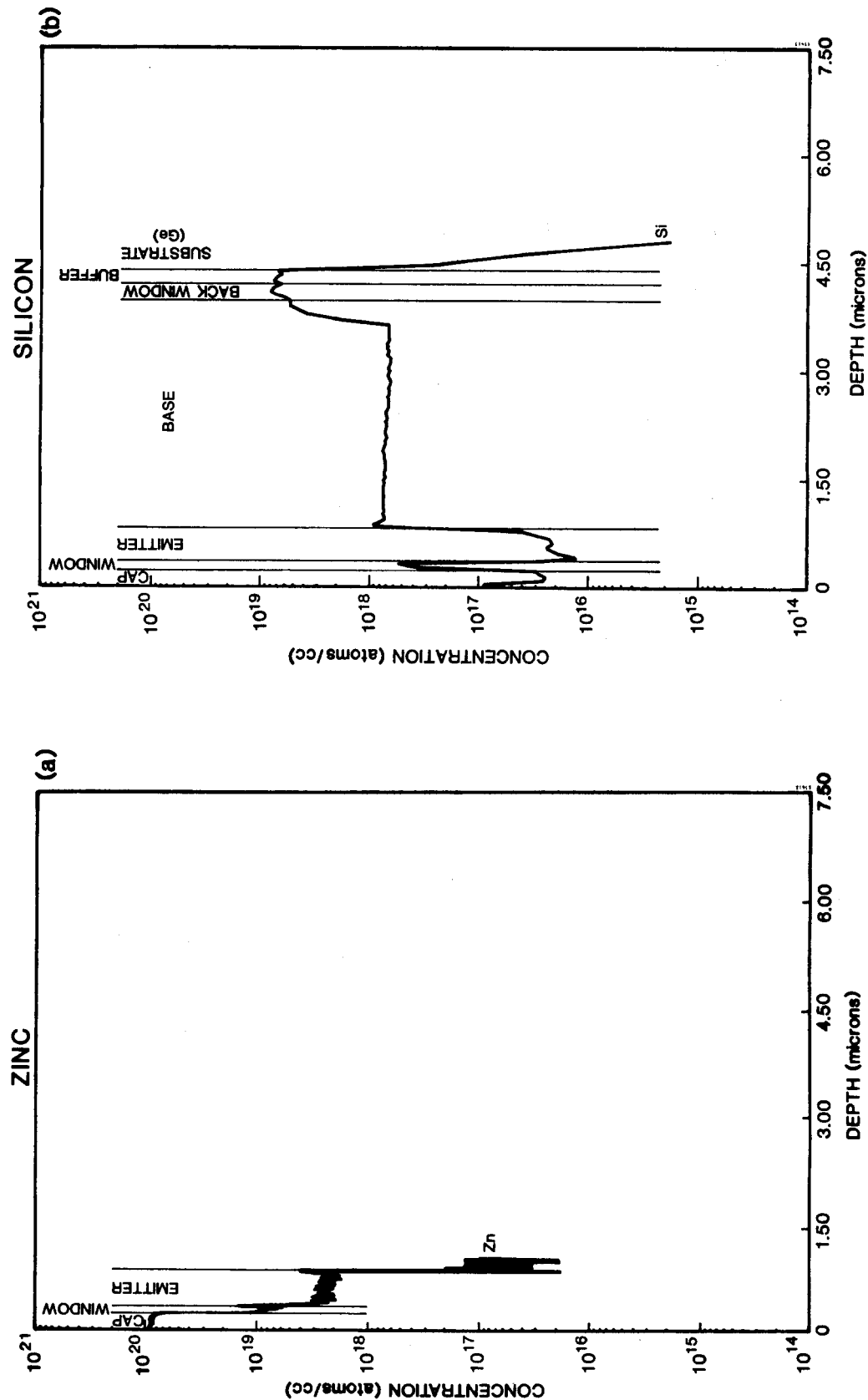


FIGURE 3. SIMS PROFILES OF (a) Zn AND (b) Si DOPANTS IN AN AlGaAs SOLAR CELL.

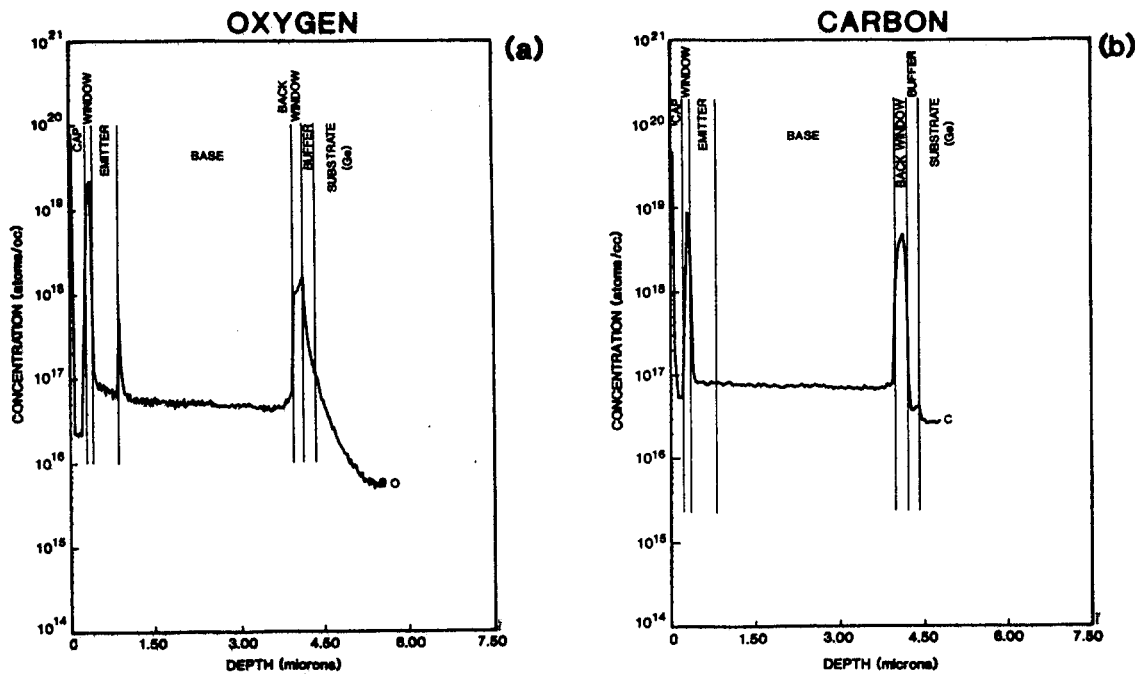


FIGURE 4. SIMS PROFILES OF (a) O AND (b) C IMPURITIES IN THE AlGaAs SOLAR CELL OF FIGURE 3.

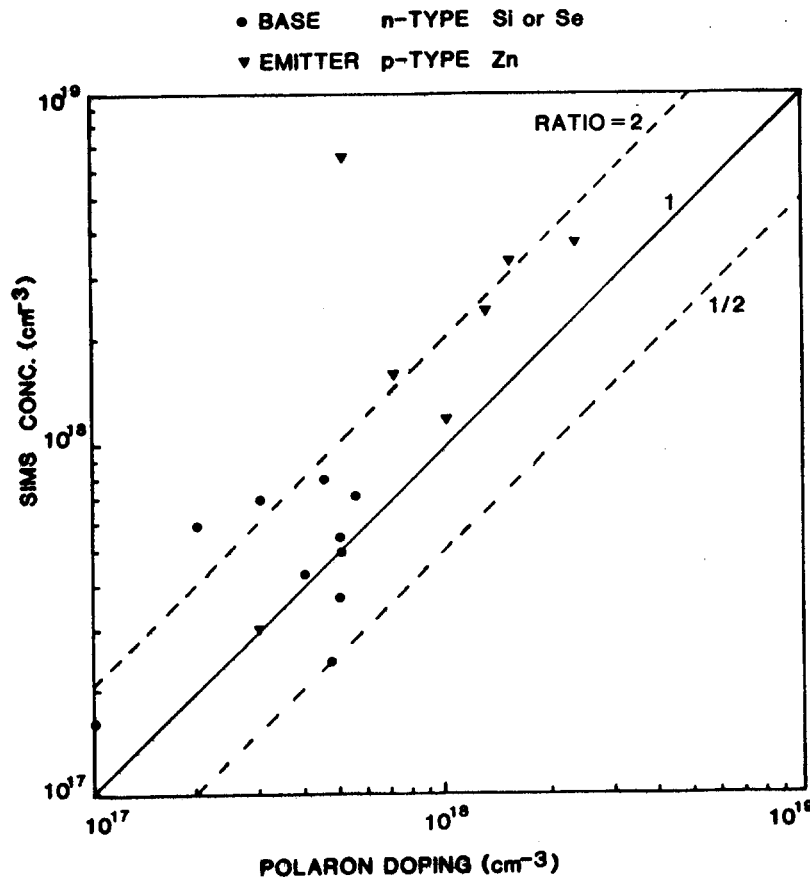
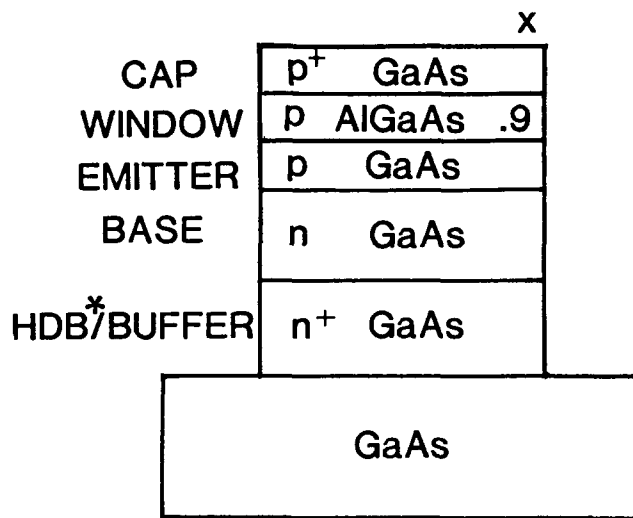
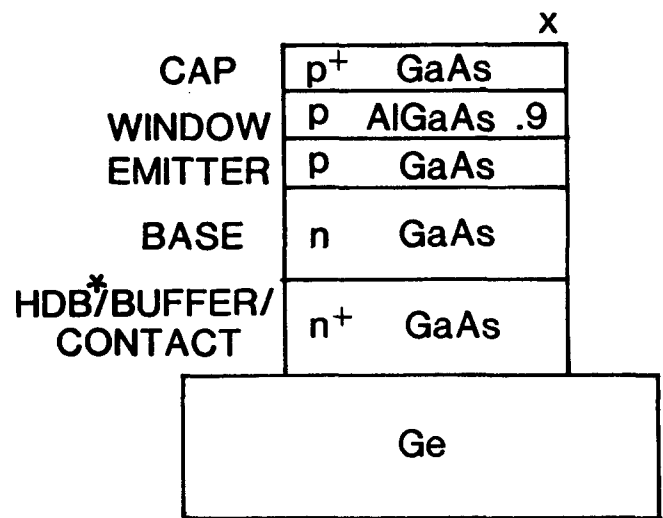


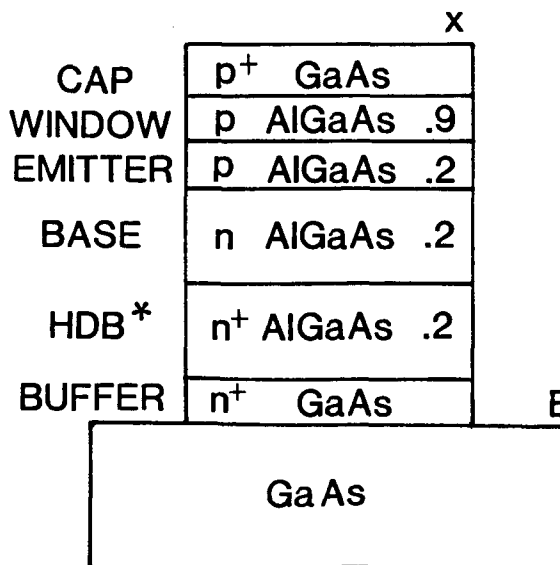
FIGURE 5. COMPARISON OF SIMS AND POLARON MEASUREMENTS OF DOPANT CONCENTRATIONS IN THE EMITTER AND BASE LAYERS FOR A NUMBER OF AlGaAs AND GaAs SOLAR CELL RUNS.



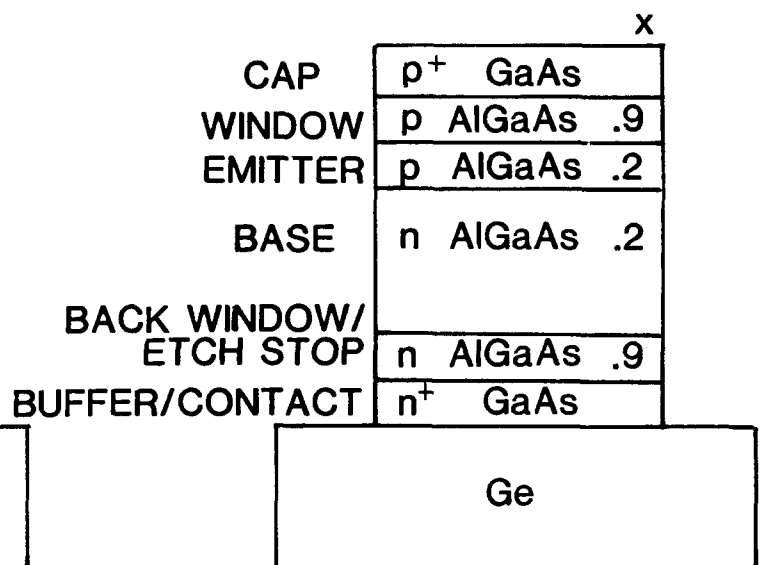
(a) GaAs on GaAs



(b) GaAs on Ge



(c) AlGaAs on GaAs



(d) AlGaAs on Ge

*HDB = HEAVILY DOPED BASE

FIGURE 6. LAYER STRUCTURES FOR THE FOUR SOLAR CELL/SUBSTRATE COMBINATIONS INVESTIGATED.

2.4 AlGaAs CELLS ON GaAs SUBSTRATES

The structure of an AlGaAs solar cell is very similar to that of a GaAs cell, as seen in Figure 6. The active cell layers (emitter, base and highly doped base) are composed of AlGaAs with a 1.7eV bandgap, instead of GaAs. The major difference in terms of growth is in the growth temperature. It has been found by many workers that the quality of MOCVD AlGaAs improves as the growth temperature is increased.⁽⁷⁾ Growth temperatures in the vicinity of 800°C produce the best AlGaAs, while 650 to 700°C is sufficient for GaAs. The higher growth temperatures lessen the effects of oxygen impurities in AlGaAs, although the mechanism is not understood at the present time. Oxygen produces particularly potent deep recombination levels in AlGaAs, degrading the minority carrier lifetime and diffusion length in the material. Concentrations of oxygen as low as 10 ppm in the gas stream have been shown to drastically reduce material quality. The sources of oxygen in the MOCVD process are usually attributed to impure source gases, particularly arsine, or to leaks in the reactor itself.

We have characterized the amount of oxygen in AlGaAs cells by SIMS measurements. To obtain quantitative information, oxygen standards were created by ion implantation into samples of GaAs, $\text{Al}_{.2}\text{Ga}_{.8}\text{As}$, and $\text{Al}_{.87}\text{Ga}_{.13}\text{As}$. The analysis was carried out by Charles Evans and Associates. A typical oxygen depth profile through an AlGaAs cell is shown in Figure 7. The amount of oxygen exponentially increases with the amount of aluminum in the AlGaAs layers; window layers have very high concentrations of oxygen. Figure 8 summarizes the amount of oxygen as a function of the aluminum fraction for a number of cells. We have also tried to correlate the measured oxygen concentrations in the active cell layers with cell performance, particularly short circuit current. Figure 9 shows a plot of J_{sc} versus oxygen content for a number of cells from each MOCVD run. The error bars show the full range of measured values. All J_{sc} values have been normalized to a 5% grid shadow, to account for different grid patterns. For this figure all oxygen profiles were measured on the same day to minimize systematic errors. Oxygen concentrations measured on previous occasions are indicated by horizontal arrows in the figure. A trend toward higher J_{sc} with lower oxygen concentration may be inferred, particularly if the older O data are used. However, it is clear that the large variation in J_{sc} within wafers from the same run and the uncertainty in SIMS oxygen concentrations make it difficult to correlate J_{sc} with oxygen on a run-by-run basis. More spatially localized measurements of J_{sc} and oxygen concentration are necessary to establish a correlation, and the accuracy of the SIMS measurement must be improved.

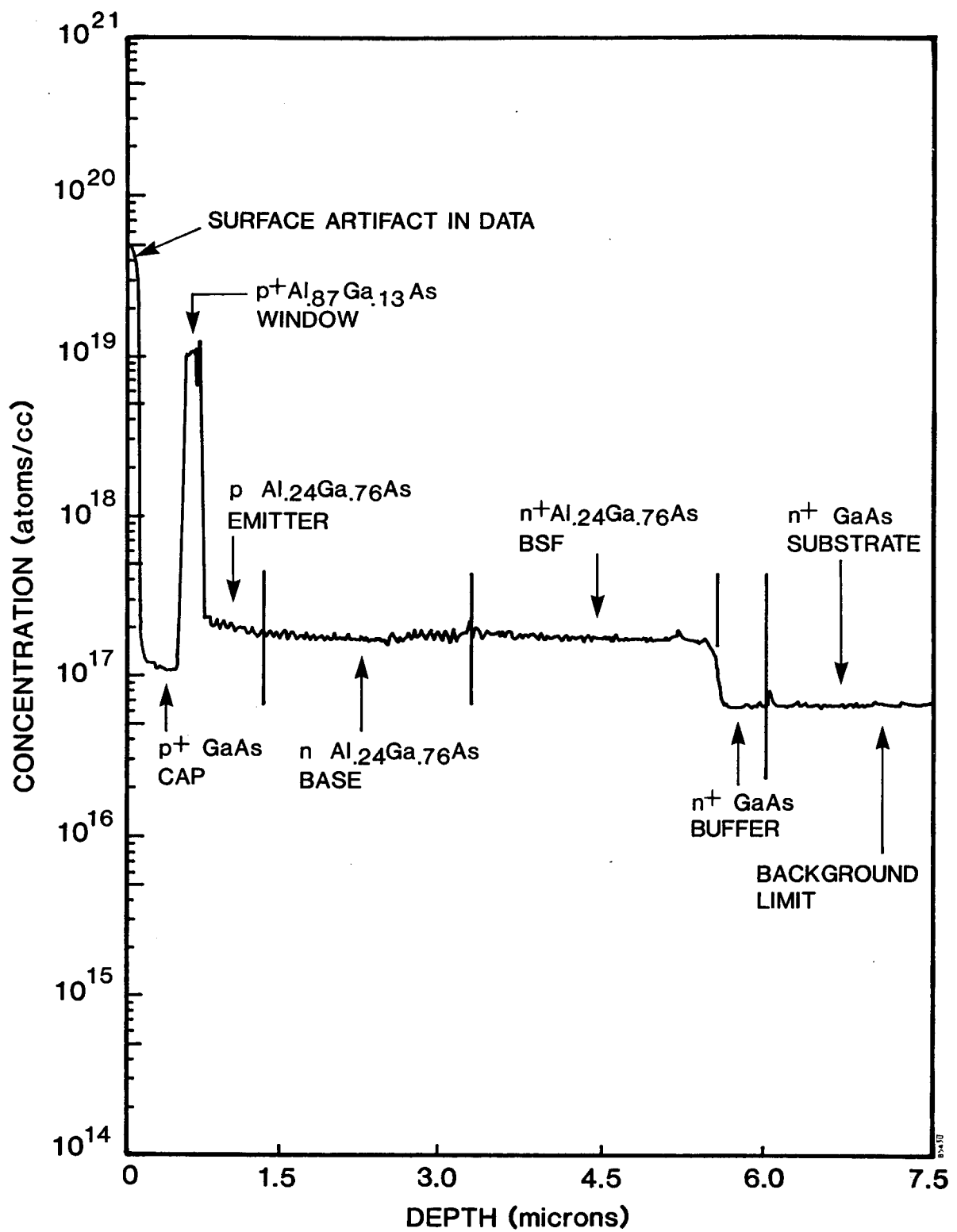


FIGURE 7. SIMS DEPTH PROFILE OF OXYGEN IN AN AlGaAs SOLAR CELL, RUN 627.

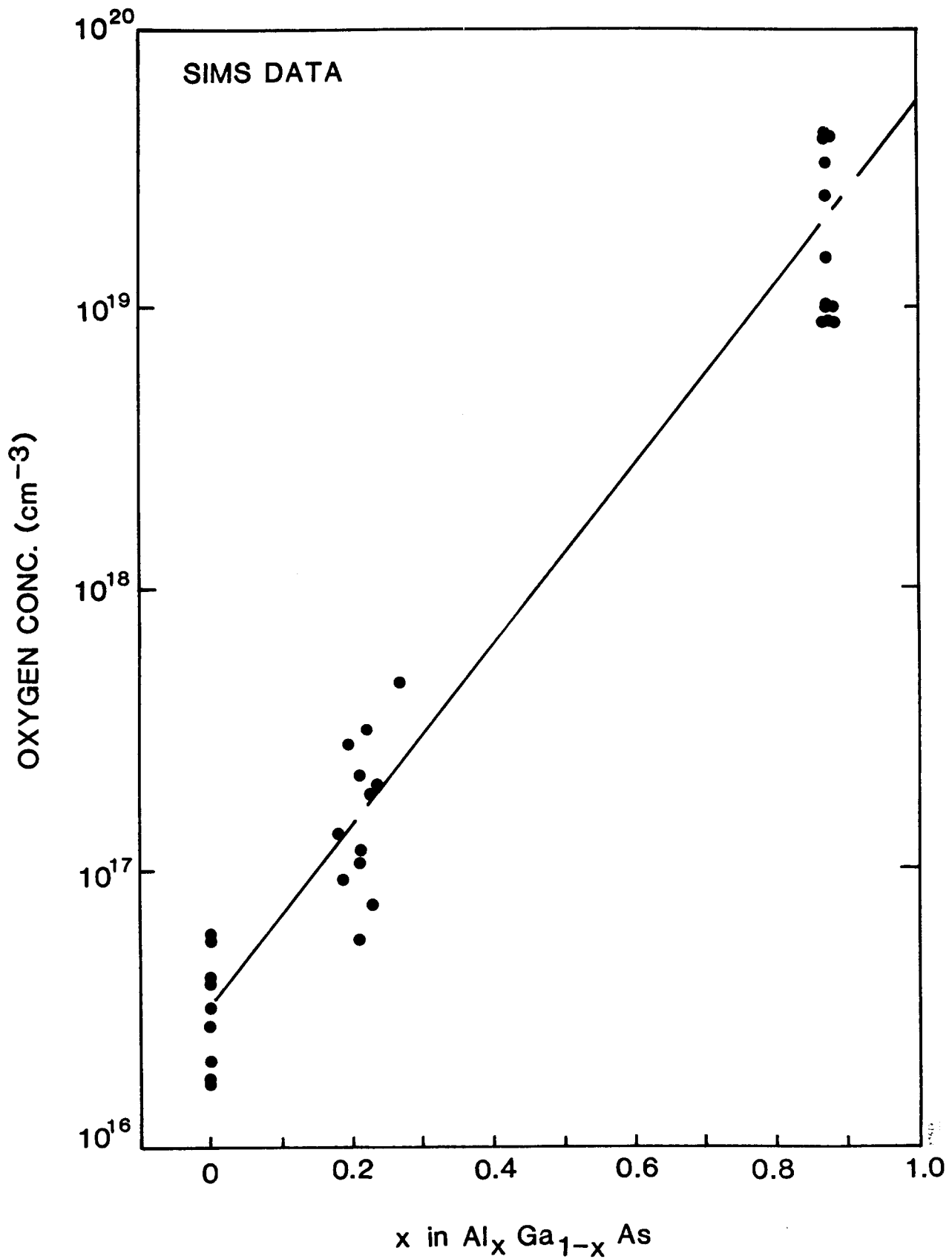


FIGURE 8. OXYGEN CONCENTRATION AS A FUNCTION OF ALUMINUM CONTENT IN AlGaAs LAYERS, SUMMARIZING SEVERAL SOLAR CELL RUNS.

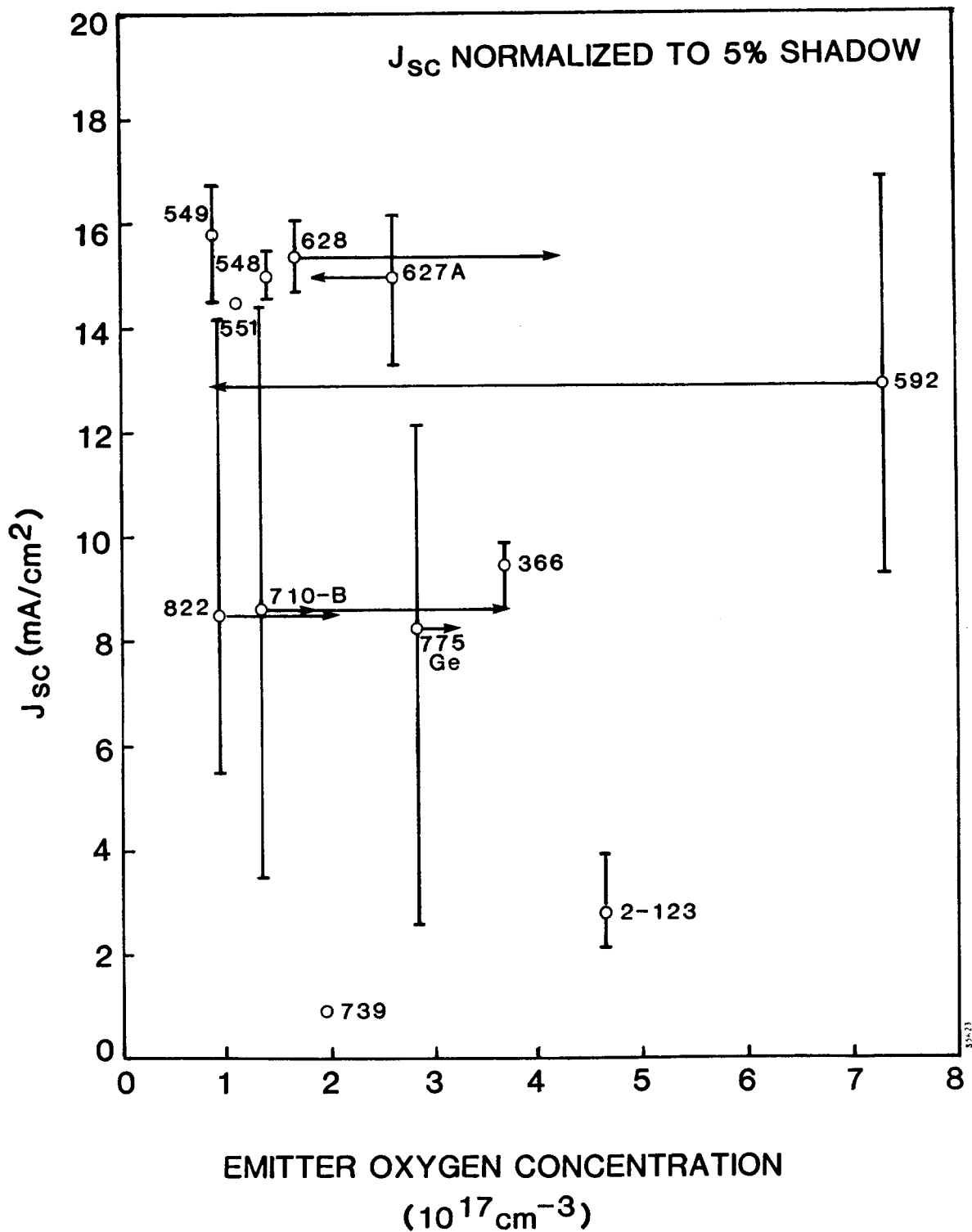


FIGURE 9. AlGaAs SOLAR CELL SHORT CIRCUIT CURRENT DENSITY AS A FUNCTION OF OXYGEN IMPURITY CONCENTRATION. The oxygen was measured by SIMS in the emitter of the solar cells. Each data point represents a different AlGaAs MOCVD run.

One problem we have had in this study is poor reproducibility of the absolute amount of oxygen measured by SIMS. Samples measured at different times can have variations up to a factor of six in oxygen concentration, as seen from Figure 9. Profile shapes are reproducible, but the calibration of absolute concentration is not. One problem is in the measurement itself. SIMS detects ions sputtered off the surface of the sample. Gases adsorbed on the surface of the sample can also contribute to the signal. If the gases are adsorbed faster than they can be sputtered away, then a high background is measured. This background depends on the quality of the vacuum at the time of the measurement, and also on the composition of the sample. Layers with high aluminum concentrations are more reactive with oxygen, and so appear to have a higher oxygen concentration. To evaluate the importance of this mechanism, measurements are made at both high and low sputtering rates. At the higher rates the relative amount of oxygen should be decreased, if surface adsorption is a factor. When this was done the oxygen profile was unchanged, suggesting that the measurement is valid. A second source of error was in the oxygen standard samples. Even at high energies oxygen can only be implanted to a small depth in AlGaAs. The surface of AlGaAs is reactive, becoming more so as the Al fraction increases. We attempted to protect the $\text{Al}_{.87}\text{Ga}_{.13}\text{As}$ sample against oxidation with a 200 Å cap layer of GaAs. This was successful, as no oxidation of the sample was noted. The $\text{Al}_{.2}\text{Ga}_{.8}\text{As}$ sample, however, was not protected. In the course of a year over which these measurements were done, progressive oxidation consumed a portion of the ion implanted layer, degrading the accuracy of the calibration. Unfortunately the SIMS analyst chose this AlGaAs sample as the calibration standard for Figure 9, so the absolute concentrations are in question.

A fairly wide variation in AlGaAs cell quality was observed over the course of the program. Figure 10 plots the solar cell J_{sc} as a function of run number. Run numbers were sequential, so it also plots J_{sc} as a function of time. We were able to correlate some of the run-to-run variations with changes in the source gases. For example, a new bottle of arsine was installed just before run 739. Obviously it was not a good bottle. Other changes in AlGaAs quality could not be readily correlated with the source gases, and may be related to intermittent leaks in the reactor. We have noted that for the better runs the spread in J_{sc} is less than for the poor runs. Runs with low J_{sc} usually show a strong gradient across the wafer, usually from top to bottom on the susceptor. This suggests that oxygen is entering the reactor at the top of the bell jar, either from the

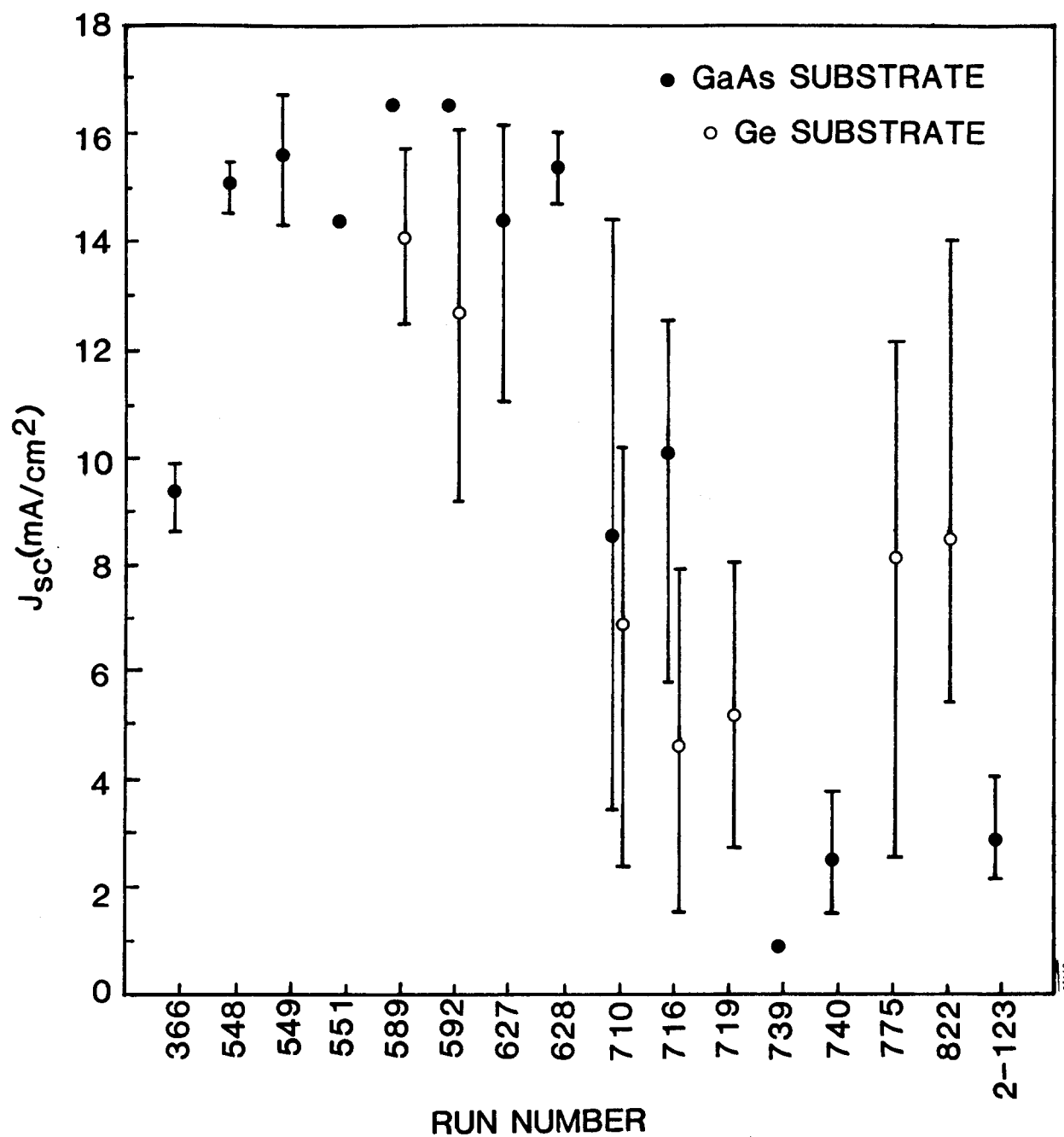


FIGURE 10. AlGaAs SOLAR CELL J_{sc} AS A FUNCTION OF RUN NUMBER. The error bars show the full range of measured values. J_{sc} values have all been corrected to the same grid shadow loss of 5%.

source gases or from a leak, and is being gettered as it passes over the AlGaAs layers. One wafer which showed a strong gradient in J_{sc} was examined by SIMS in both good and bad regions. The oxygen profiles are compared in Figure 11. The region of low J_{sc} had about twice as much oxygen as the good region, supporting our hypothesis. In addition, the oxygen profile showed an oscillatory fine structure for the sample at the top of the wafer. The period of the oscillations corresponds to the rotation of the susceptor in the bell jar, again suggesting a small leak.

Subsequent to the completion of this program, a new MOCVD reactor dedicated to solar cell development became operational. It features increased leak integrity and provision for removing oxygen from the arsine source gas. Excellent AlGaAs cell results have been obtained with this machine, suggesting that the sources of problems have been identified and eliminated.

2.5 GaAs AND AlGaAs CELLS ON Ge SUBSTRATES

The growth conditions and GaAs solar cell structure were essentially the same for GaAs and Ge substrates. This conveniently allowed direct comparisons of cells on Ge and GaAs substrates from the same growth run. Some modifications to the initial growth conditions were made, based on information from Ge autodoping studies (see Section 2.5.2). Namely, in some cases the first half micron of GaAs was grown at 700°C, with the remainder grown at 650°C. (However, no difference in cell performance was noted, whether two-temperature or single temperature growth was used). No additional etch stop or contact layers were required for cells in which the Ge substrate was to be removed, because the selective etchant stopped at the heavily doped GaAs layer at the rear of the cell.

In contrast, the growth of AlGaAs on Ge required some changes relative to growth on GaAs (see Figure 6). The GaAs buffer/contact layer at the rear of the AlGaAs cell would block light in the 700-870 nm band intended for the bottom cell of a tandem structure. A layer structure analogous to the front of the cell was therefore adopted, with an AlGaAs window/etch stop layer at the back of the cell. The GaAs contact layer could then be etched away between the grid lines on the back of the cell. In addition, the window provides a heterojunction barrier for confinement of minority carriers in the base of the cell. The growth conditions were again very similar for GaAs or Ge substrates, allowing a direct comparison of AlGaAs cells from the same growth run.

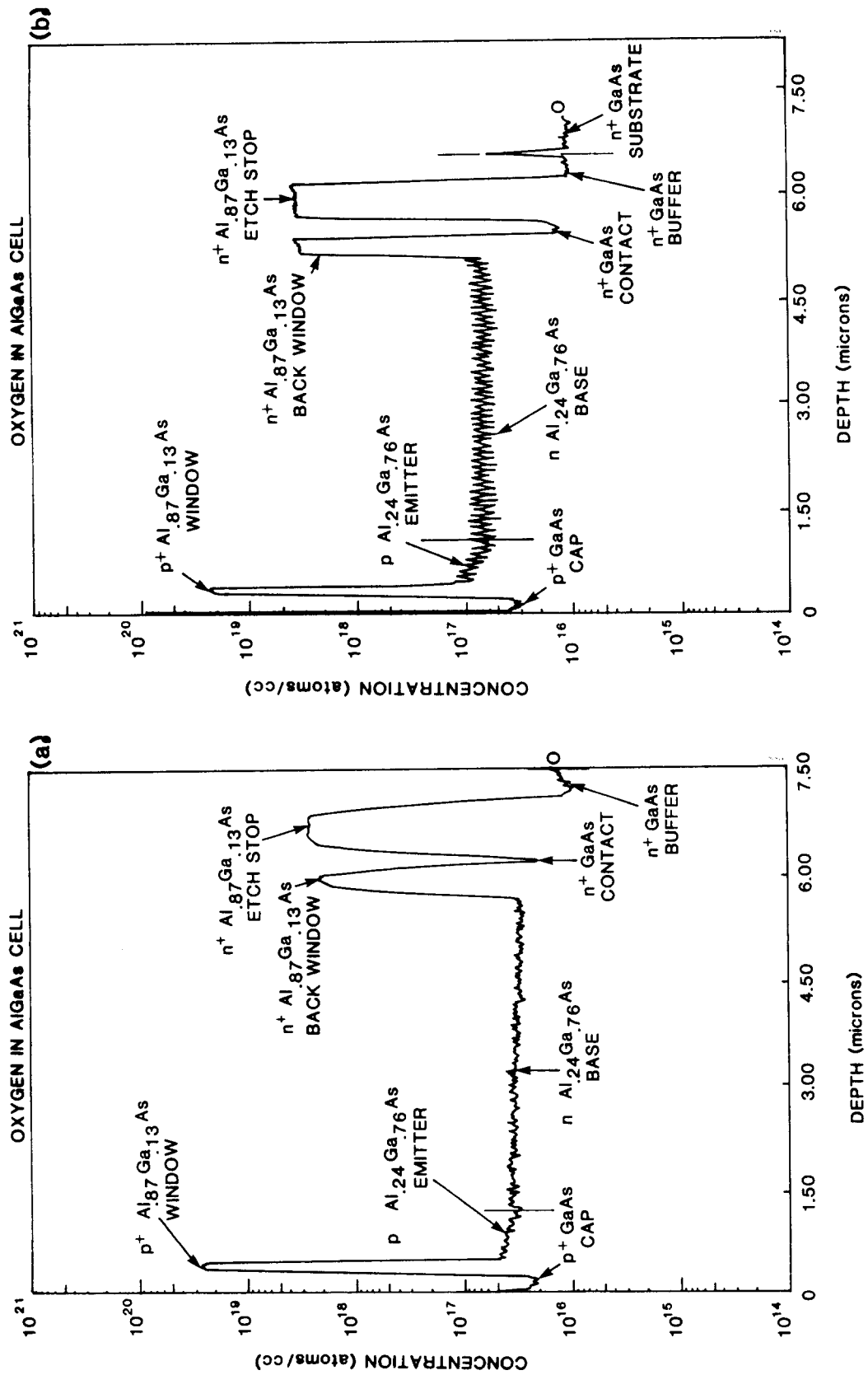


FIGURE 11. COMPARISON OF SIMS OXYGEN PROFILES FOR (a) GOOD AND (b) BAD REGIONS OF AN AlGaAs SOLAR CELL WAFER.

Although closely matched in lattice constant and thermal expansion coefficient to GaAs, the use of Ge substrates introduces a number of potential problems in the growth process. The first is cross-doping. Ge is a dopant in GaAs and AlGaAs, while Ga, As, and Al are dopants in Ge. At the elevated temperatures used for GaAs and particularly AlGaAs growth, doping can occur by solid phase diffusion or gas phase transport. These effects were investigated in the 1960's and 1970's,⁽⁸⁾ before the MOCVD technique was in use, and were found to be important. In particular, vapor phase transport by HCl was the major cause of Ge autodoping in GaAs.⁽⁹⁾ Unlike most of the earlier growth techniques, MOCVD does not involve the use of HCl. For this reason, as well as the different growth temperatures and deposition chemistry, an investigation of Ge autodoping in the MOCVD growth of GaAs and AlGaAs was undertaken. A less commonly recognized problem is doping of the Ge substrate by indiffusion from the epitaxial layers; this also was investigated. Another potential problem related to heteroepitaxy is the generation of misfit dislocations from the small (0.08%) lattice mismatch between GaAs and Ge. In earlier work the density of threading dislocations in GaAs grown on Ge was found to be about 10^6 per cm^2 .⁽¹⁰⁾ Finally, a practical problem common to all forms of epitaxy is substrate preparation prior to growth. Procedures were needed for producing clean, crystallographically perfect Ge surfaces. These special considerations related to growth on Ge are discussed in the following sections.

2.5.1 Ge Substrate Preparation

To achieve high quality heteroepitaxial layers on Ge substrates, a clean, crystallographically perfect Ge surface is required. We found substrate preparation to be a critical and surprisingly difficult aspect of growth on Ge. A large part of the problem was obtaining Ge substrate wafers of the desired orientation and doping with clean, polished, damage-free surfaces. We usually found it necessary to clean up the surfaces of wafers as received from vendors. Since the nature of the surface contaminants was unknown and Ge processing is somewhat of a lost art, a considerable amount of effort was spent in learning to clean Ge surfaces.

In some of the early work on GaAs-on-Ge heterostructures reported in the literature an in-situ high temperature HCl etch was used to prepare atomically clean Ge surfaces prior to growth. This approach was not pursued here because of concern about Ge autodoping. Instead, the Ge surface was cleaned by chemical means just before

insertion into the MOCVD reactor. The full process is as follows. The germanium substrates were polished 2-inch wafers oriented 2-3° off (100) toward (110), doped with As to 1×10^{17} - 1×10^{18} . The wafers were cleaned in hot trichlorethylene to remove wax residues from polishing, followed by acetone, methanol, and DI water. If residual contamination was detected by oblique illumination with a bright light, then the wafers were mechanically scrubbed with a detergent solution and thoroughly rinsed in DI water. Immediately prior to loading in the growth chamber, the substrates were etched for 30 seconds in a 30:2:1 solution of H_2O , H_2O_2 , and NH_4OH . The wafers were heated to the growth temperature in flowing hydrogen with no additional high-temperature bakes.

Due to problems with Ge autodoping, it was found necessary to also treat the back sides of the Ge wafers (see next section). In this case a layer of epitaxial GaAs was first grown on the Ge wafer back side to seal it. To obtain pinhole-free GaAs layers we used Ge wafers polished on both sides. The pre-growth cleaning procedure was the same as for growth on the front of the wafer. After a 10 micron undoped GaAs layer was grown on the back of the Ge, the wafer was again etched in the 30:2:1 solution to remove any contamination or surface damage from the front side. The Ge wafer was then ready for cell growth.

2.5.2 Ge Autodoping

By autodoping we mean the transfer of Ge atoms from the substrate to the GaAs or AlGaAs epitaxial layers. It is a concern because Ge is an n-type dopant and could affect the doping profile of the solar cell. Autodoping is primarily a gas-phase transport process in which Ge atoms evaporate (or are chemically etched) from the substrate, are transported in the gas stream, and then incorporate into the growing layer. Solid-phase diffusion of Ge into the epitaxial layers also occurs, but is of lesser importance. Significant solid diffusion occurs only at high growth temperatures and only immediately adjacent to the interface. Gas-phase autodoping, on the other hand, can occur throughout the epitaxial structure as long as a source of Ge is exposed to the gas stream.

Ge autodoping was first studied as a function of growth temperature. Undoped 3-micron GaAs layers were grown on Ge substrates in the temperature range of 620 to 750°C. The doping profile in the epitaxial layer was measured with a Polaron Profile

Plotter. The resulting profiles are shown in Figure 12. In general the n-type doping profile is high near the GaAs/Ge interface, then decreases to a relatively constant level through most of the GaAs layer. Qualitatively this can be understood as reduced autodoping once the front of the Ge wafer is completely covered by GaAs. However, the exposed back of the wafer still provides a constant source of Ge throughout the growth.

Several growth variations were tried during this series of experiments. First, the As/Ga ratio was either 10:1 or 20:1. At the higher ratio there was evidence of slightly increased autodoping. Since n-type doping depends on Ge atoms finding Ga sites in the lattice preferentially over As sites, increasing the supply of As should result in fewer acceptors and hence more n-type doping. Another variation was an 850°C prebake in $\text{AsH}_3 + \text{H}_2$ to remove any surface contamination. Although little improvement in surface morphology was noted as a result of this treatment, it did increase the amount of autodoping. A third variation was a two-temperature deposition, in which the initial half micron was grown at 700°C, then the temperature was lowered to 650°C. Not surprisingly, the surface doping was characteristic of a 650°C growth while the interface concentration was raised. This sequence was selected to minimize the number of interface traps as well as the autodoping near the surface.

The amount of autodoping increases exponentially with growth temperature, as shown in Figure 13. Also shown in the figure is the amount of autodoping near the GaAs/Ge interface and the number of light-sensitive traps near the interface. The latter quantity was determined by comparing doping profiles measured in the dark and under illumination. (This is a unique capability of the Polaron profiler). Two examples are shown in Figure 14. A minimum in the number of traps occurs at about 690°C.

In many cases the Polaron doping profiles were continued into the Ge. One must be cautious about interpreting this data because the profiler was not calibrated for Ge, and the quality of the electrolyte Schottky barrier was poorer for Ge. However, the Ge doping values from the Polaron are in rough agreement with the expected bulk values. The general increase in doping near the interface could be evidence of solid-phase As diffusion into the Ge. The ability to examine cross-doping on both sides of the heterojunction is another unique capability of the Polaron profiler, hard to duplicate in other techniques.

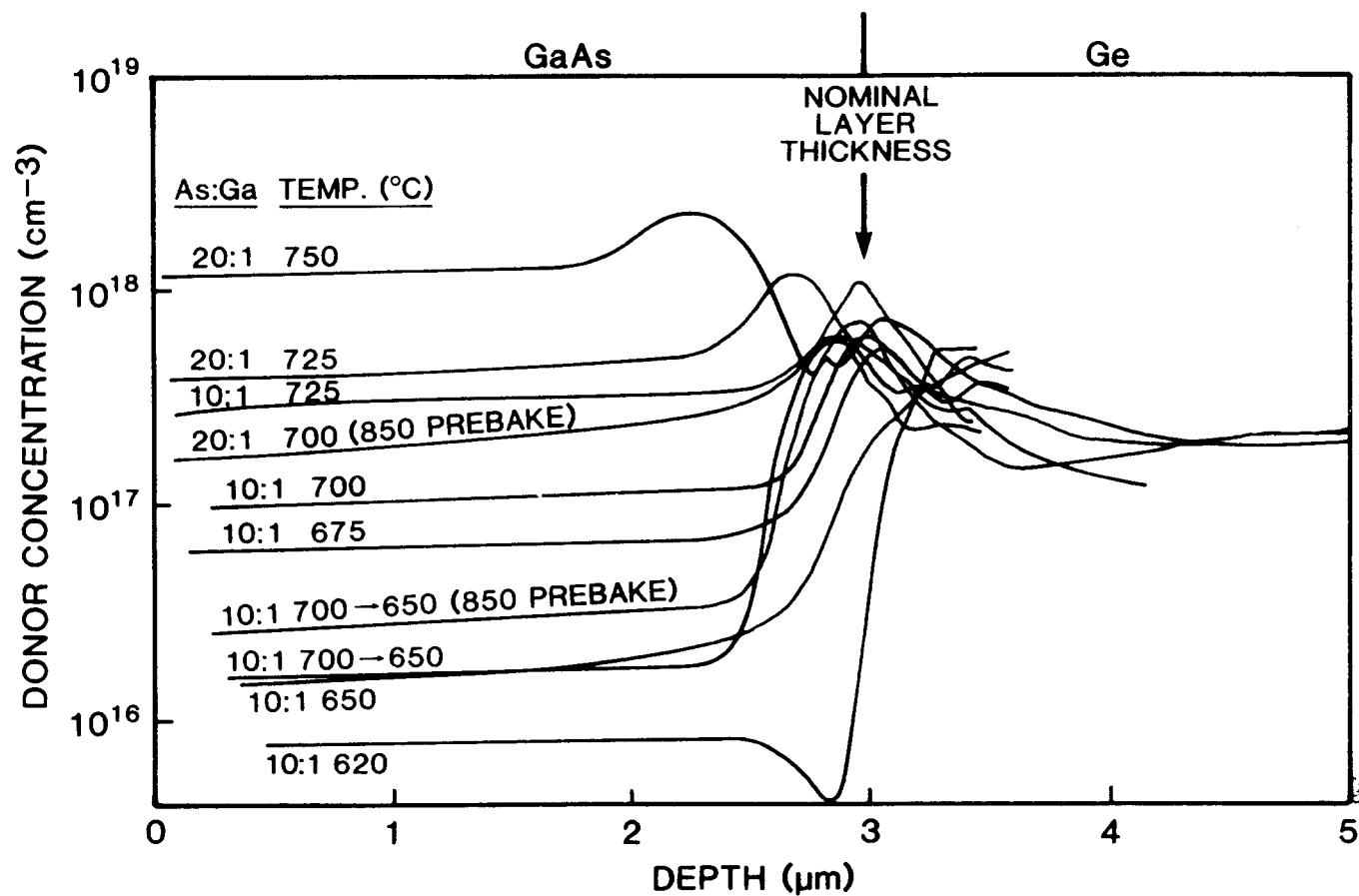


FIGURE 12. POLARON PROFILES OF AUTODOPING IN GaAs LAYERS GROWN ON Ge SUBSTRATES.

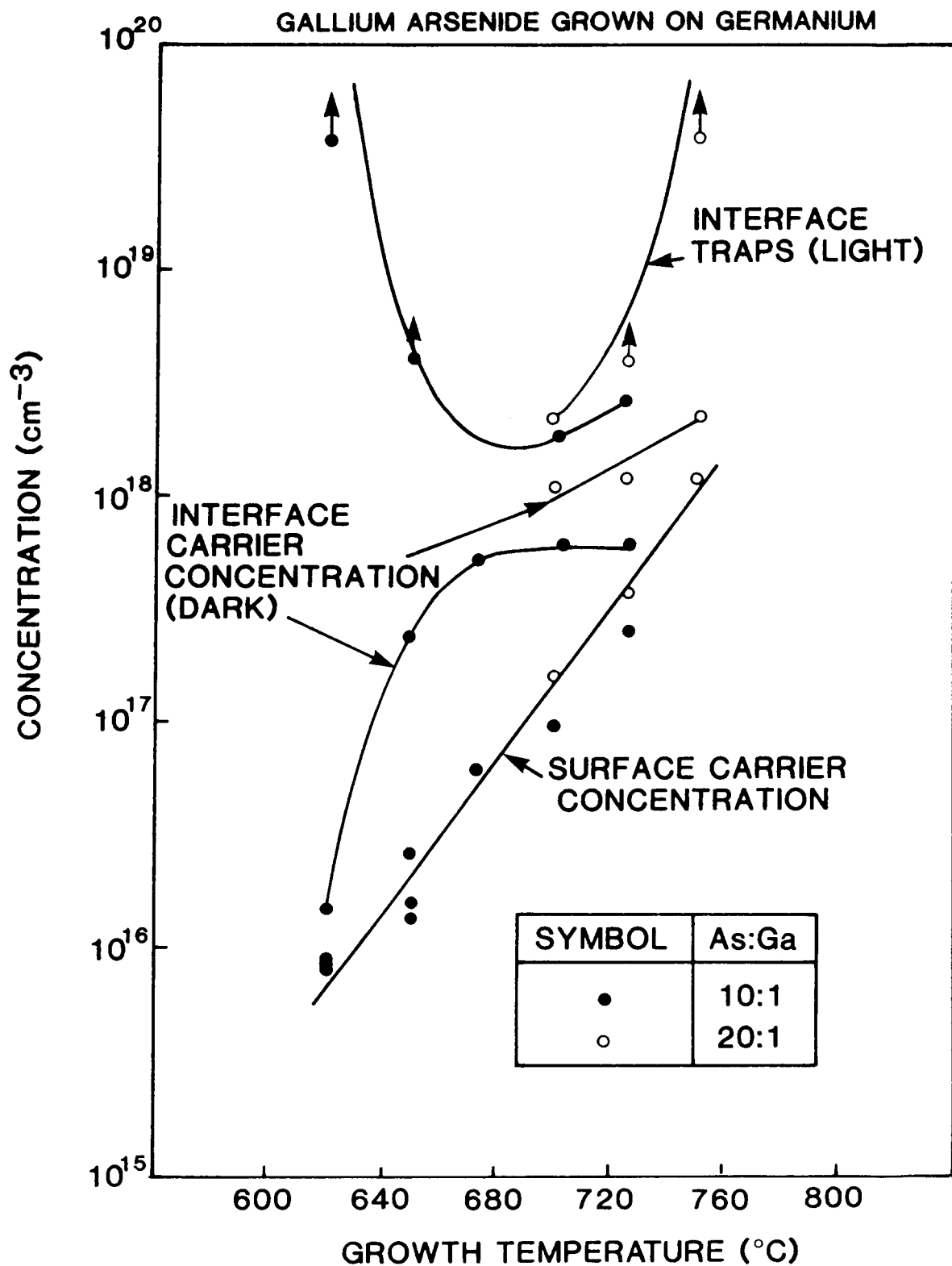


FIGURE 13. Ge AUTODOPING AND INTERFACE TRAP DENSITY AS A FUNCTION OF GROWTH TEMPERATURE. Undoped 3-micron GaAs layers were grown on bare Ge wafers.

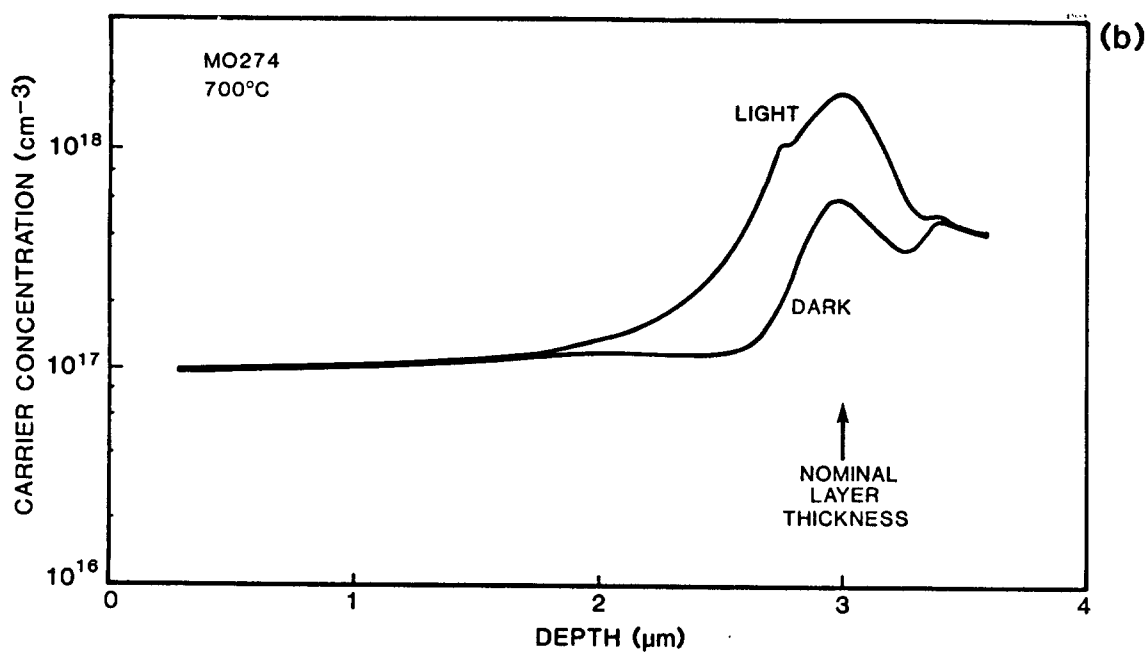
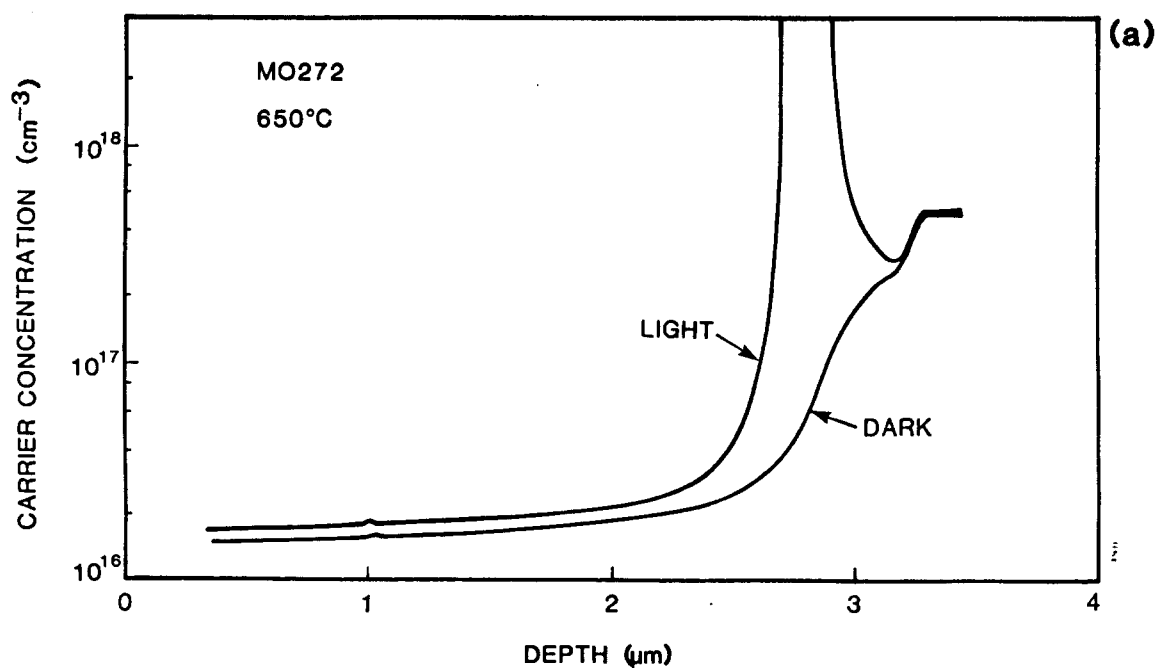


FIGURE 14. POLARON PROFILES OF GaAs LAYERS GROWN ON Ge WAFERS, SHOWING DIFFERENCES BETWEEN ILLUMINATED AND DARK MEASUREMENTS. a) 650°C b) 700°C.

At typical GaAs growth temperatures of 650-700°C the Ge autodoping is less than or comparable to solar cell doping levels. GaAs solar cells could then be grown at the lower temperatures without special provisions for controlling autodoping. This has in fact been done. However, at 800°C, typical of AlGaAs growth, normal cell doping would be impossible.

A factor of 10 reduction in autodoping was realized by coating the backs of the Ge wafers with GaAs prior to growth. A comparison of autodoping with and without backside capping is shown as a function of growth temperature in Figure 15. Typically a 5 micron capping layer of GaAs was grown at 650°C. In this case the autodoping was reduced to insignificant levels for GaAs solar cells, but at 800°C it was still a problem. Further improvements in the capping procedure lowered the Ge autodoping to the mid- 10^{16}cm^{-3} range, even at 800°C. Changes included wafers polished on both sides, 10 micron GaAs layers, and a two-temperature growth on the wafer front in which the first 0.5 micron was grown at 650°C. With this process we were able to grow AlGaAs solar cells on Ge substrates without significant influence of autodoping on the doping profile.

Ge depth profiles in GaAs and AlGaAs cells grown on Ge substrates have been measured by SIMS. Figure 16 compares the Ge profiles in AlGaAs cells grown on Ge and GaAs substrates in the same growth run. (The substrates were on different faces of a barrel-type susceptor). This figure gives good insight into the autodoping process. On Ge substrates, the GaAs and AlGaAs layers within 1 micron of the interface are heavily doped with Ge. On the GaAs substrate there is also a structured Ge profile. This can only occur if Ge is being transported in the gas stream. The Ge level is high at the original substrate surface, presumably from Ge deposited during the heat-up stage. During the growth of the GaAs buffer at the relatively low temperature of 650°C we see little autodoping. More Ge is deposited as the growth is stopped to raise the temperature for AlGaAs growth. In fact, wherever the growth was stopped, on either substrate, there is a pileup of Ge. (The tendency of Ge and Si to form doping spikes when MOCVD growth is interrupted but the dopant flux continues has been noted in the literature⁽⁷⁾). At 800°C there is initially a significant amount of Ge doping, but as growth continues the sources of Ge are covered up and the Ge profile drops to the background level for both substrates. Small spikes in the Ge profile again appear when the growth is halted to change dopants or AlGaAs composition, suggesting that the capping is not perfect. However,

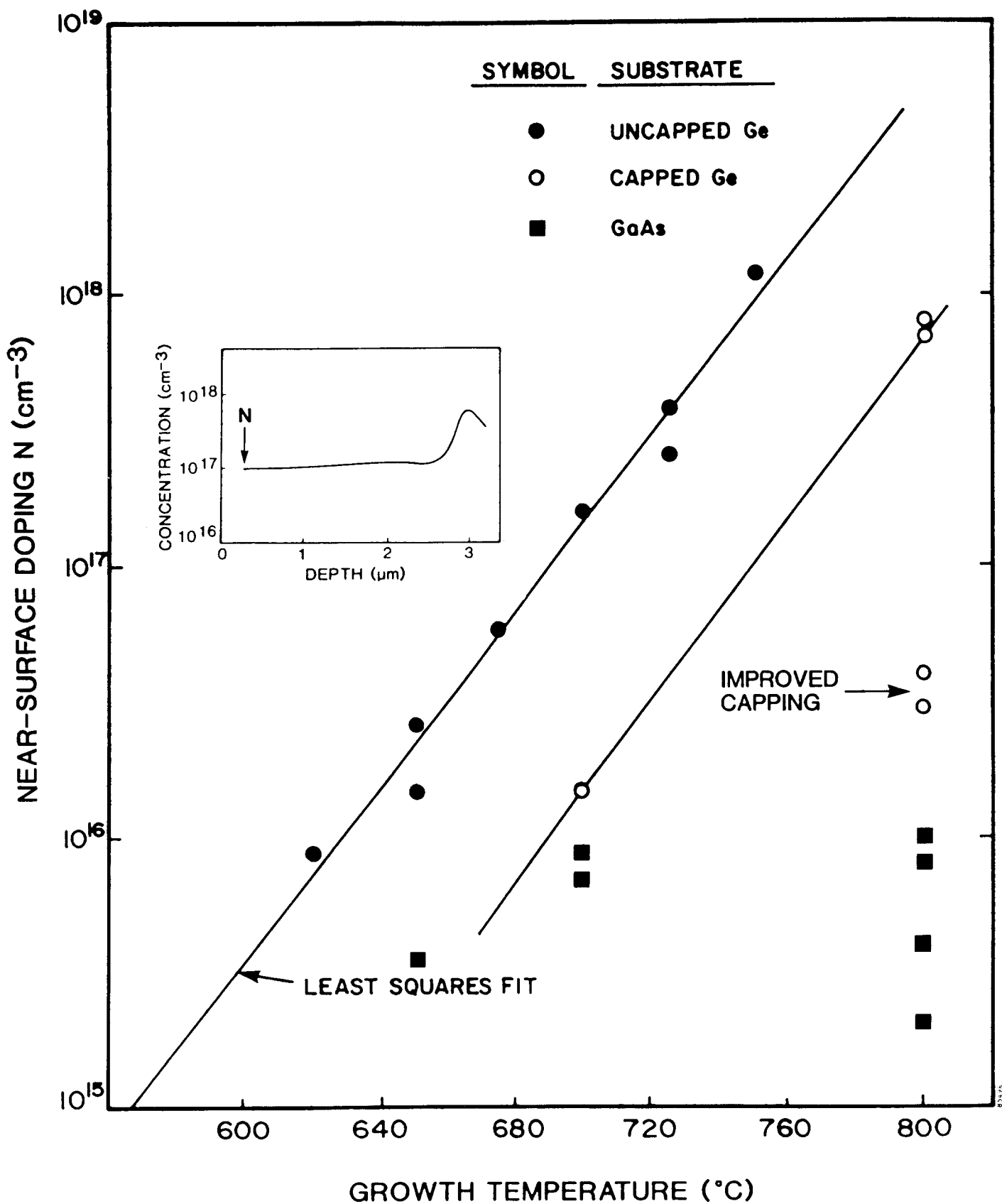


FIGURE 15. Ge AUTODOPING AS A FUNCTION OF TEMPERATURE. Autodoping is greatly reduced by capping the back of the Ge substrate with GaAs.

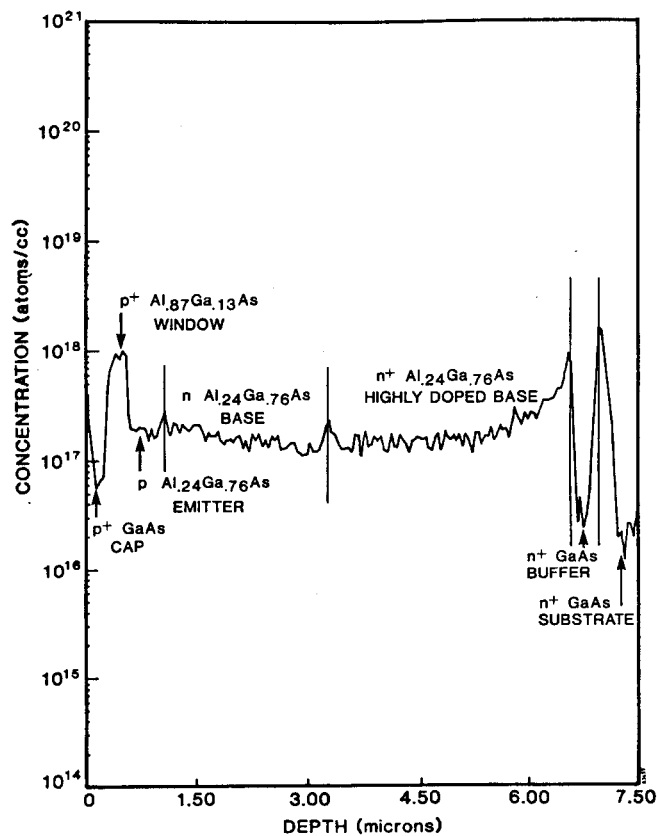
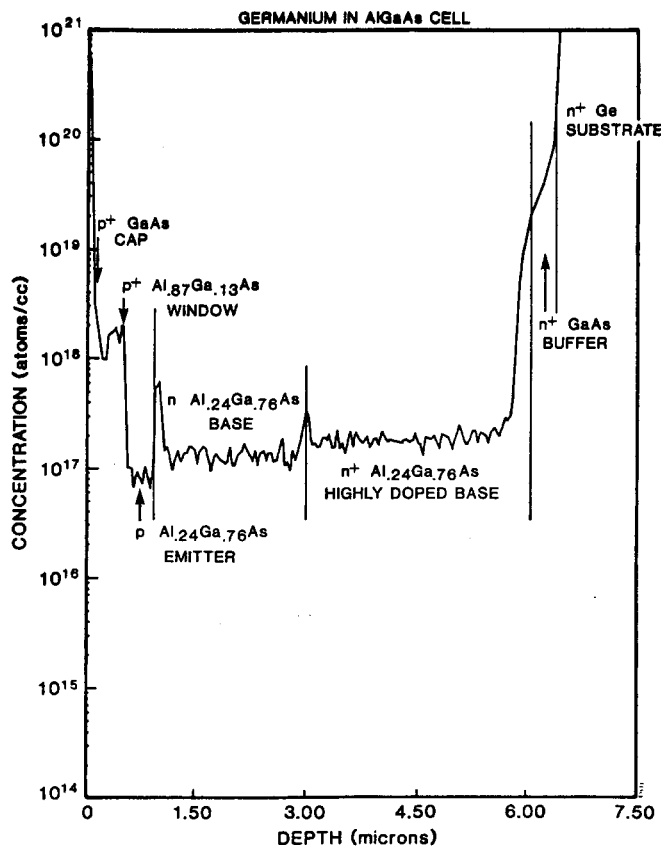


FIGURE 16. SIMS PROFILES OF Ge IN AlGaAs SOLAR CELLS GROWN IN THE SAME RUN. a) Ge substrate b) GaAs substrate.

the overall effect of Ge on the solar cell doping profile is small, except at the rear surface of the cell. In this region the n+ doping is not harmful and in fact may be helpful, providing a minority carrier barrier.

2.5.3 Unintentional Tandem Cell Formation

Another area of concern was doping of the Ge substrate by Ga and As from the epitaxial layers (in our cell structures the first layer grown was GaAs, even for AlGaAs cells). It was anticipated that the surface of the Ge would be doped n-type by indiffusion of As, a much faster diffuser than Ga. However, since the Ge wafer was already heavily n-type, this was not expected to be a problem. In reality there were unexpected consequences of substrate doping by the epitaxial layers.

From the beginning solar cells grown on Ge exhibited anomalously high open circuit voltages and low fill factors (see Section 4.2). This behavior suggested tandem cell operation, with two active junctions in series. Electrical and optical measurements of solar cells did in fact point to an active junction in the Ge substrate (Section 4.2). One early hypothesis was an n-n GaAs-Ge heterojunction. However, considering the band discontinuities in this system, the heterojunction should be forward biased with a positive bias applied to Ge.⁽⁸⁾ The heterojunction photovoltage should then subtract from that of the p-n GaAs homojunction. Experimentally the voltages were found to add, however. This could be explained by formation of a p-n junction in the Ge.

We first looked for evidence of Ga and As diffusion into Ge by SIMS. The high background of Ga and As resulting from sputtering of the overlying GaAs layers made this approach impractical. Better results were obtained by the spreading resistance technique. Although developed for and usually applied to silicon, spreading resistance can also be applied to Ge. The technique involves beveling the sample at a known angle, then measuring the resistance between a set of probes as the probes are translated across the surface. Spreading resistance relies on known calibration samples to convert the measured resistance to resistivity and carrier concentration. Although not as extensive as those used for silicon, calibration samples do exist for Ge.

Figures 17 to 19 show carrier concentration profiles measured for a variety of Ge substrates after growth of epitaxial layers by MOCVD. At low growth temperatures, 650-700°C, the n-type doping shows a buried peak resulting from diffusion of As into Ge. A drop in carrier concentration at the surface is evidence of Ga diffusion, compensating the As-doped layer. There may in fact be an extremely shallow p-n junction in the Ge, beyond the resolution limits of spreading resistance. Results of GaAs solar cells grown in this temperature range certainly suggest a p-n junction. At higher growth temperatures used for AlGaAs cell growth the p-n junction is clearly revealed in the Ge. At these temperatures the junction depth is about 0.5 micron and the As diffusion extends many microns into the Ge. Profiles like Figure 19 were measured for several different AlGaAs cell runs on Ge.

The formation of a Ge p-n junction can be viewed as a general result of the relative diffusion coefficients and solid solubilities of Ga and As in Ge. Figure 20 shows these quantities as a function of temperature, using literature values.^(11,12) At all temperatures of interest arsenic is a faster diffuser but gallium has a higher solubility. A p-type Ga-doped layer then results at the surface, with an n-type As-doped layer beneath it. Using the values in Figure 20 the diffusion profiles of As and Ga were calculated for the growth conditions corresponding to Figures 17 to 19. A complementary error function profile was used with the surface concentration set by the solid solubility at the growth temperature. Comparing the calculated and measured profiles for the AlGaAs cell growth in Figure 19, we see that while both indicate p-n junction formation, the calculated curve shows higher dopings and a shallower junction. This may be a result of concentration-enhanced diffusion at the high doping levels involved. The calibration of the spreading resistance probe at very high doping levels may also be a problem.

Another possibility is that assumed diffusion model may be too simplistic; i.e., GaAs may not act as a limitless source of Ga and As atoms for diffusion into Ge. The self-diffusion coefficients are not very accurately known in GaAs but high-temperature data indicate that they are very low.⁽¹⁸⁾ A consequent depletion of Ga or As near the GaAs-Ge interface could lower the surface concentration on the Ge side below the solid solubility limit. In any case, the existence of the p-n junction is a real concern in the MOCVD growth of GaAs and particularly AlGaAs solar cells on Ge.

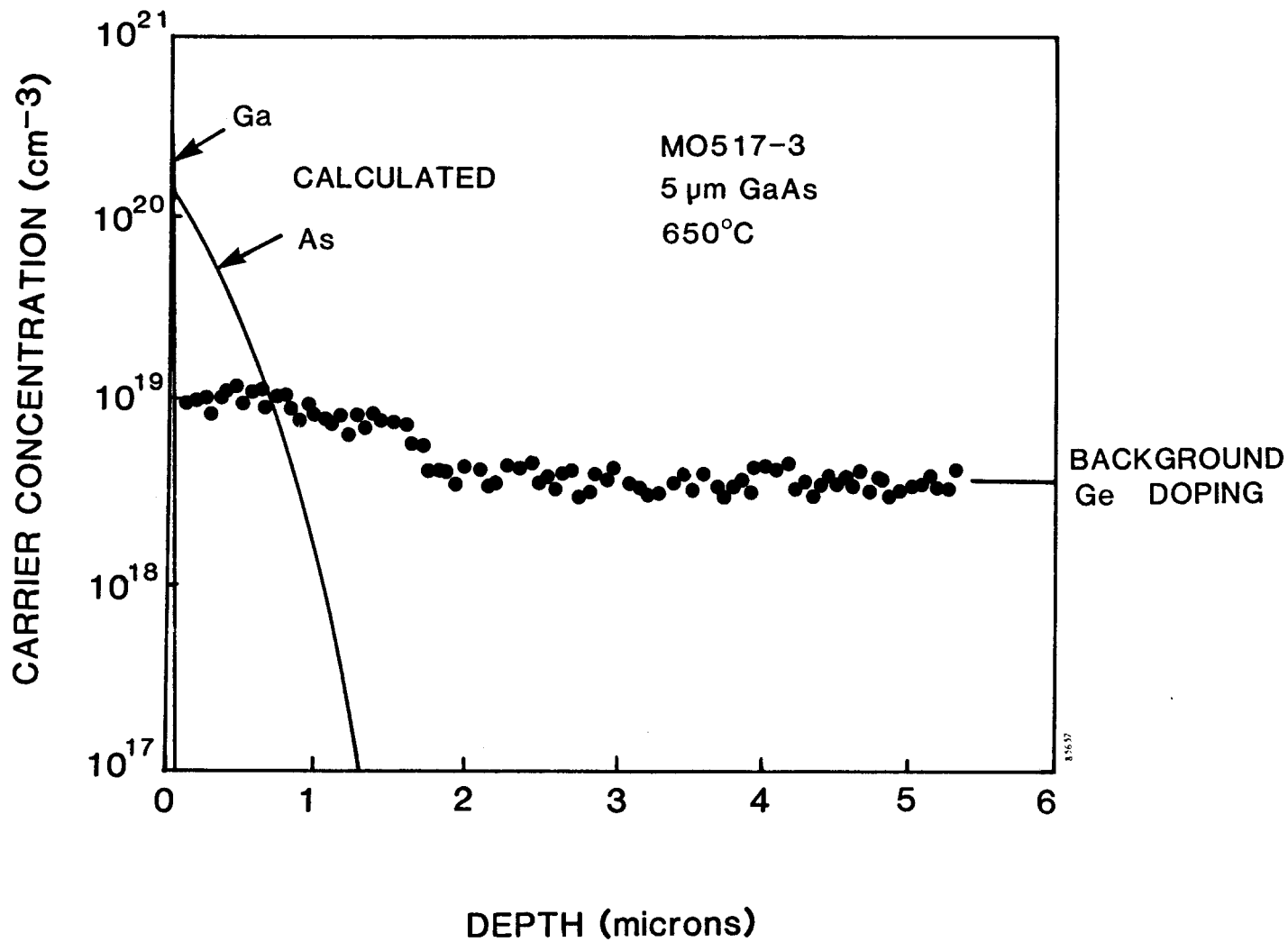


FIGURE 17. DOPING PROFILE IN A Ge SUBSTRATE AFTER GROWTH OF A 5 MICRON GaAs EPITAXIAL LAYER AT 650°C.

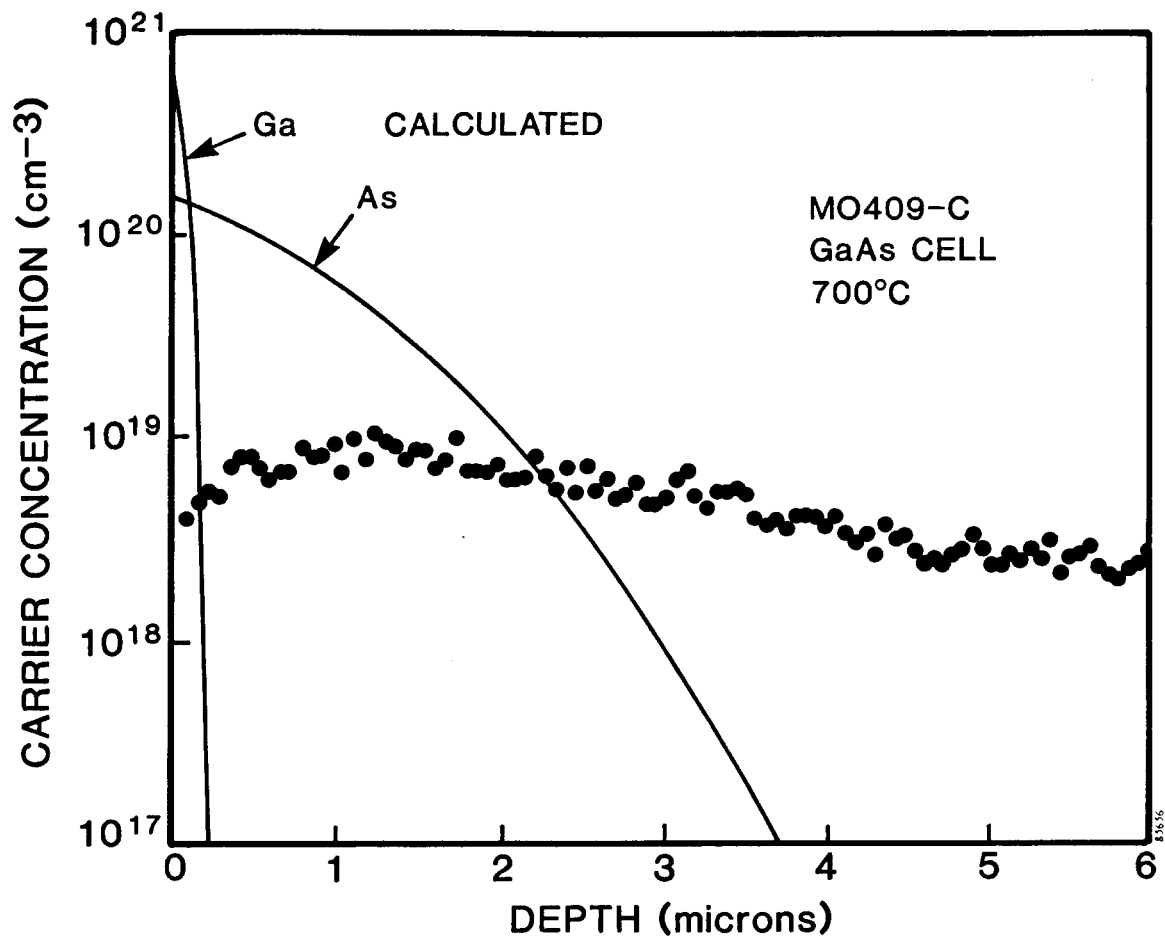


FIGURE 18. DOPING PROFILE IN A Ge SUBSTRATE AFTER GROWTH OF A GaAs SOLAR CELL AT 700°C.

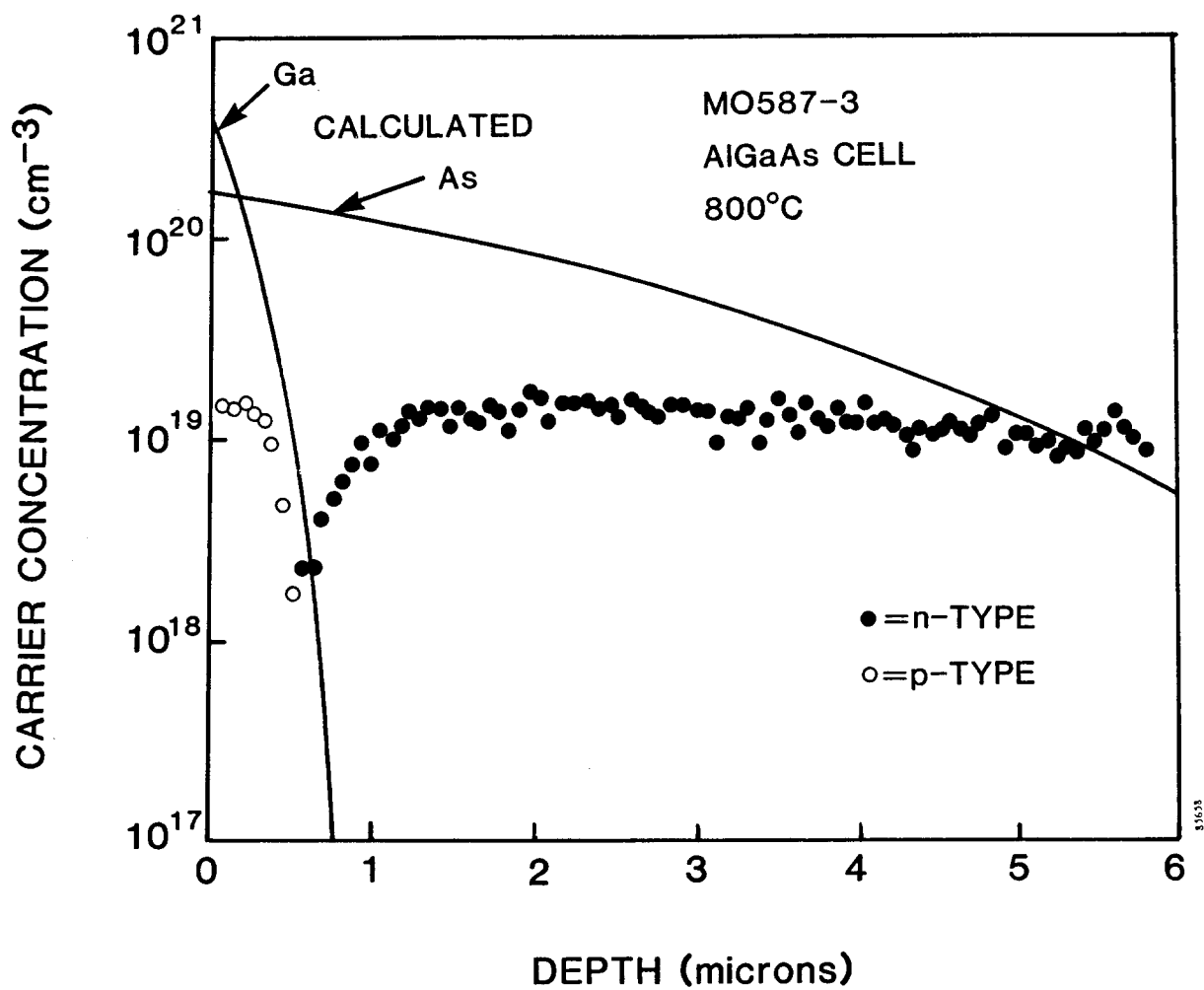


FIGURE 19. DOPING PROFILE IN A Ge SUBSTRATE AFTER GROWTH OF AN AlGaAs SOLAR CELL AT 800°C. The measured profile is from spreading resistance measurements; the calculated profile used the Ga and As parameters from Figure 20.

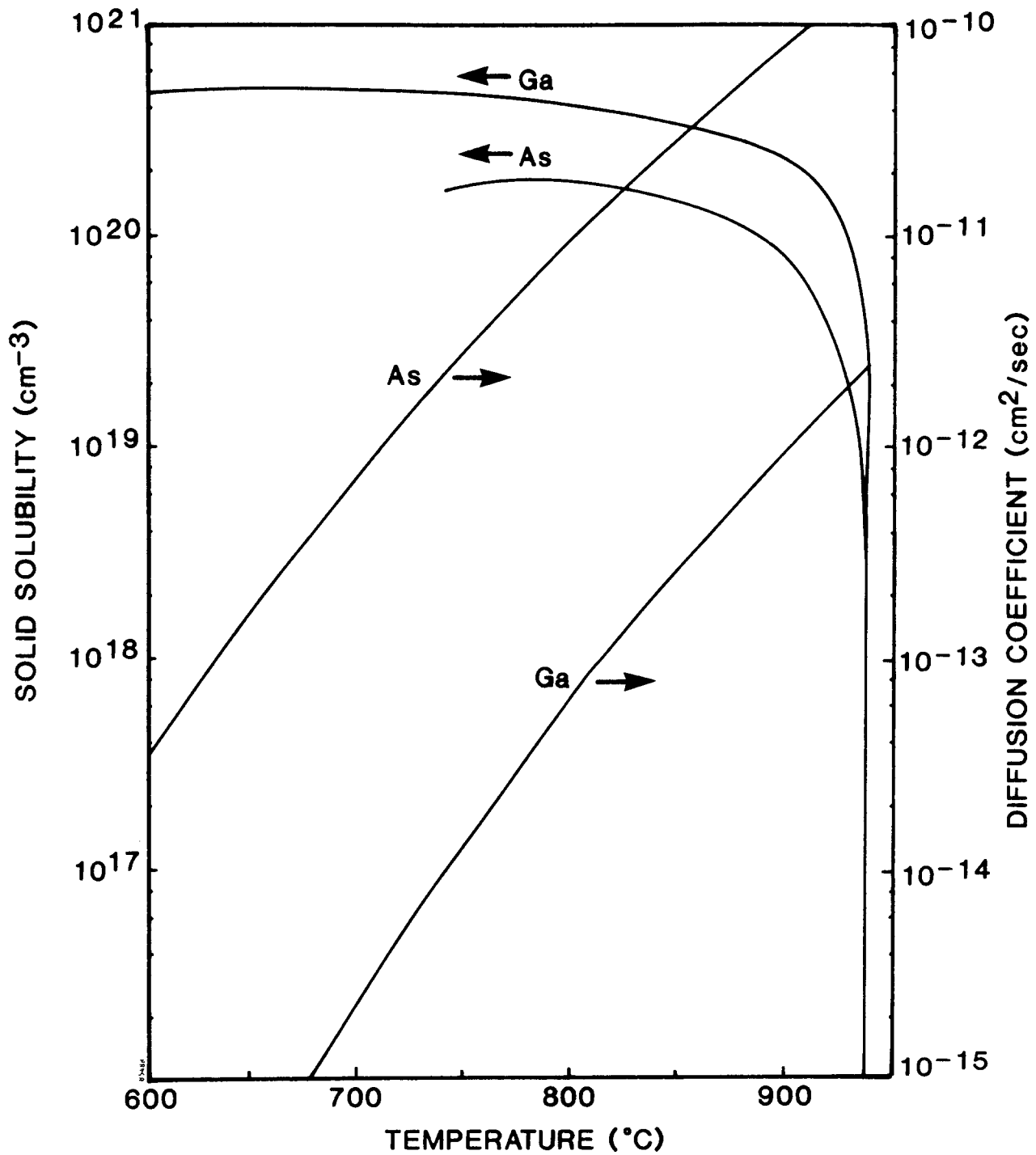


FIGURE 20. MATERIAL PROPERTIES FOR Ga AND As IMPURITIES IN Ge, AS A FUNCTION OF TEMPERATURE. Solid solubilities are from Trumbore (12) and diffusion coefficients are from Sze (11).

From a pragmatic point of view, the Ge p-n junction is no longer a problem once the substrate is removed from the AlGaAs cell. We have also found that the quality of the Ge junction varies considerably from cell to cell; in some cases it is so poor that it has little effect on the cell characteristics. Thus although the Ge junction is a nuisance in terms of intermediate characterization of the solar cells, it is not a real limitation for producing thin AlGaAs cells. Elimination of the Ge p-n junction would require very low growth temperatures, not compatible with high quality AlGaAs growth in present MOCVD systems. Advances in low temperature AlGaAs growth may be forthcoming as the sources of deep recombination levels, such as oxygen, become better understood. At low growth temperatures the Ga-doped layer may be so thin as to have no effect; reports in the literature suggest that this is the case.⁽⁹⁾

2.5.4 Defect Structure in Epitaxial Layers on Ge

A third area of investigation was the defect structure of GaAs and AlGaAs layers grown on Ge substrates. Although Ge and GaAs are closely matched in lattice constant and thermal expansion coefficient, there is finite mismatch present. A 3-micron GaAs layer grown on a capped Ge wafer was examined by Transmission Electron Microscopy (TEM) to characterize the defect structure. The growth sequence simulated an AlGaAs cell growth, with 0.5 micron grown at 650°C then 2.5 micron at 800°C. The only defects were isolated threading dislocations at a density of 10^5 to 10^6 cm⁻². A TEM micrograph of a dislocation is shown in Figure 21. The measured density agrees with Kasano's x-ray topography results for GaAs on Ge.⁽¹⁰⁾ For comparison, the density of dislocations is comparable to that found in GaAs substrates grown by the Liquid Encapsulated Czochralski technique. It is not clear whether or not this dislocation density is high enough to affect the minority carrier diffusion length in the cell. We have noted that short circuit current densities are slightly smaller in solar cells grown on Ge than on GaAs substrates when grown and processed identically. A higher dislocation density is one possible explanation. No evidence was found by TEM of antiphase domains, a concern when growing polar semiconductors on a nonpolar substrate.⁽¹³⁾ It has been reported by several authors that slight misorientation of the substrate away from the (100) orientation suppresses the formation of antiphase domains when growing GaAs on Ge.^(14, 15) Our results, using substrates oriented 2 degrees from (100), are in agreement with this finding.

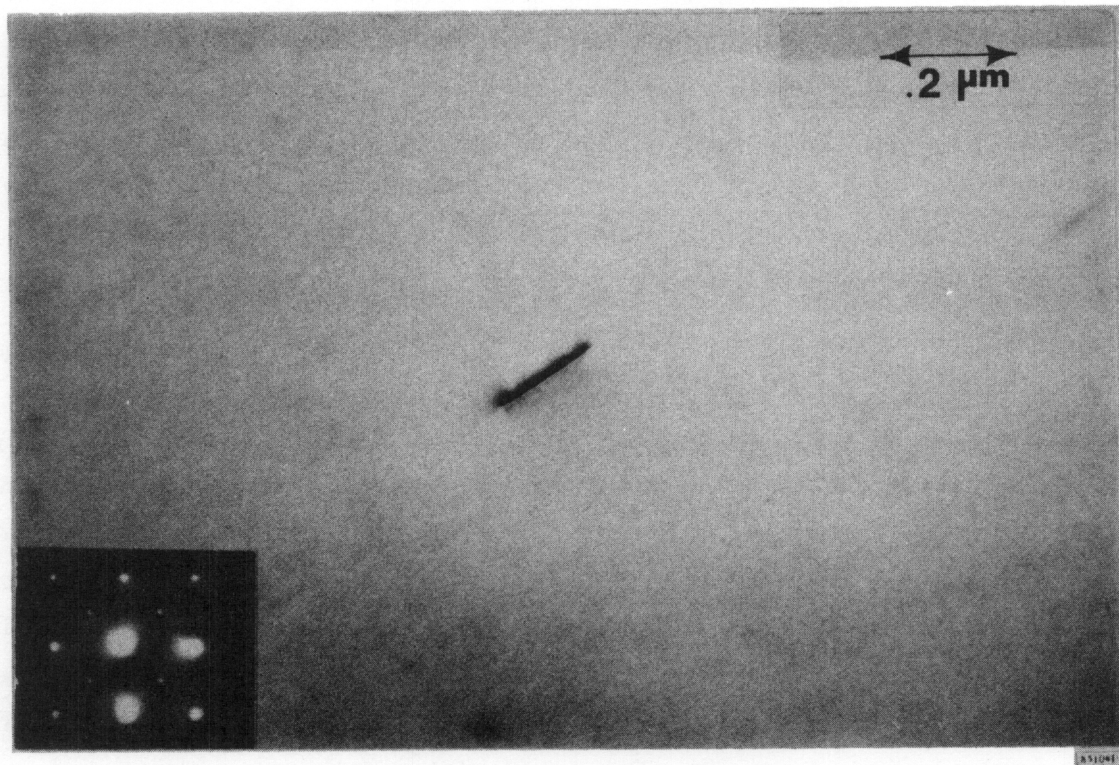


FIGURE 21. TEM MICROGRAPH OF AN ISOLATED THREADING DISLOCATION IN GaAs GROWN ON A Ge SUBSTRATE.

SECTION 3

PROCESS DEVELOPMENT

3.1 CONCENTRATOR CELL GRID DESIGN

The grid pattern for the concentrator cell was designed analytically to provide the maximum efficiency given certain input conditions. After consultation with Dave King at Sandia a circular cell with a diameter of 1.00 cm and a concentration ratio of 500 was selected. The light intensity was assumed to be uniformly distributed across the cell, although this is not required in our design code. A radial pattern of grid lines was chosen, with uniform line width.

The grid design equations are given in Appendix A. Assumed parameters input to the model are listed in Table 2. The cell parameters are those of a 20.3% efficient GaAs one-sun cell, scaled to 500 suns operation.

TABLE 2. PARAMETERS INPUT TO THE GRID DESIGN MODEL

Parameter	Value
Current density at maximum power point	12.08 A/cm ² (active area)
Voltage at maximum power point	1.056 V
Resistivity of metal	2.6 x 10 ⁻⁶ ohm-cm
Grid line aspect ratio	3:1 width:height
Sheet resistance of emitter	400 ohms per square
Specific contact resistance	<1x10 ⁻⁵ ohm-cm ²

The resulting grid consisted of eight tiers of radial lines with concentric rings connecting the outer four tiers. The rings connect discontinuous lines in successive tiers and also provide redundancy in case of line breaks. Calculated losses and cell parameters are listed in Table 3. A photograph of the grid pattern on a thin AlGaAs concentrator cell is also shown in Figure 22.

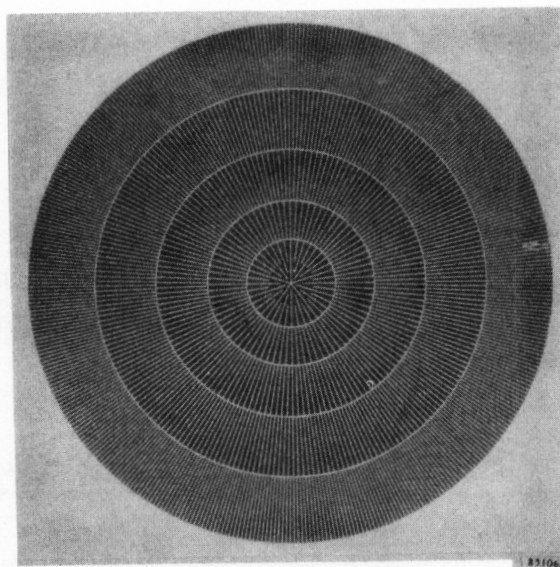


FIGURE 22. PHOTOGRAPH OF THE 1 CM DIAMETER GRID PATTERN ON A THIN AlGaAs CONCENTRATOR CELL.

TABLE 3. RESULTS OF CONCENTRATOR CELL GRID DESIGN

Parameter	Value
Grid line width	7.0 micron
Grid line height	2.3 micron
Total shadow loss	9.6%
Line resistance loss	4.3%
Sheet resistance loss	2.5%
Contact resistance loss	0.1 %
GaAs cell: J_{\max}	10.9 A/cm ²
V_{\max}	0.983 V
Efficiency	21.4%

The design calculations were done using parameters for an existing GaAs cell. There is considerable room for improvement in the short circuit current of the cell, so that the calculated efficiency is a conservative estimate. The model was also conservative in the calculation of series resistance losses, assuming that all losses combine linearly. Efficiencies in excess of the calculated 21.4% are therefore expected.

A separate grid design optimization for AlGaAs cells was not done. The major differences between GaAs and AlGaAs cells are the increased emitter sheet resistance and the lower operating currents of AlGaAs, which tend to cancel. It was felt that the added cost of a second photomask set was not worth the small efficiency increment at this stage of development.

3.2 CONCENTRATOR CELL FRONT SIDE PROCESSING

Front side solar cell processing consisted of grid metallization, junction definition, cap removal, and antireflection coating. The individual steps are listed in Table 4. The process was identical for GaAs and AlGaAs cells, whether or not they were to be thinned.

One of the major limitations on concentrator cell efficiency during this program has been excessive grid shadow caused by overly wide grid lines. Figure 23 shows the shadow loss as a function of the grid line width for the concentrator cell grid pattern.

TABLE 4. CONCENTRATOR CELL FRONT SIDE PROCESSING

1. Deposit Silox layer, 0.3 micron
2. Photolithography to define grid pattern
3. Etch Silox in buffered HF
4. Evaporate AuZn ohmic contact layer, 0.2 micron
5. Liftoff photoresist to define grid
6. Sinter contacts, 250°C for 5 min in N₂
7. Electroplate Au, 3 micron
8. Etch Silox in buffered HF
9. Photolithography to define cell area
10. Mesa etch in 2 H₂O: 1 H₂O₂: 1 HCl
11. Remove photoresist
12. Selective etch to remove GaAs cap, 190 H₂O₂: 10 NH₄OH: 6 1% EDTA
13. Evaporate tantalum pentoxide antireflection coating

The design values were 7 microns and 9.6% shadow; values up to 20 microns and 26% shadow have been observed. The primary problems were poor control of the photoresist liftoff process, over-etching of the Silox layer allowing the plated metal to be considerably wider than the evaporated line, and mushrooming during plating of the grid lines. The process was considerably improved by the end of the program, with typical line widths of 12 microns. Work still remains to be done in this area, however.

3.3 Ge SUBSTRATE REMOVAL

The first step in substrate removal was to bond the cell to a Corning 0211 glass cover slide. Cells had been previously sawed from the Ge wafer with a high speed diamond saw, leaving squares several mm larger than the cell mesa area. Dow Corning Sylgard 182 silicone adhesive was used, applied according to the manufacturer's specifications. The procedure was to apply a drop of adhesive to the center of the cell, then place the cover glass upon it. Excess adhesive and any air bubbles were worked out to the edge of the glass. The adhesive was cured in air at 100°C for one hour.

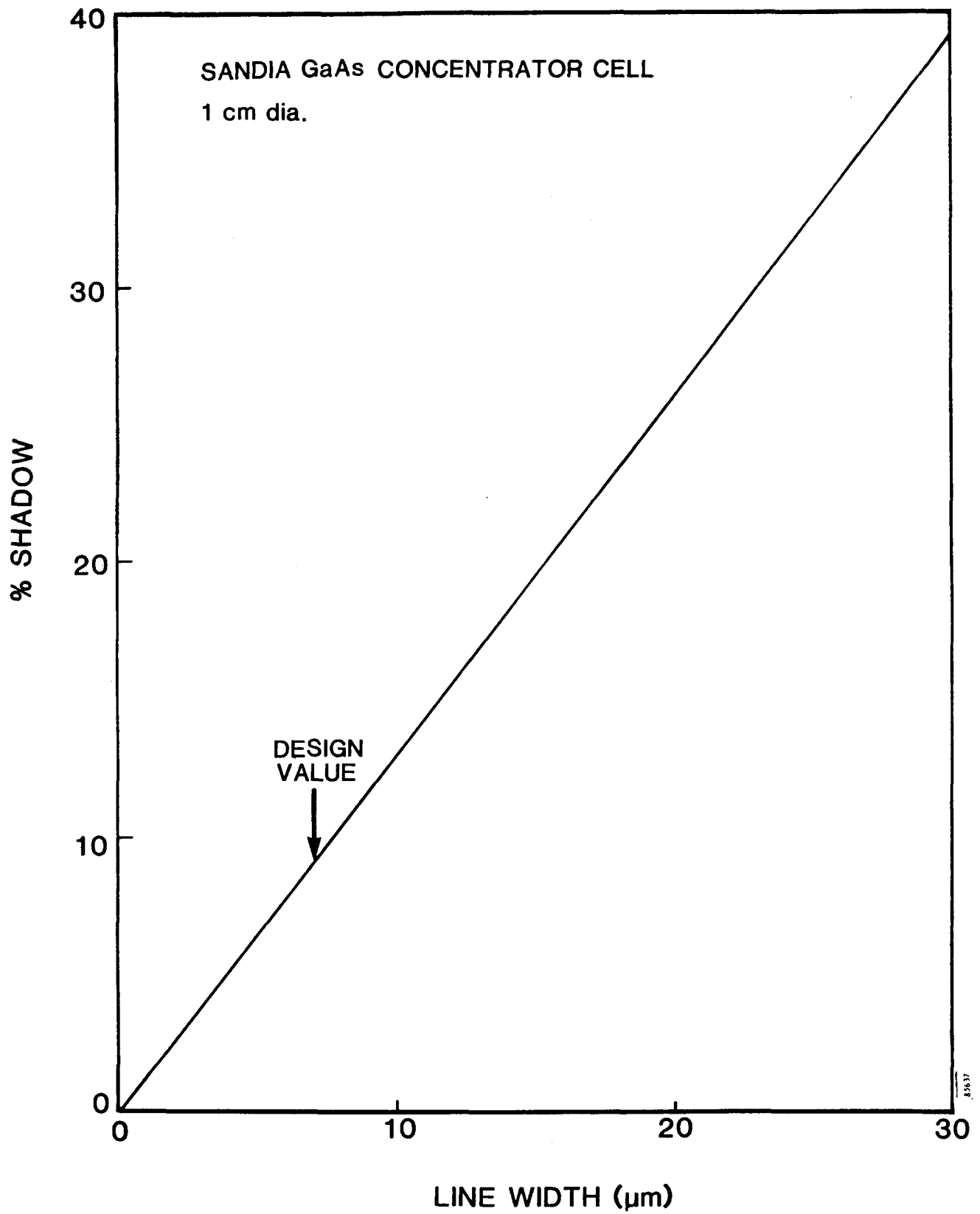


FIGURE 23. GRID SHADOW LOSS AS A FUNCTION OF LINE WIDTH FOR THE 1 CM DIAMETER CONCENTRATOR CELL.

The Ge growth substrates were completely removed by a two-stage etching process. Prior to etching, the edges of the cell were protected by black wax. This was found necessary to prevent attack of the front side of the cell by HCl in the first etchant. The first etching step employed a nonselective etchant, 10 H₂O₂ : 1 HCl, to remove most of the germanium substrate. The etching reaction is exothermic, and can reach the boiling point if higher concentrations of HCl are used. For a 10% solution a steady state temperature of about 60°C was reached. In this solution the etch rate of Ge is about 0.6 micron/min. After the cell was thinned to about 50 microns, a slower selective etchant removed the remainder of the Ge. The selective etchant consisted of H₂O₂ at a temperature of 55°C. To prevent trapping of bubbles during the etching process the cover glass was placed in an inclined position in a beaker of etchant. The solution was also vigorously stirred during the process. The cover glass was rotated several times during etching to achieve a more uniform etch. Because hot hydrogen peroxide decomposes fairly rapidly, the etch rate of Ge is difficult to quantify. Usually the sample was placed in a beaker of fresh etchant and allowed to etch overnight. This normally resulted in complete removal of the substrate. Because the etchant does not attack GaAs, over etching was not a concern.

3.4 BACK SIDE PROCESSING OF THIN CELLS

Back side processing involved putting a metallization grid on the back of the cell, making electrical contact to the grids on both sides of the cell, and antireflection coating of the back side. First the black wax and excess adhesive, originally around the edge of the Ge substrate but now separated by a small gap from the active solar cell, was removed. Photolithography was then used to define a grid pattern in photoresist on the back of the cell. A non-contact lithography system was used to avoid damaging the thin cell. Using the photoresist as a mask, AuSn contacts were electroplated. The same grid pattern was used on both sides of the cell, but no attempt was made to align the grids front-to-back. After removing the photoresist the cell was sintered at 275°C for 10 min in N₂ to produce ohmic back contacts. Access to the grid pattern on the front of the cell was gained by etching away one or more corners of the cell. Black wax was used as a mask for the 2 H₂O : 1 H₂O₂ : 1 HCl etchant. After removing the cell layers the front metallization was exposed, supported by the adhesive. To make electrical contact to the cell for testing purposes, silver ribbons were attached with conductive silver epoxy (Epotek H2OE). The epoxy was cured at 90°C for 90 min. The cells were too fragile to permit mechanical probing.

For the thin GaAs cell described in Section 4.5 the process ended here. AlGaAs cells, however, required removal of the back GaAs contact layer between the grid lines. The same cap removal process used for the front of the cell was used for the back. After the contact layer was removed the back of the cell was antireflection coated with 620 Å of e-beam evaporated tantalum pentoxide. The antireflection coating was not optimized to provide lower reflection in the wavelength region between the bandgaps for silicon and AlGaAs. For the thin AlGaAs cell reported in Section 4.6, with concentrator grid patterns and antireflection coatings on both sides, the final step was to attach silver ribbons as described above. To lower the series resistance four ribbons were attached to the front grid in the corners and four to the back grid at the midpoint of each side. Cells were mounted with the glassed side facing up using the cover glass for mechanical support. Photographs of the front and back of a complete thin AlGaAs cell are shown in Section 4.6.

SECTION 4

TEST RESULTS

4.1 GaAs CELLS ON GaAs SUBSTRATES

GaAs cells on GaAs substrates provided a baseline of comparison for AlGaAs cells and for Ge substrates. Relatively few GaAs cells were processed, mostly at the beginning of the program. The I-V characteristics of a one-sun GaAs cell processed before the beginning of this program are shown in Figure 24. An efficiency over 20% and an open circuit voltage over 1 volt are indicative of the high quality GaAs material grown in our MOCVD reactor.

GaAs cells were used to check out the concentrator grid pattern described in Section 3.1. Measurements made at Sandia on one of these cells, number 454D-S1, gave the following results at one sun:

V_{oc}	.976 V
J_{sc}	22.9 mA/cm ²
FF	.828
Efficiency	18.5%

The major efficiency limitation of this cell was the short circuit current density, which should be about 25 mA/cm² for a GaAs cell. The internal quantum efficiency measured by Sandia is shown in Figure 25. Here the internal quantum efficiency is defined as the external quantum efficiency divided by one minus the total reflectance measured with an integrating sphere. The cell has a high quantum efficiency over a wide wavelength range, indicating high material quality. Excessive shadow loss caused by wide grid lines is the major reason for the decreased short circuit current.

When the same cell was measured under concentrated sunlight a peak efficiency of 19.0% was reached at 3.7 suns. A high series resistance was responsible for a rolloff in fill factor at low concentrations. The series resistance was in turn caused by high contact resistance, as measured by a transmission line test pattern on the same wafer.

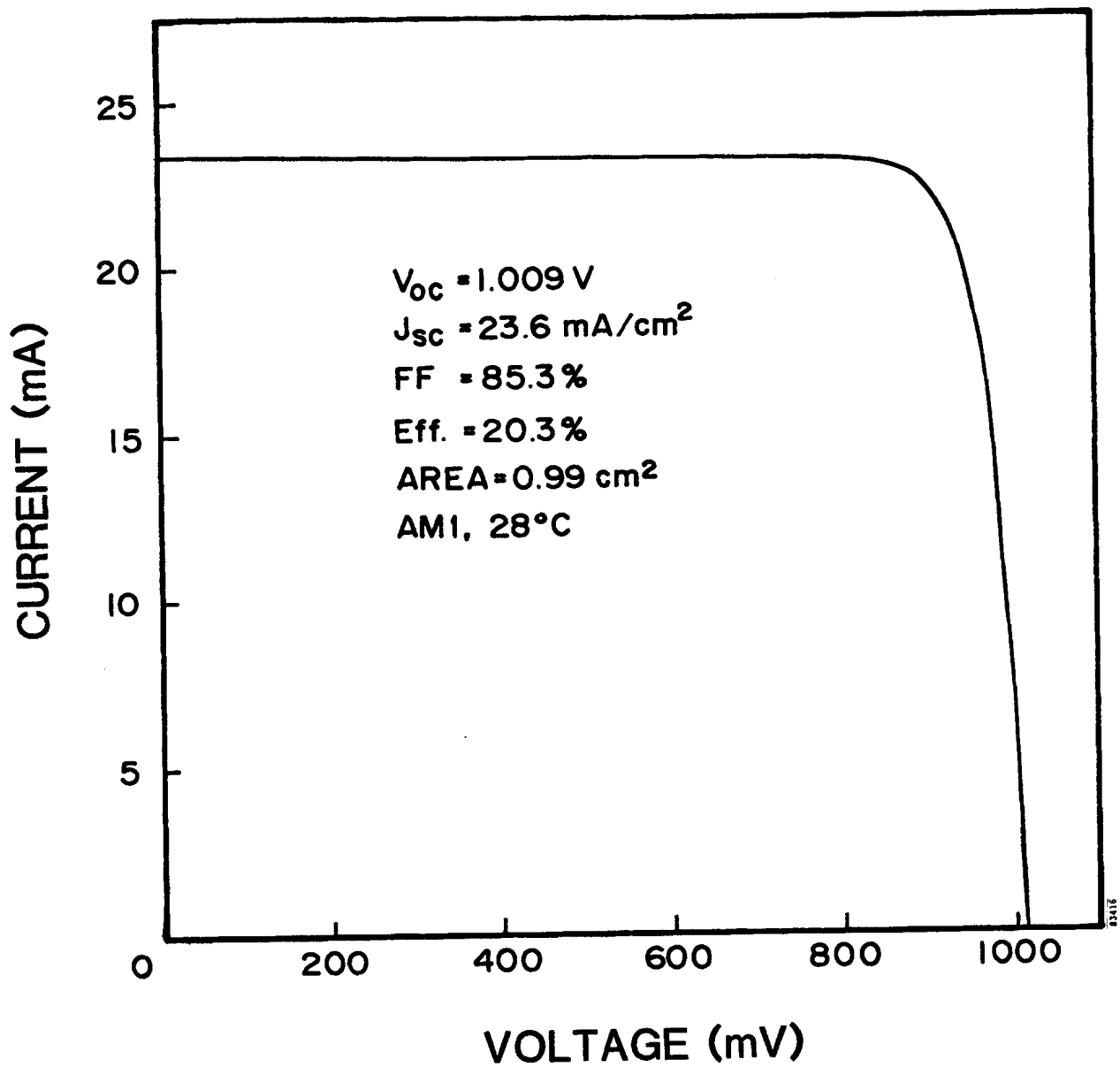


FIGURE 24. GaAs ONE-SUN CELL WITH EFFICIENCY OF 20.3%.

SAMPLE ID: SPIRE MO 454D-S1

DATE: 09/06/84 11:45:56 AM MST

QUANTUM EFFICIENCY

0% SHADOWING

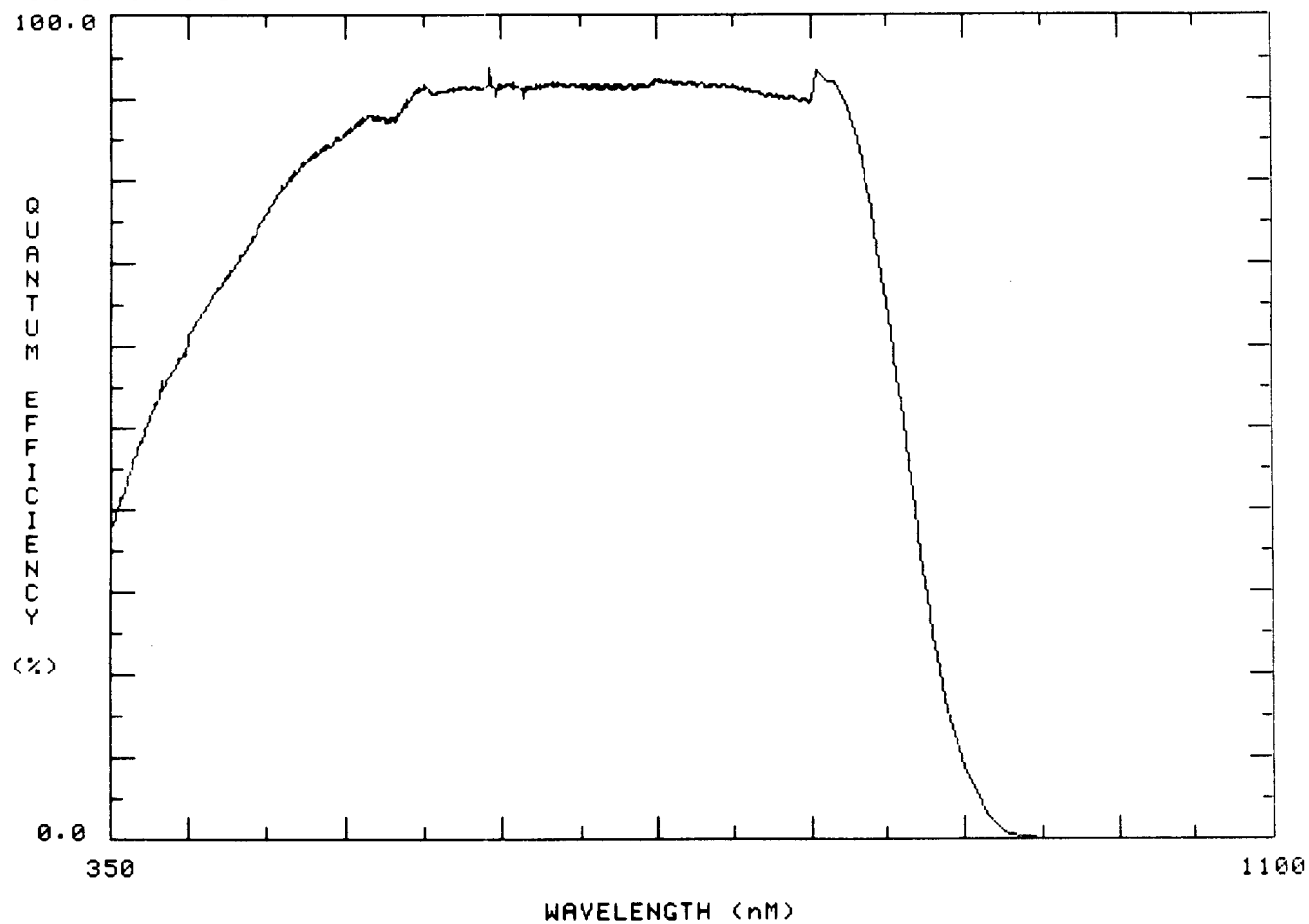


FIGURE 25. INTERNAL QUANTUM EFFICIENCY FOR A GaAs CONCENTRATOR CELL, AS MEASURED BY SANDIA.

The two problems preventing the cell from achieving its design efficiency are both attributable to immature processing technology in the early stages of the program when this cell was produced. As discussed in Section 3.2, the grid technology was improved later in the program, reducing the shadow loss. The contact resistance problem was subsequently solved by increasing the doping in the GaAs contact layer. Although the remainder of the program was devoted to AlGaAs cell development, it is clear that baseline GaAs concentrator cells could have been produced with efficiencies close to the design value.

4.2 GaAs CELLS ON Ge SUBSTRATES

It was quickly discovered that cells grown on germanium substrates were different from those on gallium arsenide substrates. A comparison of one-sun I-V curves for GaAs solar cells grown on Ge and GaAs substrates in the same growth run is shown in Figure 26. The cells on Ge have similar short circuit currents to those on GaAs, but anomalously high open circuit voltages and low fill factors. This behavior is representative of a large number of solar cells. Insight into the difference can be obtained from the log I vs. V characteristics in Figure 27. On GaAs substrates the junction characteristics are well behaved, with an ideality factor shifting from 2 at low voltages toward 1 at high voltages. On Ge substrates the ideality factor is about 4.5 over most of the curve. In addition the illuminated and dark I-V characteristics do not agree.

These results can be understood by postulating an active junction in the Ge substrate, forming an unintentional tandem cell structure. In a series-connected tandem the ideality factor is approximately the sum of the ideality factors of the two subcells, explaining the poor fill factors. The photovoltages of the two cells add, explaining the high V_{oc} . The rather small V_{oc} increment over a GaAs cell (about 100 mV) and the high ideality factors implied for the Ge junction point to a Ge junction of poor quality.

The I-V characteristics of the Ge junction were measured directly using the test device shown in Figure 28. In this 3 terminal cell structure the GaAs and Ge junctions could be examined independently. A photovoltage and photocurrent were measured for the Ge substrate, although the junction quality was poor. It was also confirmed that the apparent enhancement of the GaAs cell V_{oc} was caused by the Ge junction.

SUBSTRATE	V_{oc}	J_{sc}	FF	Eff.
GaAs	1000	22.9	78.8	18.1
Ge	1082	22.3	68.0	16.4

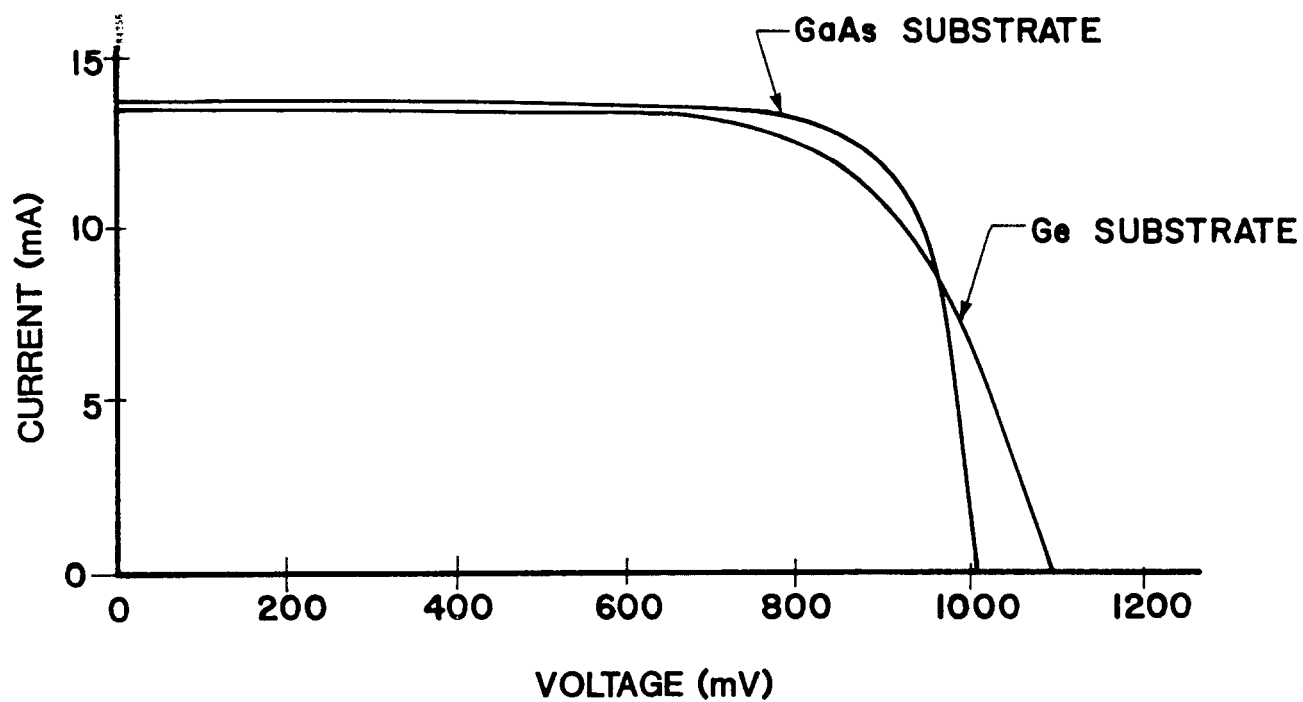


FIGURE 26. COMPARISON OF GaAs SOLAR CELLS GROWN ON GaAs AND Ge SUBSTRATES IN THE SAME MOCVD RUN.

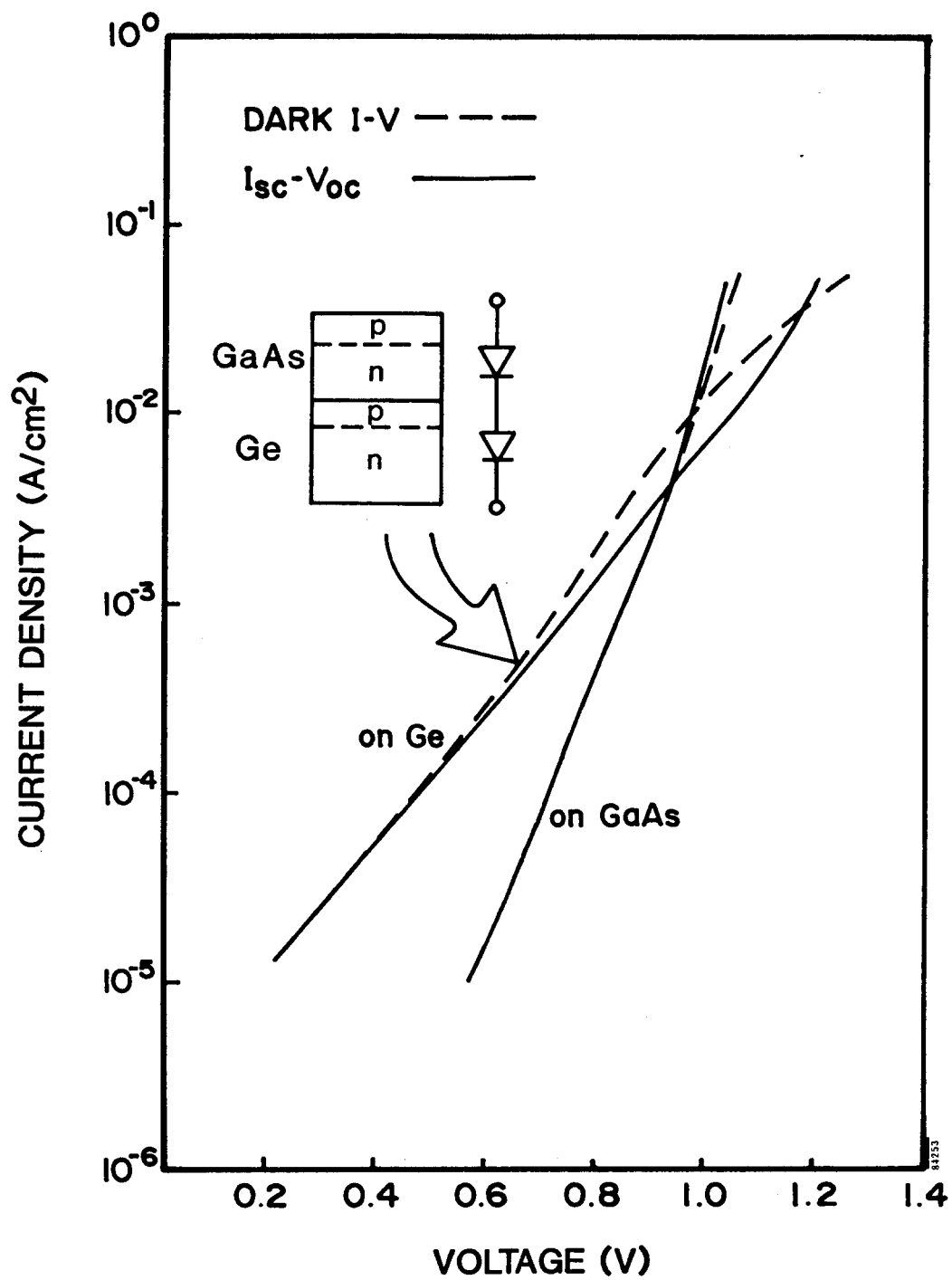


FIGURE 27. LOGARITHMIC CURRENT-VOLTAGE CHARACTERISTICS FOR THE SOLAR CELLS OF FIGURE 26.

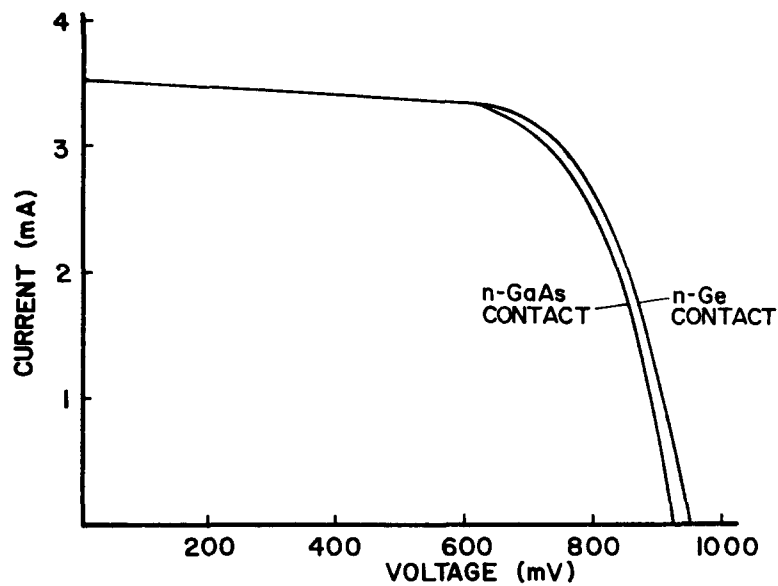
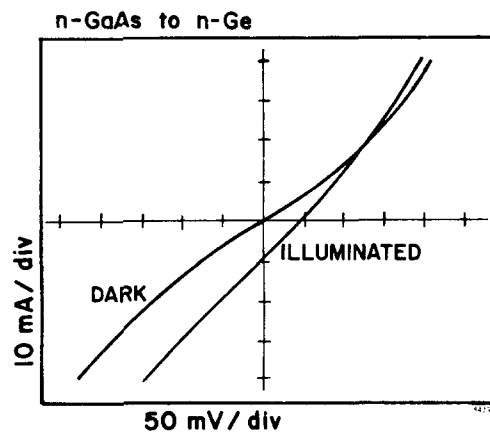
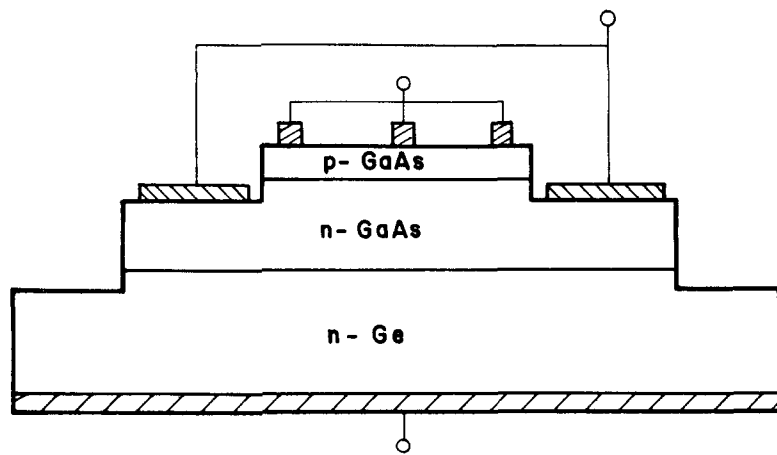


FIGURE 28. 3-TERMINAL CELL STRUCTURE USED TO EXAMINE THE CHARACTERISTICS OF A GaAs SOLAR CELL GROWN ON A Ge SUBSTRATE. (a) DEVICE STRUCTURE, (b) I-V CHARACTERISTICS OF THE Ge SUBSTRATE MEASURED FROM FRONT TO BACK, (c) I-V CHARACTERISTICS OF THE GaAs CELL MEASURED WITH AND WITHOUT THE Ge SUBSTRATE.

Further evidence of an active Ge junction was obtained for cells in which the GaAs junction was short-circuited. The spectral response of these cells turned on at 870 nm, the normal cutoff for GaAs, and continued to well beyond 1000 nm, as would be expected for Ge. For such cells the apparent quantum efficiency was often well over 1.0. The reason is a large collection area for the Ge junction, much larger than the GaAs cell area. The mesa etch used to define the GaAs cells did not etch through the Ge junction; thus the whole wafer acted as one large Ge solar cell. We found experimentally that for cells in which the GaAs junction was short circuited photocurrent could be collected by shining light far away from the cell. This explains why the short circuit current of the tandem cell was not limited by the Ge subcell. Even without this area-related effect, however, the large leakage current of the Ge junction would prevent the Ge subcell from limiting the short circuit current of the tandem.

It should be noted that we have seen no evidence of a blocking junction at the n^+ GaAs- p^+ Ge heterojunction. This could be due to the high cross-doping at the interface, or to crystal defects.

With unintentional tandem cell effects controlling the V_{oc} and fill factor of the cells on Ge substrates, it was difficult to compare the quality of the cells to ones grown on GaAs substrates. The short circuit currents, however, could be compared by assuming that the GaAs subcell limited J_{sc} . Table 5 compares the short circuit current densities for cells grown on GaAs and Ge substrates in the same growth run. It can be seen that J_{sc} is consistently somewhat smaller on Ge substrates, but within 5% for the best cells. The difference might be due to threading misfit dislocations in the GaAs grown on Ge substrates, at densities of 10^5 to 10^6 per cm^2 . Another possibility is larger size crystal imperfections caused by incomplete cleaning of the Ge substrates. Cells grown on Ge substrates were usually more defective than those on GaAs substrates when viewed with an optical microscope.

The highest efficiency achieved for a GaAs cell on a Ge substrate was 16.4% at one sun, as shown in Figure 26.

TABLE 5. COMPARISON OF SHORT CIRCUIT CURRENT DENSITIES FOR GaAs CELLS GROWN ON GaAs AND Ge SUBSTRATES IN THE SAME RUN.

MOCVD Run	Best J_{sc}		Mean J_{sc}		# of cells	
	on Ge	on GaAs	on Ge	on GaAs	on Ge	on GaAs
226	22.5	23.6	22.5	23.1	1	6
409	23.2	24.1	21.9	23.2	6	4

4.3 AlGaAs CELLS ON GaAs SUBSTRATES

One of the best AlGaAs concentrator cells produced during the program was number 628B-S2A. The data obtained by Sandia from 1 to 1000 suns and by Spire at 1 and 15 suns are shown in Figures 29 - 31. The figures plot efficiency, V_{oc} , and fill factor, respectively, as functions of concentration. Table 6 summarizes Sandia and Spire measurements at one sun. Note that Sandia data in the figures has not been corrected for spectral mismatch error. This would raise the short circuit current, and to first order also the efficiencies, by 1.4%.

TABLE 6. COMPARISON OF SPIRE AND SANDIA MEASUREMENTS AT ONE SUN FOR AlGaAs CONCENTRATOR CELL 628B-S2A.

Measured by:	Mismatch corrected?	Temp. (C)	V_{oc} (V)	J_{sc} (mA/cm ²)	FF (%)	Eff (%)
Spire	No	28	1.145	12.93	84.2	12.47
Sandia	No	27.9	1.135	12.08	83.2	11.4
Sandia	Yes			12.25		

The efficiency of the cell peaked at 13.5% at 242 suns concentration. (The corrected value is 13.7%). Another cell on the same wafer had similar characteristics, with a peak efficiency of 13.3% at 317 suns. Both cells had efficiencies slightly under 12% at 1000 suns. The behavior at high concentrations is much improved over the GaAs cell discussed in Section 4.1. The reason is much higher zinc doping in the GaAs cap layer, leading to lower contact resistance. Measured contact resistances on this wafer were in the 10^{-5} ohm-cm² range, consistent with the design value.

The open circuit voltages and fill factors of these cells were both very good for a 1.69 eV bandgap cell. The high quality of the junction and the low series resistance of the cell can be seen in the log I-V characteristics of Figure 32. Over the range shown the dark I-V and I_{sc} - V_{oc} curves are coincident, indicating negligible series resistance. The actual series resistance measured by Sandia at high concentrations was 24 milliohms. By comparing the log I-V data and the V_{oc} vs. concentration data of Figure 33 it can be seen that the ideality factor of the junction is 1.3 over a range of 0.2 to 100 suns. Above 100 suns the ideality factor approaches 1.0.

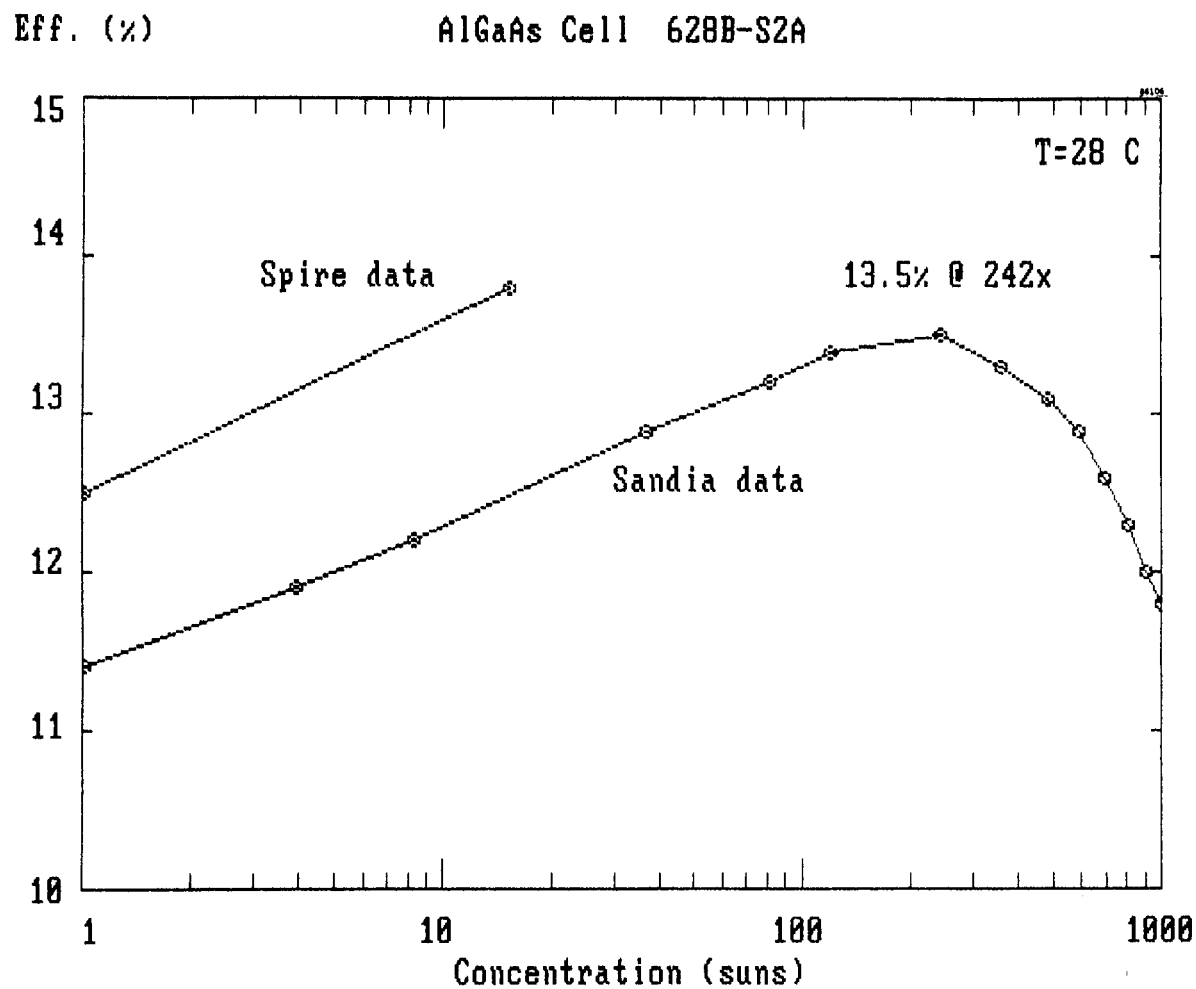


FIGURE 29. EFFICIENCY VERSUS CONCENTRATION FOR AlGaAs CELL 628B-S2A. Differences in calibration of one-sun J_{SC} accounts for the difference between Spire and Sandia measurements.

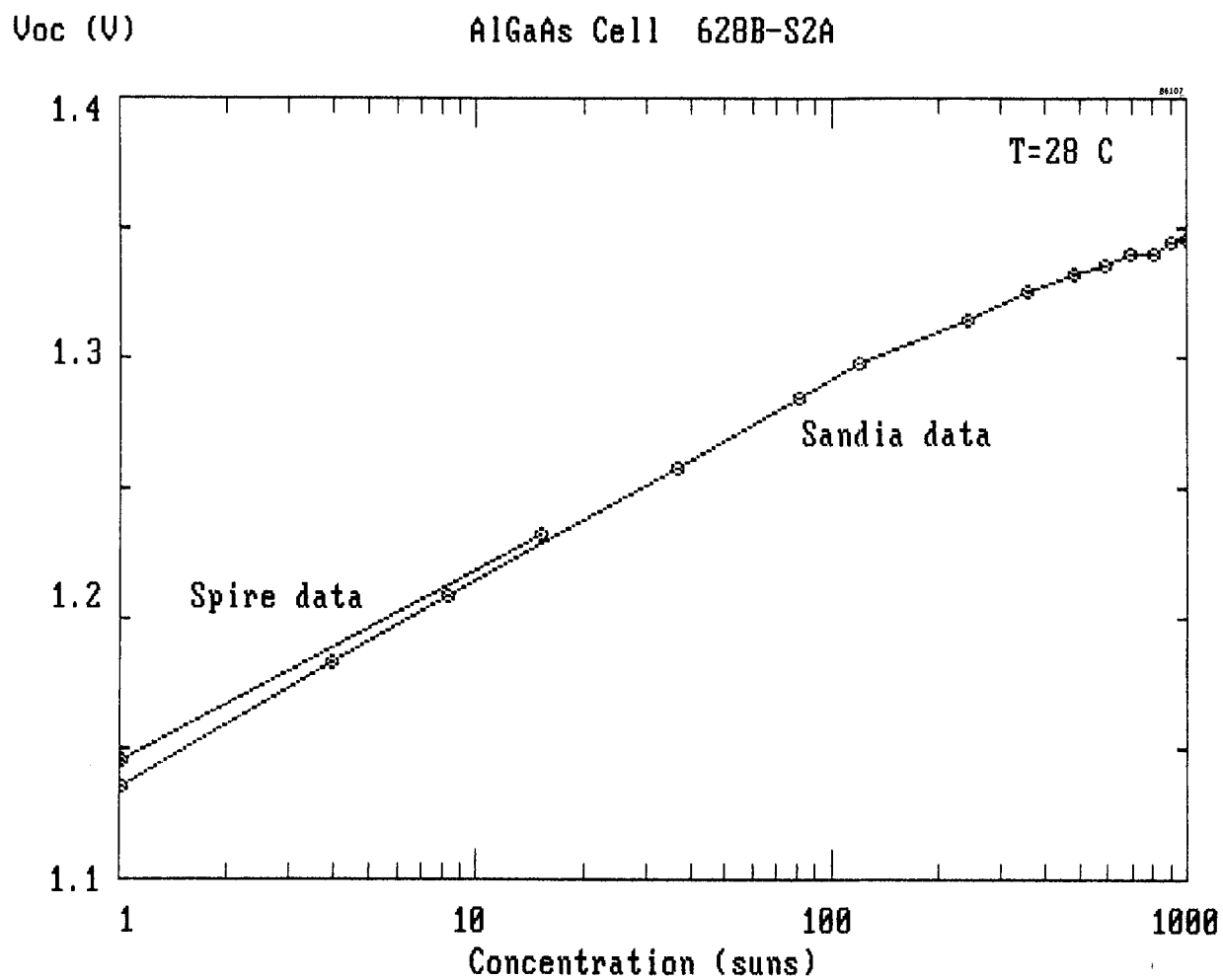


FIGURE 30. OPEN CIRCUIT VOLTAGE VERSUS CONCENTRATION FOR AlGaAs CELL 628B-S2A. The bandgap of the AlGaAs material is 1.69 eV.

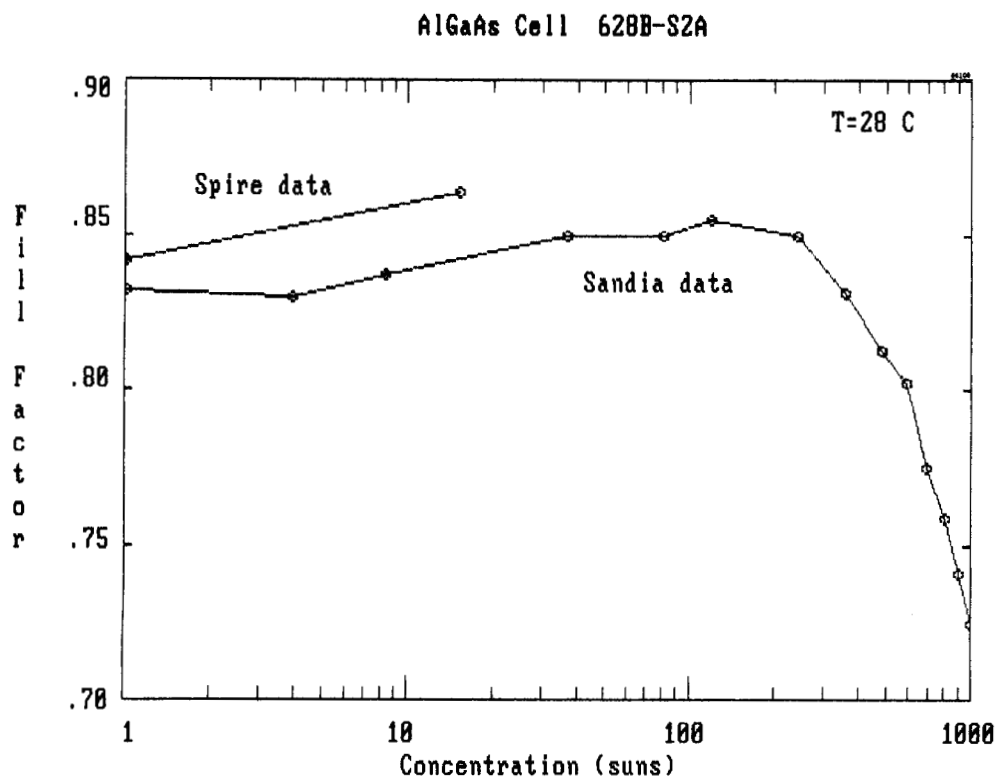


FIGURE 31. FILL FACTOR VERSUS CONCENTRATION FOR AlGaAs CELL 628B-S2A.

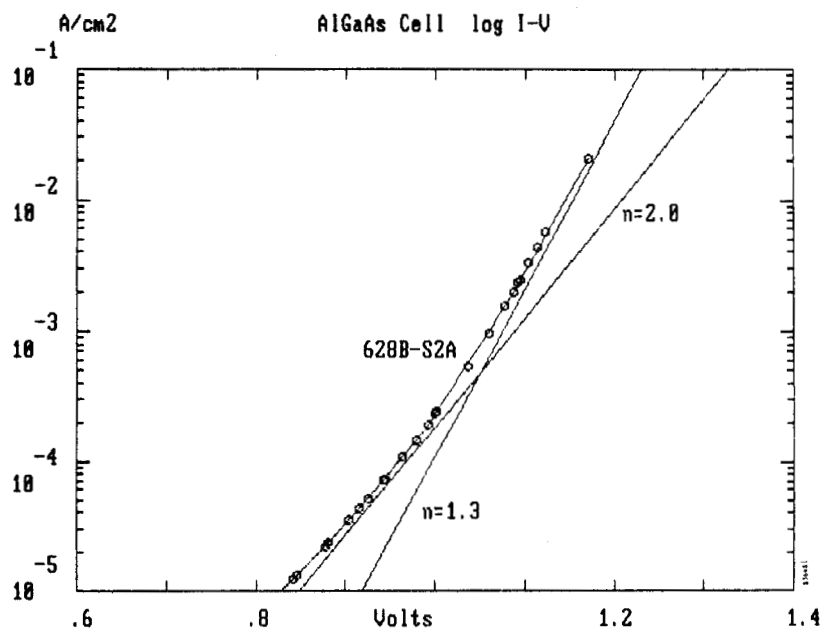


FIGURE 32. LOG I vs. V CHARACTERISTICS FOR CELL 628B-S2A. The illuminated and dark curves coincide over the range shown.

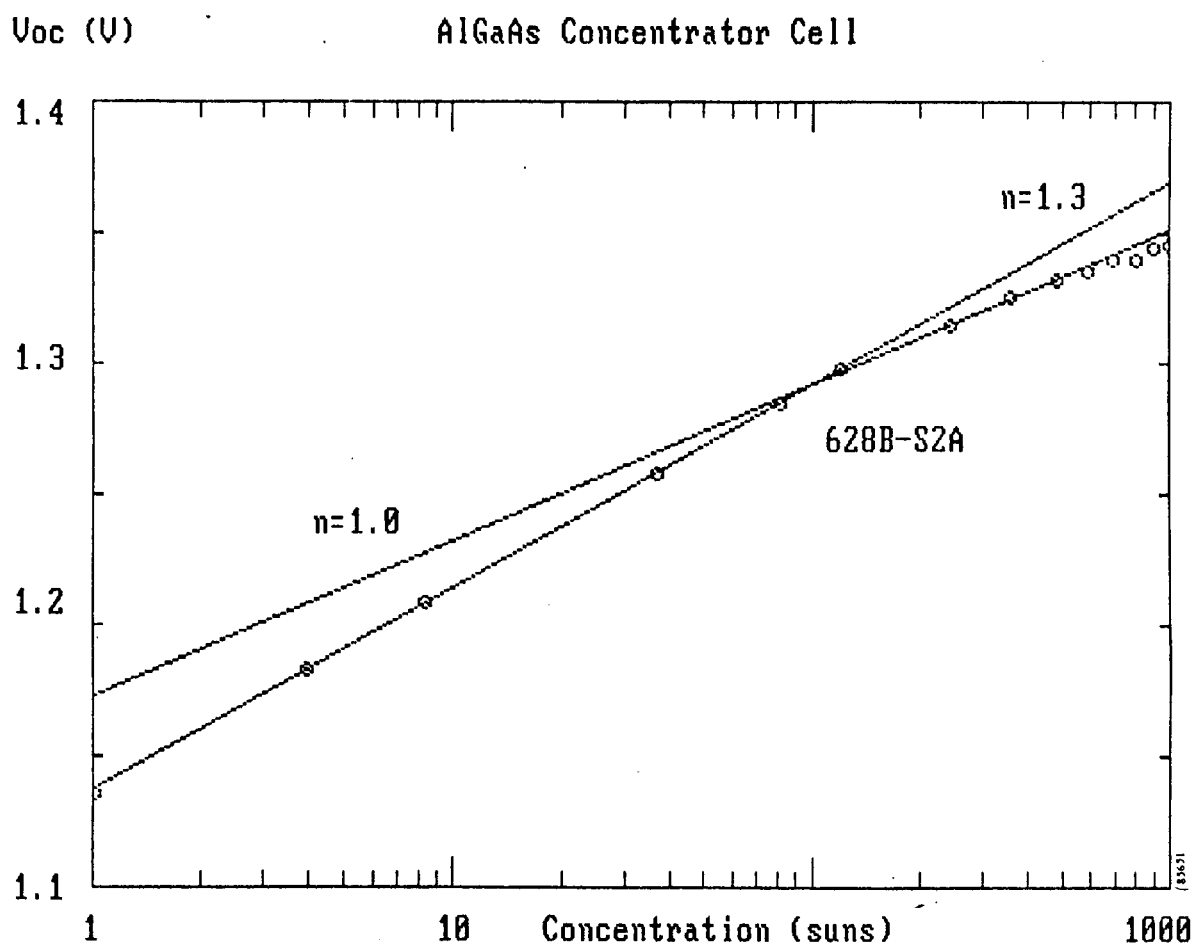


FIGURE 33. OPEN CIRCUIT VOLTAGE AS A FUNCTION OF CONCENTRATION FOR AlGaAs cell 628B-S2A. Slopes corresponding to diode ideality factors of 1.0 and 1.3 are compared to the measured data.

The major limitation on the efficiency of cell 628B-S2A was the short circuit current density. Limitations on J_{sc} resulted both from material quality and processing limitations. Overly wide grid lines were responsible for a substantial shadow loss and reduction in short circuit current. Measured grid line widths of 16.5 microns correspond to a shadow loss of 22.6%, compared to design values of 7 microns and 9.6%. Short minority carrier diffusion lengths also contributed to low J_{sc} . Figure 34 presents the cell internal spectral response and total reflectance measured by Sandia. As mentioned previously, the internal response was calculated by dividing the measured external response by one minus the measured hemispherical reflectance. For this procedure to accurately account for shadow loss the reflectance of the grid lines must be 1, independent of wavelength. Apparently this is not the case for this cell, because the minimum reflectance of 4% is much smaller than the measured shadow loss of 23%. An approximate correction can be made by scaling the "internal" QE by $(1-.19)^{-1}$ to account for an extra grid shadow of 19%. The corrected peak internal quantum efficiency is then 89%.

The gradual rolloff in the blue and red ends of the spectrum and the peak response less than 1 are indicative of short diffusion lengths in the AlGaAs material (relative to the thickness of the layers). Modeling of the quantum efficiency gave values of 0.7 and 0.5 micron for diffusion lengths in the emitter and base layers, respectively. This can be compared to values of 0.67 and 0.22 micron derived from the literature for AlGaAs material of comparable composition and doping [16]. Thus although the diffusion lengths in the AlGaAs cell are small relative to GaAs values, they in fact compare favorably with what has been observed by others.

There was about a one percentage point discrepancy in the efficiencies measured at Spire and Sandia. This is accounted for mostly by uncertainties in calibration of the short circuit current, which was 5-6% higher at Spire. Spectral mismatch corrections necessitated by the use of a silicon reference cell to set the simulator intensity can account for most of the discrepancy. (The mismatch factor calculated for Spire's measurement would decrease the short circuit current by about 1.9% for the ASTM 1985 Global spectrum and 10.8% for the ASTM 1985 Direct spectrum).

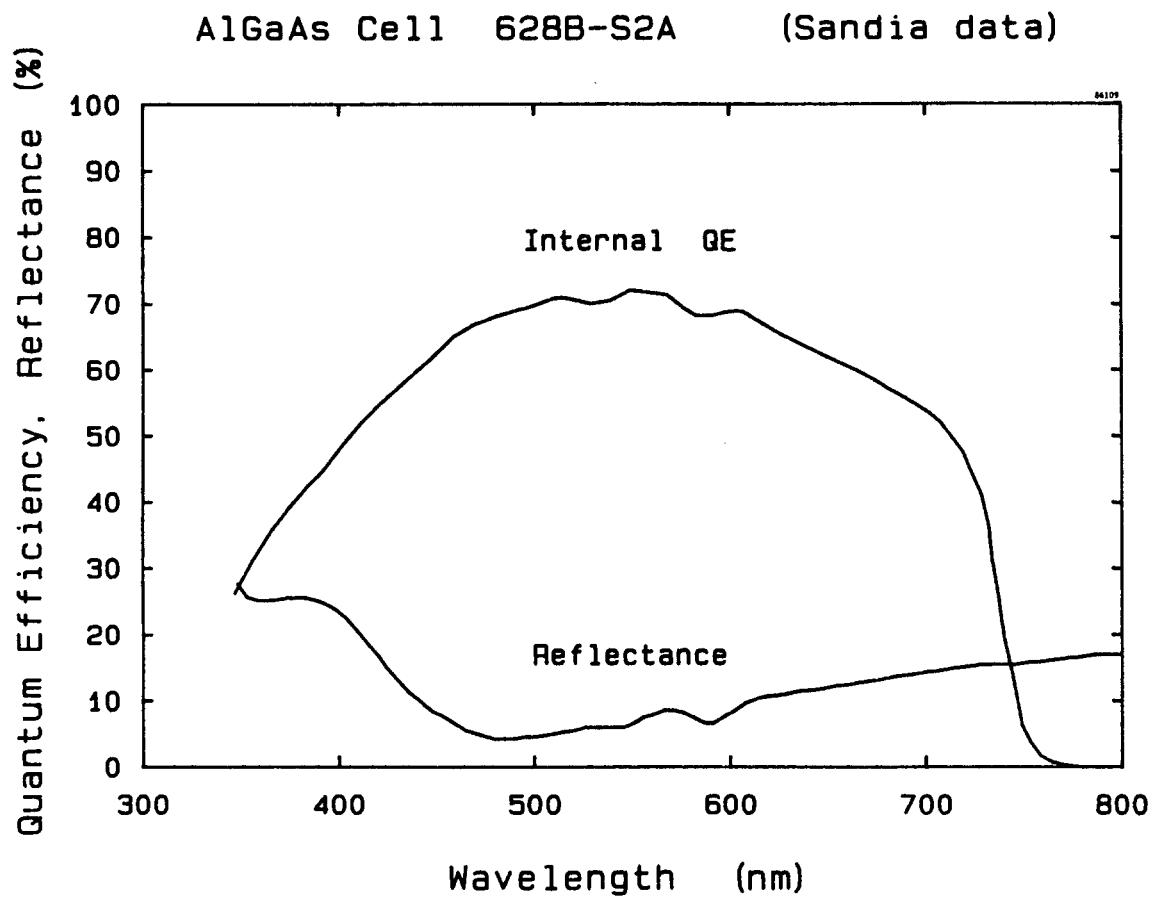


FIGURE 34. INTERNAL QUANTUM EFFICIENCY AND TOTAL REFLECTANCE MEASURED BY SANDIA FOR CELL 628B-S2A.

Somewhat higher concentrator cell efficiencies were achieved later in the program, but these cells were not measured at high concentrations by Sandia. The improvement was mostly in reduced grid line shadow and higher short circuit current. Wafers from the same growth run as cell 628B-S2A were used, so that material quality was the same. The performance of the two batches of cells is compared in Table 7. Subtracting about one percentage point from Spire's measurements to correct for short circuit current calibration, cell 628A-S1B has an efficiency of 13.8% at 15 suns. Assuming the same series resistance as cell 628B-S2A (measured contact resistances were the same) we can project a peak efficiency of about 14.6%.

Since these cells were processed, considerable improvement has been achieved both in grid line technology and in AlGaAs material growth. Recent AlGaAs cells processed under SERI funding have demonstrated one-sun efficiencies of 15.9% (SERI measurement) for a 1.70 eV bandgap. The improvement was mostly in short circuit current, as suggested by the above analysis. Based on these results very high efficiencies, in the 18% range, can be projected for AlGaAs concentrator cells.

TABLE 7. COMPARISON OF AlGaAs CONCENTRATOR CELLS 628B-S2A AND 628A-S1B (Spire measurements, not corrected for spectral mismatch).

Cell	Suns	V_{oc} (V)	J_{sc} (mA/cm ²)	FF (%)	Eff (%)
628B-S2A	1	1.145	12.93	84.2	12.47
628B-S2A	15.34	1.232	198.3	86.1	13.71
628A-S1B	1	1.153	13.72	78.0	12.24
628A-S1B	14.88	1.245	204.2	87.1	14.81

4.4 AlGaAs CELLS ON Ge SUBSTRATES

The highest efficiency AlGaAs concentrator cell grown on a Ge substrate was number 822C-S1C, with an efficiency of 12.1% at 16 suns. Its I-V curve is shown in Figure 35. The efficiency is lower than measured for our best AlGaAs cells on GaAs substrates. V_{oc} is lower than expected for a 1.65 eV cell, particularly on a Ge substrate. The fill factor is also lower than expected. This is not simply the effect of the Ge substrate, as a high series resistance was indicated by the log I vs. V characteristics of the cell. Some indication of nonohmic contacts was observed in the illuminated I-V

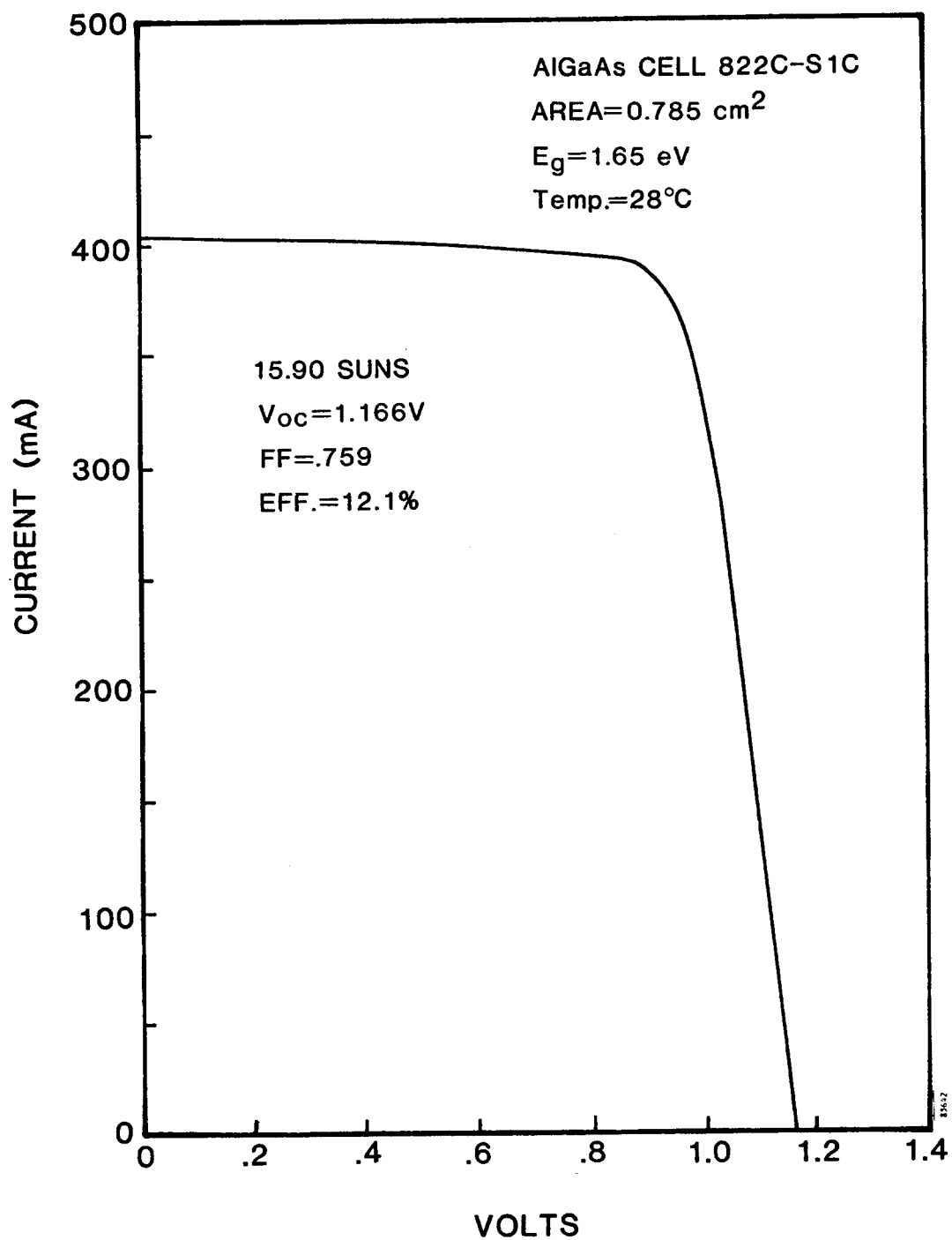


FIGURE 35. I-V CURVE AT 16 SUNS FOR AlGaAs-ON-Ge CONCENTRATOR CELL 822C-S1C.

characteristics on a curve tracer; a slight inflection point existed near the open-circuit point. The one-sun J_{sc} was 13.0 mA/cm^2 , somewhat lower than observed on our best AlGaAs cells grown on GaAs substrates. The external quantum efficiency shown in Figure 36 suggests reasons for a low J_{sc} . The blue response of the cell is low, the result of a relatively thick AlGaAs window layer in this run (1500 \AA). The peak quantum efficiency is also low. Part of this is ascribed to grid shadow, which was measured as 17%. Reflection loss should be only a few percent at the peak of the quantum efficiency curve. The remainder of the missing quantum efficiency must be due to incomplete collection of carriers generated in the cell.

This particular MOCVD run was noted as producing cells with low and variable short circuit currents. For example, Figure 36 also shows the quantum efficiency of another cell on the same wafer with a much different response (this cell is discussed in Section 4.6). There was a definite pattern to the J_{sc} variation on the wafer, with lower values closest to the top of the reactor bell jar. We suspect that a small leak in the reactor was responsible for the variation. Unfortunately near the end of the program when we were developing the AlGaAs on Ge cells the low J_{sc} problem was at its worst (see Figure 10). Our high efficiency AlGaAs cells on GaAs substrates were all grown earlier in the program. It is therefore difficult to separate the effects of the Ge substrate from the general AlGaAs growth problem. To investigate this we have compared the short circuit currents of cells grown in the same run on Ge and GaAs substrates. The results are summarized in Table 8. There does appear to be a consistent pattern of lower J_{sc} when Ge substrates are used. However, the number of cells is limited. More work is required in the future to first verify that a problem exists with Ge substrates, and then to identify and solve it.

TABLE 8. COMPARISON OF AlGaAs SOLAR CELL J_{sc} FOR Ge and GaAs SUBSTRATES. All J_{sc} values have been normalized to 5% grid shadow loss.

Run	Best J_{sc}		Mean J_{sc}		# of cells	
	on Ge	on GaAs	on Ge	on GaAs	on Ge	on GaAs
589	15.7	16.7	14.1	16.5	3	2
592	16.0	16.5	12.7	16.5	5	2
710	10.2	14.4	7.0	8.6	12	9
716	7.9	12.5	4.7	10.1	18	10

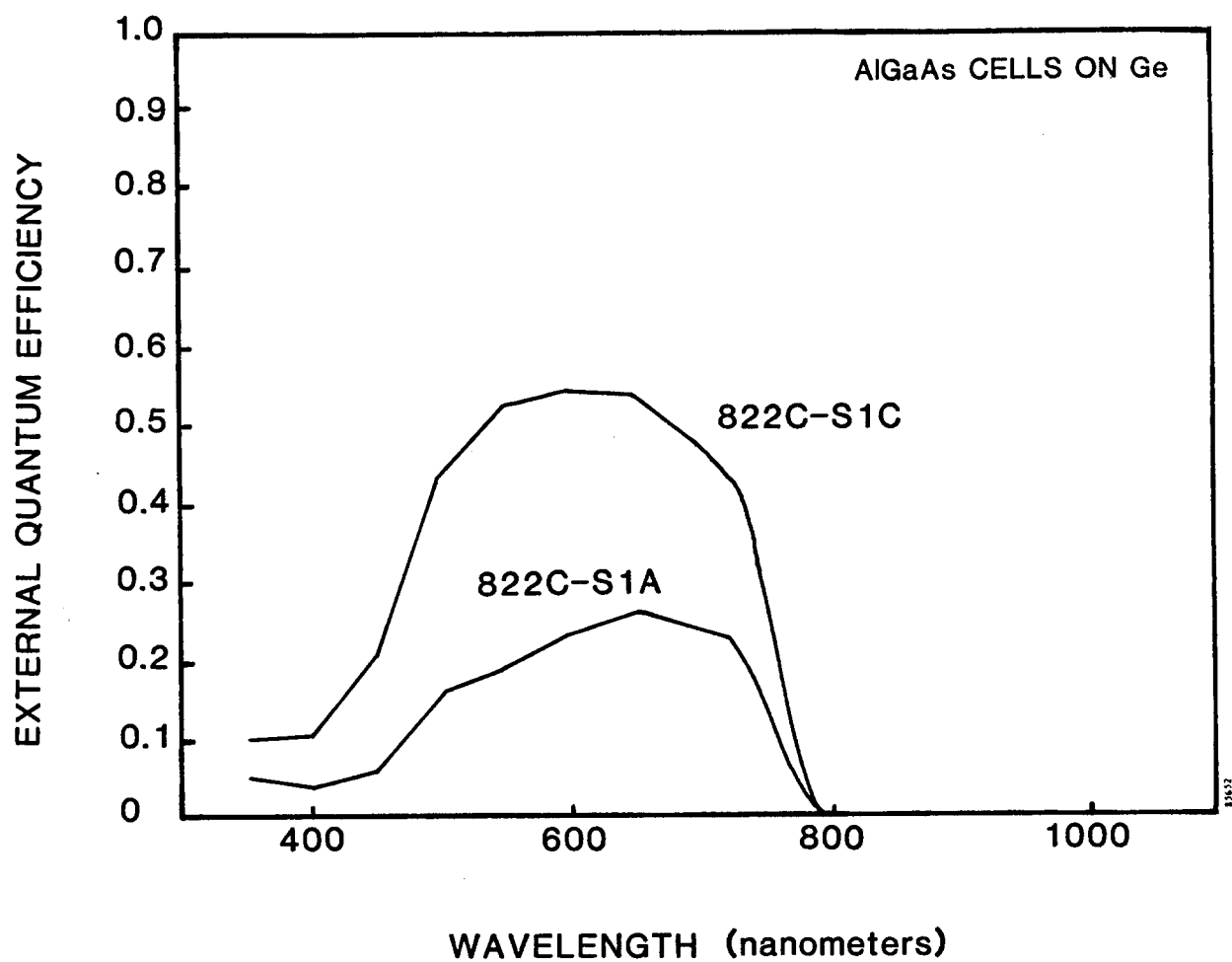


FIGURE 36. EXTERNAL QUANTUM EFFICIENCY CURVES FOR TWO AlGaAs CELLS GROWN ON THE SAME Ge SUBSTRATE.

4.5 THIN GaAs CELLS

Using the procedures described in Sections 3.3 and 3.4 the Ge substrate was removed from a GaAs cell with a one-sun grid pattern. A back contact grid was applied to the cell but no back antireflection coating was used. The I-V characteristics of the cell before and after removal of its Ge substrate are shown in Figure 37. Initially the cell exhibited a very low fill factor and very high open circuit voltage. With the parasitic Ge p-n junction removed, the fill factor and open circuit voltage returned to more normal values for a GaAs cell. The efficiency of the cell actually improved after substrate removal. A comparison of the log I-V curves in Figure 38 before and after thinning shows no increase in leakage current, as might be expected if the cell were damaged by the substrate removal process. This cell demonstrates the feasibility of the thin cell approach.

To see how the thin cell would act as a top cell in a mechanical stack, the transmission spectrum through the 5 micron cell has been measured. The data measured with a Perkin-Elmer spectrophotometer are shown in Figure 39. Interference fringes are particularly noticeable because the cell thickness is comparable to the wavelength of light. The transmission has a sharp turn-on at 870 nm and a below-bandgap transmittance of about 50%. The 50% transmittance can be adequately modeled as a combination of double grid shadow (the front and back grids were not aligned) and reflection off the front and back surfaces of the cell. A calculated transmission curve taking into account all of the optical layers is shown in Figure 40. To match the amplitude of the oscillations it was necessary to assume a bandwidth of 22 nm for the spectrophotometer. Without some form of averaging, the calculated amplitude of the oscillations was much larger than measured experimentally. Another way to account for this is to assume some nonuniformity in thickness across the cell. A disagreement between calculated and measured curves is evident near the absorption edge of GaAs. This could be because the spectrophotometer is out of calibration by a few nm, or could be caused by different absorption coefficients in the doped solar cell layers than were assumed in the model (undoped GaAs properties were used). The band edge absorption in GaAs is known to depend on doping.⁽¹⁷⁾

By aligning the grids and applying antireflection coatings to the back and front of the cell the transmission can be markedly increased. Figure 41 shows the transmission calculated for a thin AlGaAs cell with antireflection coatings on both sides. The

THINNING	V _{oc} (mV)	J _{sc} (mA/cm ²)	FF (%)	Efficiency (%)
BEFORE	1122	21.9	57.5	14.2
AFTER	958	21.1	75.4	15.2

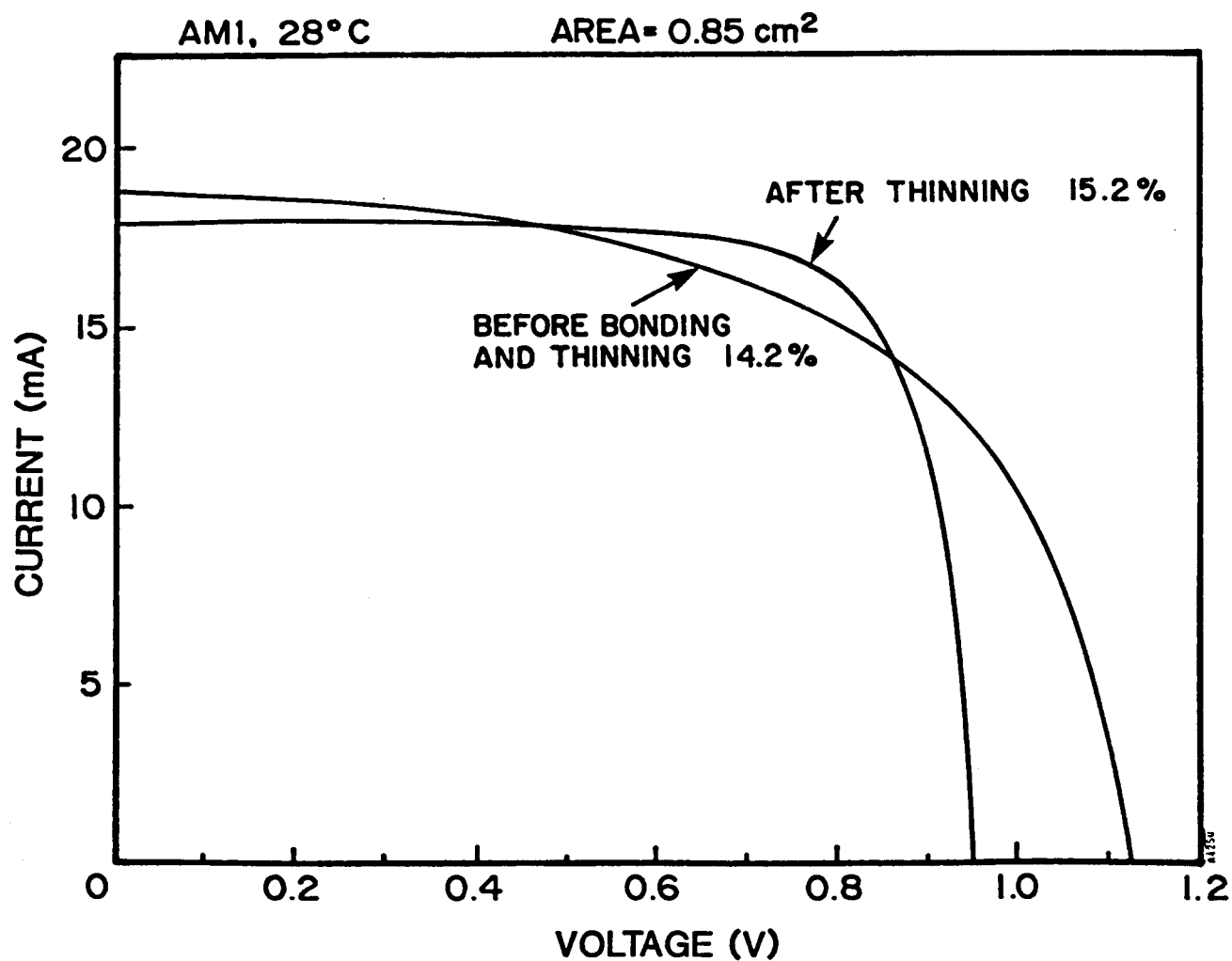


FIGURE 37. I-V CHARACTERISTICS OF GaAs CELL GROWN ON A Ge SUBSTRATE, BEFORE AND AFTER SUBSTRATE REMOVAL.

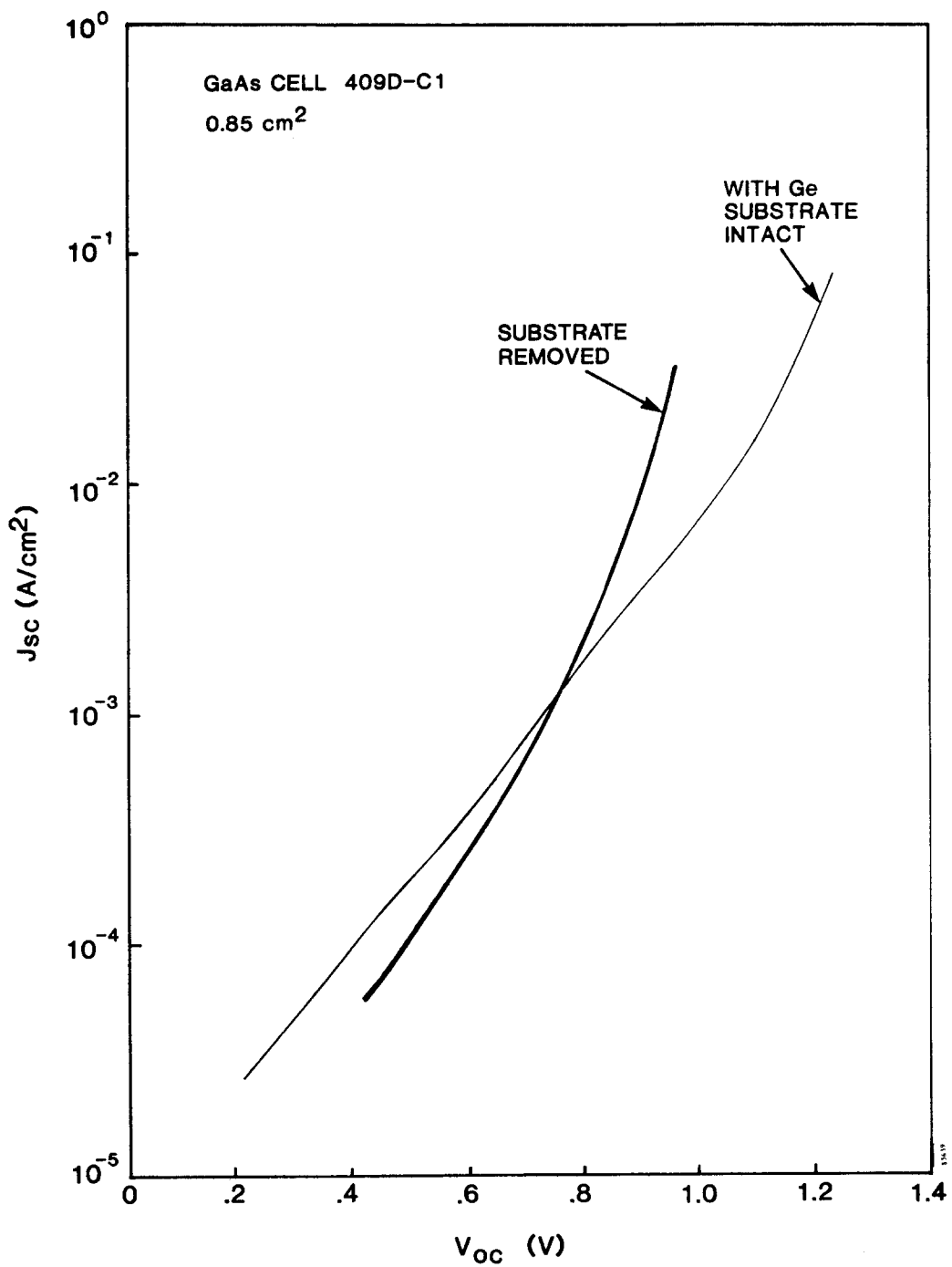


FIGURE 38. LOG I-V CHARACTERISTICS OF THE CELL IN FIGURE 37.

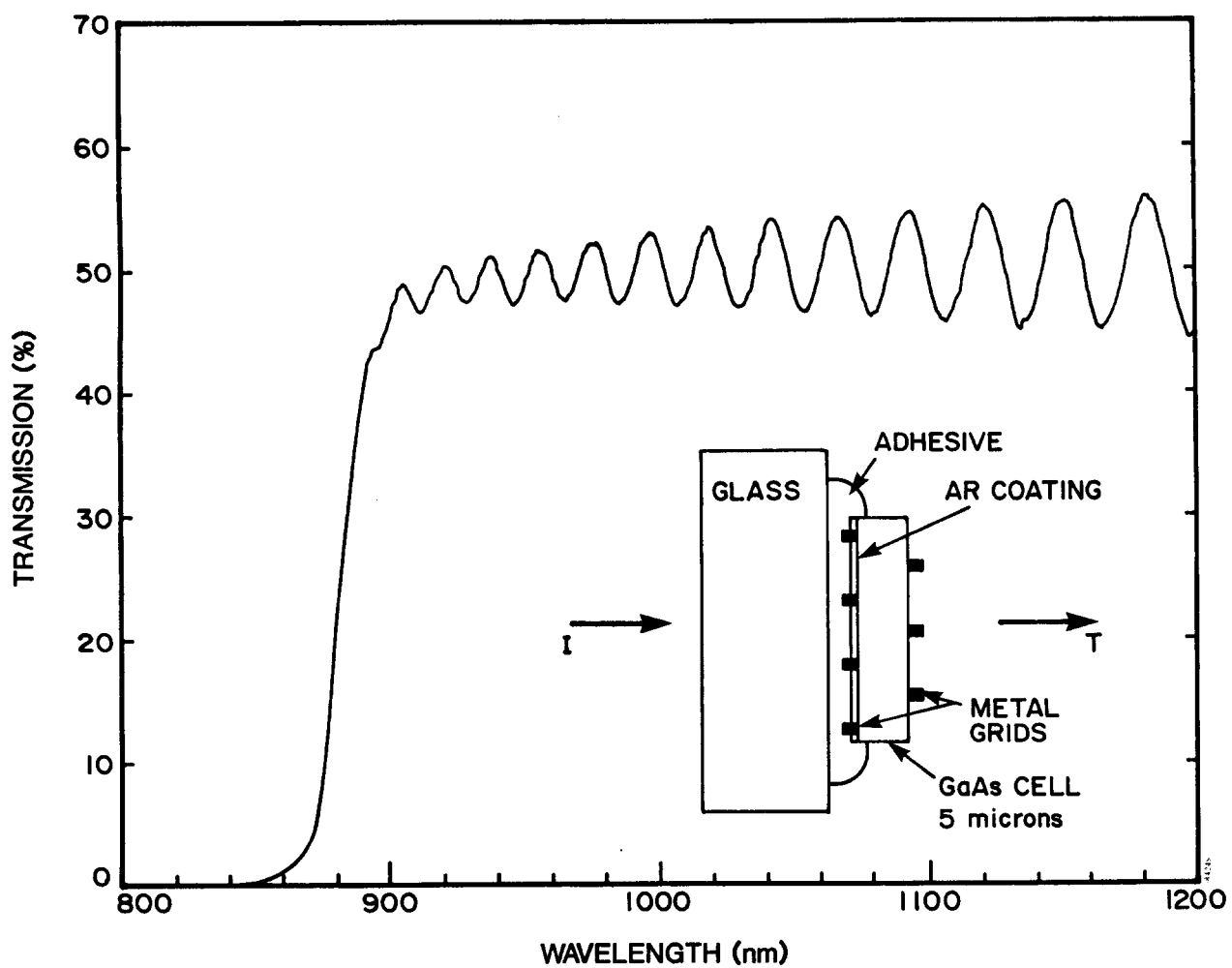


FIGURE 39. MEASURED TRANSMISSION SPECTRUM THROUGH A 5-MICRON GaAs CELL ORIGINALLY GROWN ON A Ge WAFER.

409D-C1 Thin GaAs Cell

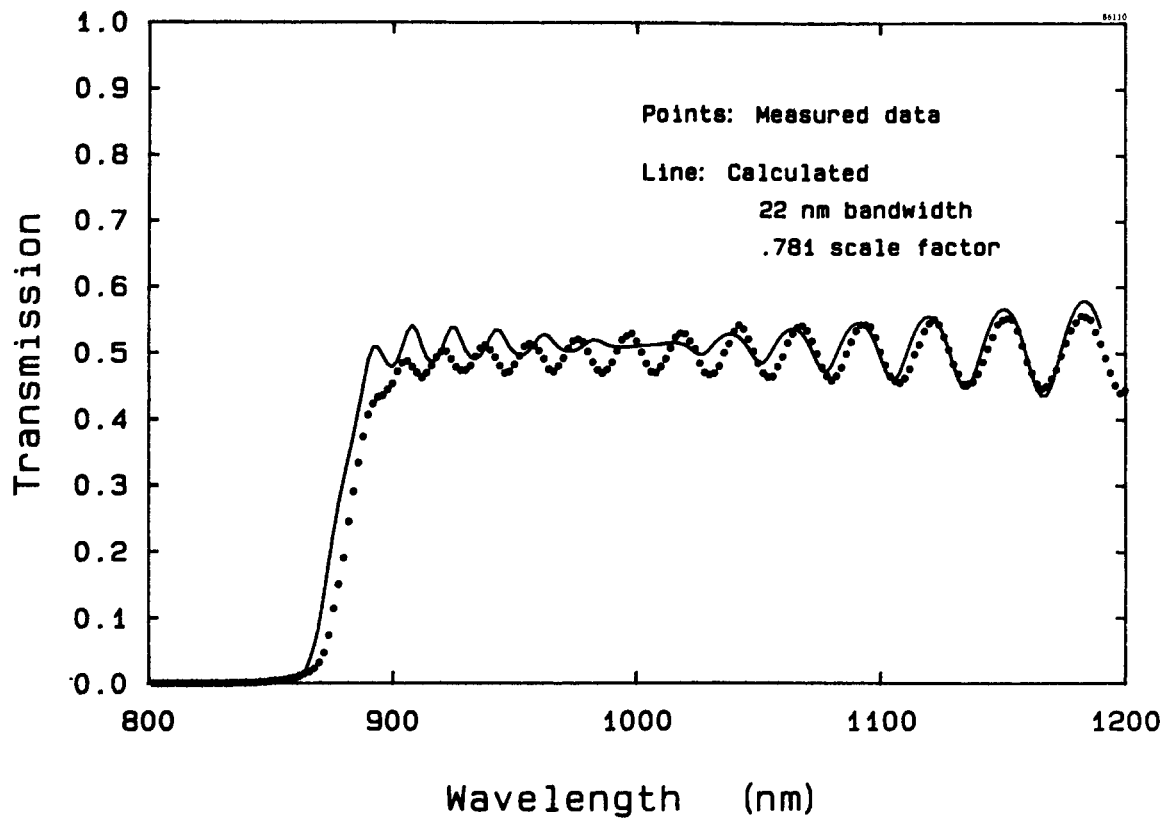


FIGURE 40. TRANSMISSION SPECTRUM CALCULATED FOR THE CELL OF FIGURE 39.

calculation does not include grid shadow or reflection from the front of the glass cover. The average transmission is about 94% in the wavelength range usable for a silicon cell. Most of the lost light is reflected from the front surface of the cell by an antireflection coating tuned for the AlGaAs cell. Broadband multilayer antireflection coatings could probably reduce the reflection loss considerably. Assuming an 8% grid shadow loss for aligned grids and a 2% reflection loss from a MgF_2 - coated glass cover, an average transmission of 85% is calculated for the structure in Figure 41.

Subsequent to the measurements described above, a progressive delamination of the cell from its cover glass was observed. This behavior had not been seen on previous samples and is not understood. Although process optimization work obviously remains to be done on the thin cells, feasibility has been established.

4.6 THIN AlGaAs CELLS

Two AlGaAs concentrator cells grown on Ge substrates, 822C-S1A and 822C-S1C, were chosen for substrate removal and backside processing. The process was as described in Sections 3.3 and 3.4, including concentrator grid patterns and antireflection coatings on both sides of the 5 micron cells. These cells demonstrated the feasibility of the complete thin AlGaAs cell process.

Figure 42 shows photographs of completed cell 822C-S1A. The cover glass supporting the cell is attached to two lucite support legs. A platform made from a plastic ruler was constructed around the cover glass so that the ribbon leads could be brought around to the top surface of the structure for testing. Figure (a) shows the front of the thin cell, viewed through the cover glass. Figure (b) shows the back of the cell. The lucite legs are out of focus in the photograph. The attachment scheme of the ribbon leads is visible, three to the front of the cell in the corners, and four to the back of the cell. The leads wrap around the cover slide to the front.

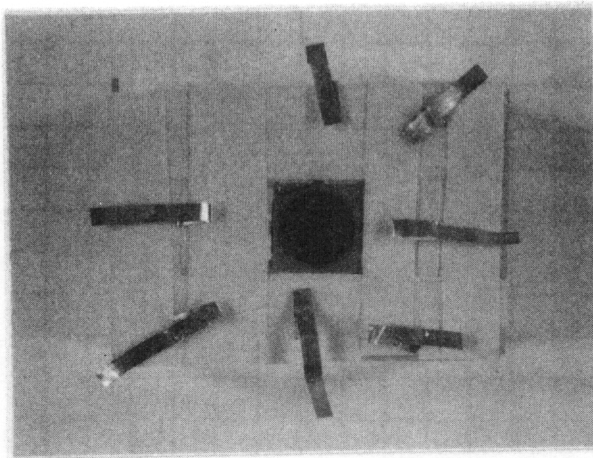
Testing revealed that cell 822C-S1A showed only a small change in efficiency through the substrate removal process. Table 9 compares the one sun simulator results with and without the Ge substrate. One sun I-V curves are shown in Figure 43, and log I-V curves are compared in Figure 44. We saw no increase in junction leakage current after

substrate removal, indicating that the thinning process is nondestructive to the cell. The drop in open circuit voltage after thinning is attributed to removal of the extra p-n junction in the Ge substrate. The fact that the fill factor did not increase after removal of the substrate (as was seen earlier for a thin GaAs cell) points to series resistance as the cause of a low fill factor.

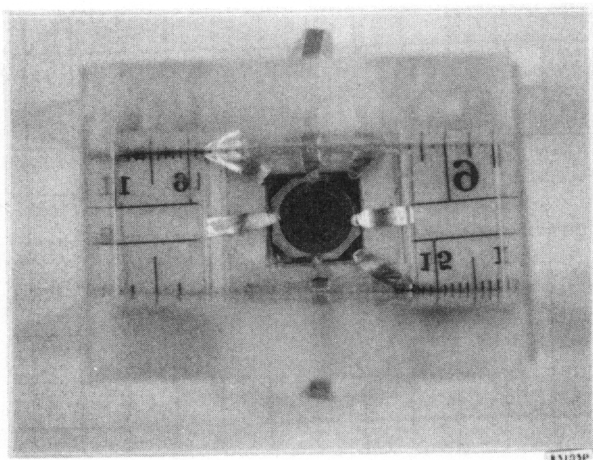
TABLE 9. ONE SUN TEST RESULTS FOR 1.65 eV AlGaAs
CONCENTRATOR CELL 822C-S1A. Test conditions were
AM1.5, 100 mW/cm², 28 C.

Ge Substrate	V _{oc} (mV)	J _{sc} (mA/cm ²)	FF (%)	Efficiency (%)
Intact	1048	6.34	70.3	4.7
Removed	960	6.48	68.3	4.3

While cell 822C-S1A demonstrated the feasibility of the complete thin cell process, its efficiency was much lower than desired. Companion cell 822C-S1A had a much higher starting efficiency, over 12% at 15 suns (Section 4.4). Unfortunately it was damaged after thinning while trying to remove photoresist residue with a cotton swab. The achievement of high efficiency in a thin AlGaAs cell must wait for future work.



(a)



(b)

FIGURE 42. PHOTOGRAPHS OF THE COMPLETED THIN AlGaAs CONCENTRATOR CELL. (a) Front of the cell, seen through the cover glass. (b) Back of the cell, with silver ribbons attached.

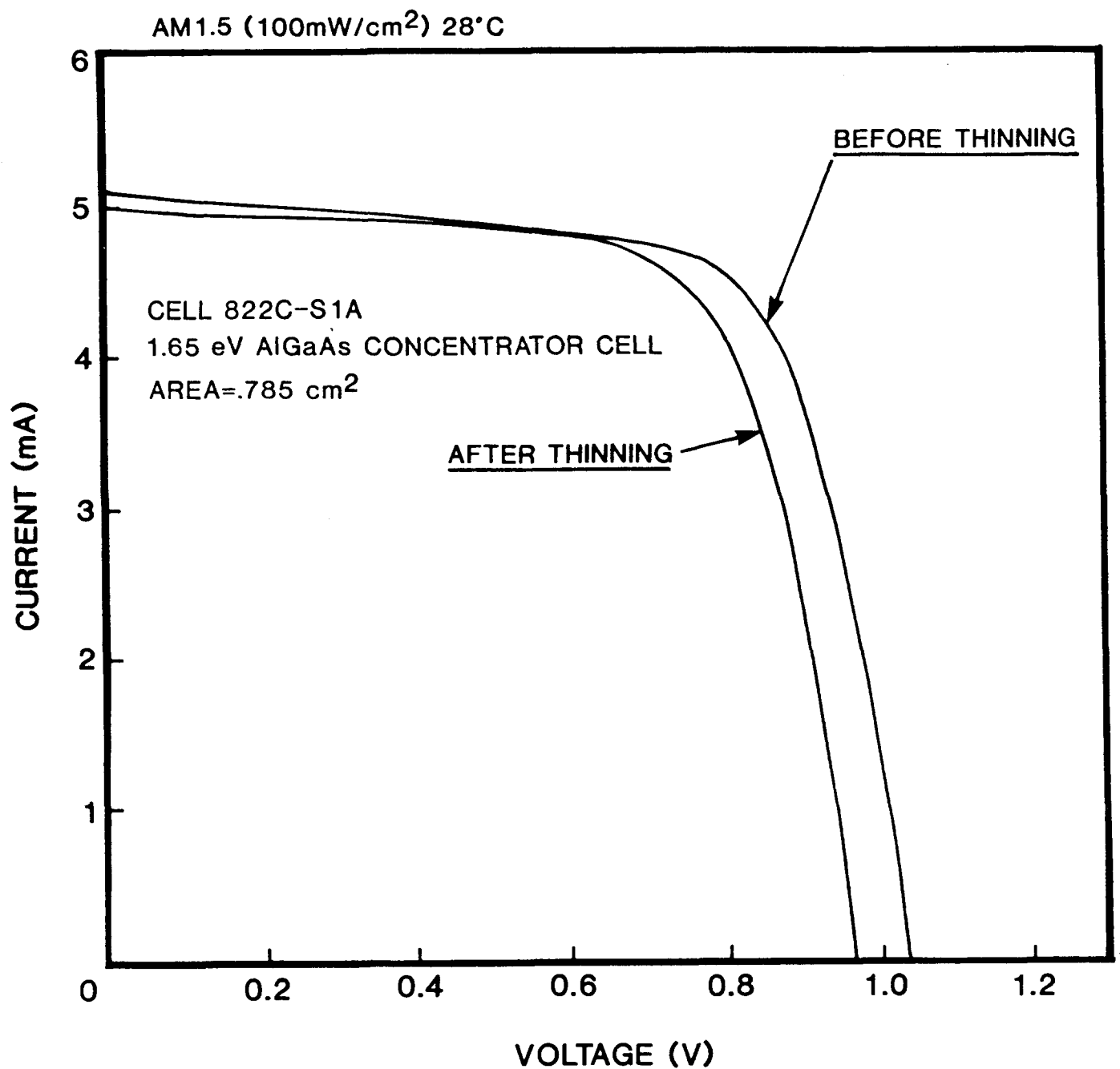


FIGURE 43. ONE-SUN I-V CURVES BEFORE AND AFTER REMOVAL OF THE Ge SUBSTRATE. This thin AlGaAs concentrator cell was transparent to below-gap photons and demonstrated the feasibility of our approach.

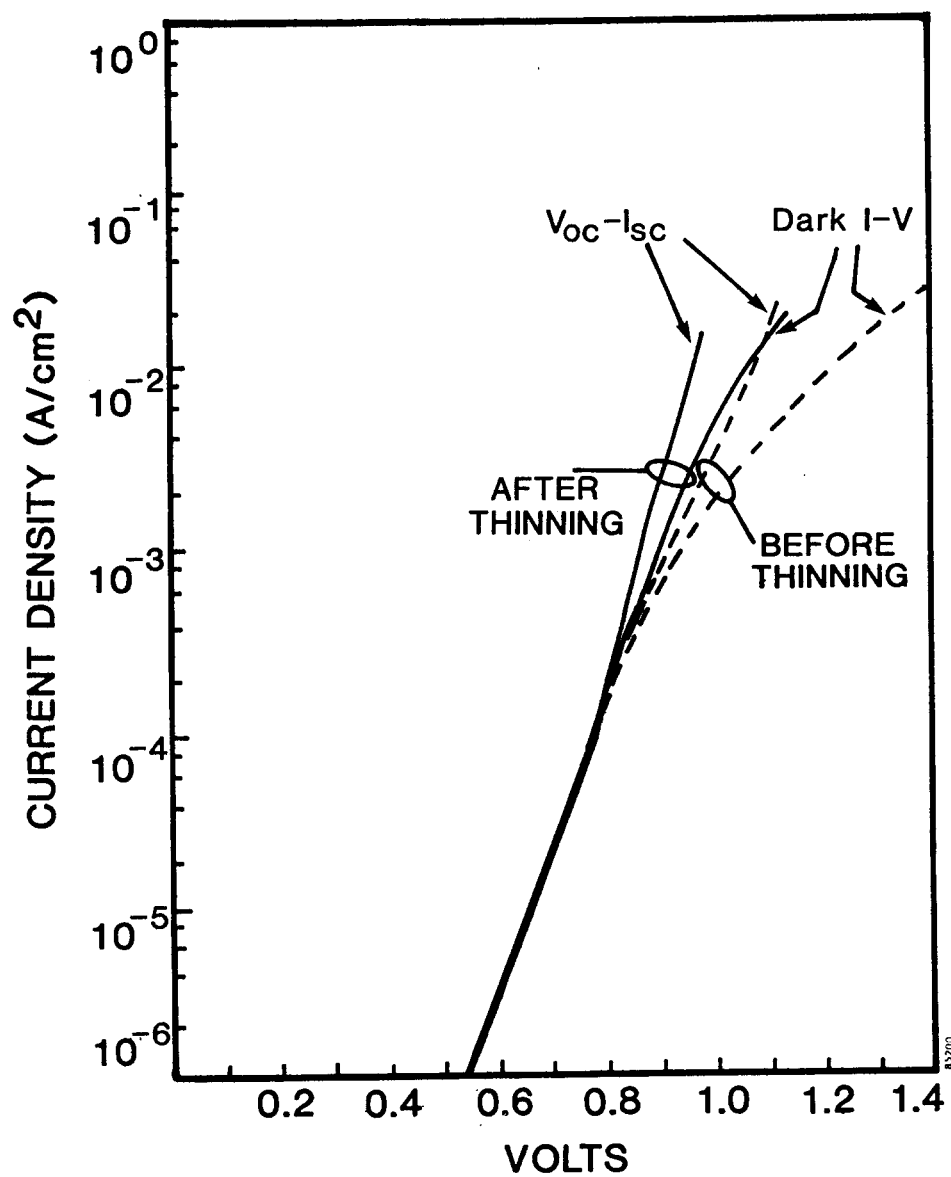


FIGURE 44. LOG I-V CHARACTERISTICS OF CELL 822C-S1A FROM FIGURE 43.

SECTION 5

CONCLUSIONS

The major conclusions of this work are as follows:

- 1) Removable Ge growth substrates are a viable approach for producing ultrathin solar cells of GaAs and AlGaAs.
- 2) Doping of the active cell layers by Ge during growth can be effectively controlled by capping the backs of the Ge wafers with epitaxial GaAs.
- 3) Diffusion of Ga and As into the substrate produces a Ge p-n junction in series with the active solar cell. While this prevents accurate characterization of the GaAs or AlGaAs solar cell junction with the substrate intact, removal of the substrate also removes the problem.
- 4) Selective etching with hydrogen peroxide is an effective way of removing the Ge substrate without harming an ultrathin 5 micron solar cell.
- 5) Thin solar cells of AlGaAs and GaAs have been produced with little or no degradation of starting efficiency. No unexpected losses of below-bandgap photons have been encountered.

SECTION 6

PROBLEM AREAS AND AREAS FOR FUTURE WORK

The following problem areas were encountered during the course of the program and not entirely resolved:

- 1) Reproducible surface preparation of Ge substrates prior to MOCVD growth. This is mostly a problem of the wafer supplier. In future work it is desirable to do a final wafer polish in-house so that this critical step can be better controlled.
- 2) Reproducible achievement of high diffusion lengths in AlGaAs solar cell material. This problem was discussed in Section 2.4.
- 3) We have some evidence of lower short-circuit currents in AlGaAs solar cells grown on Ge than on GaAs substrates. In future work this should be investigated in more detail to see if there is a fundamental problem.
- 4) Excessive shadow loss in concentrator cells. This was a result of immature grid processing technology. Great improvement was made during the program and with additional work the required narrow lines can be produced. Two areas requiring further development are undercutting of the silicon dioxide plating mask and control of mushrooming during plating.
- 5) Short-circuiting and excessive leakage for concentrator cells. We observed a high occurrence of short-circuited concentrator cells, whereas one-sun type cells on the same wafer did not have this problem. The major difference in the two cells is the large area of the concentrator cell covered by metallization under the bus bar. Since the problem was observed for cells even before any heat treatments were applied to the metallization, we hypothesize that defects in the as-grown material were responsible. Two ways to overcome the problem are to lower the number of defects in the as-grown material and to change the design to be tolerant of defects. The latter approach would involve, for example, placing an insulating layer between the cell and the bus bar.

- 6) Bonding of the cell to a glass superstrate. The silicone adhesive used in this work has a number of drawbacks, including a very large thermal expansion mismatch to AlGaAs and a maximum processing temperature lower than desired for producing ohmic back contacts. Ideally the adhesive and glass would be well matched to the thermal expansion of AlGaAs, allowing a rigid bond to be formed between the cell and glass. The present elastomer layer makes the thin cell very susceptible to breakage. In addition the thin cell on GaAs had an unexpected delamination from the cover glass that should be investigated.
- 7) Making electrical contact to the thin cell. There are two areas here that could benefit from innovative ideas: making low temperature ohmic contacts to the back of the cell, and connecting from the ohmic contact layers on both sides of the cell to the outside world.
- 8) Packaging of the thin cells. Thin cells are susceptible to mechanical damage, but could be protected with a suitable package design. The package should also address low resistance interconnects to both sides of the cell and thermal transfer to a heat sink.

SECTION 7

ACKNOWLEDGMENTS

The author wishes to acknowledge the contributions of his many colleagues at Spire Corporation during the course of the program. Dr. Robert Wolfson was the program manager. Dr. Mark Spitzer was instrumental in formulating the approach for the program and in obtaining funding. The MOCVD growth team was directed by Stan Vernon, with growth runs carried out by Victor Haven and John Enterkin. Concentrator cell grid design was performed by Chris Keavney. Susan Davis was responsible for concentrator cell process development. Clara Bajgar developed the process for producing thin solar cells. Harry Drake and the staff of the solar cell processing laboratory provided assistance in solar cell fabrication. Mike Nowlan provided technical expertise in cell-to-glass bonding and in interconnect techniques. Solar cell testing was carried out by Joe McDonough, under the supervision of Mike Sanfacon. Mr. Sanfacon also developed all of the cell diagnostic measurements.

At Sandia National Laboratories James Gee provided technical guidance and provided us with extensive cell test data. Dave King collaborated on the design of the concentrator cell grid pattern and verified our final design.

A number of material characterization techniques were applied to our samples at outside laboratories. Dr. James Norberg at Charles Evans and Associates performed many SIMS analyses of solar cell structures. Spreading resistance measurements verifying the formation of a Ge p-n junction were carried out at Solecon Laboratories by Paul Picard. We are grateful to Dr. Dave Dickey at Solecon for pointing out the utility of spreading resistance measurements in Ge. TEM measurements were performed by Dr. Harry Kawayoshi at ARACOR.

APPENDIX A CONCENTRATOR CELL GRID DESIGN

Making the assumption that a set of K lines radiating in from the edge, equally spread and equally sized, is the best design, we can calculate the loss due to shadow as: (see list of symbols below)

$$dP = WJVKdr \text{ (WKdr is the area shadowed, JV is the power per unit area)}$$

The loss due to line resistance is:

$$dP = \frac{\rho}{HWK} I^2 dr$$

where I is the total current generated in a circle of radius r.

The loss due to sheet resistance is:

$$dP = \frac{J^2 R D^3 K}{I^2} dr$$

substituting $D = \frac{2\pi r}{K}$, $I = J\pi r^2$, $H = AW$, we have

$$dP = \left(WJVK + \frac{\rho J^2 \pi^2 r^4}{AW^2 K} + \frac{2}{3} \frac{\pi^3 J^2 R r^3}{K^2} \right) dr$$

In the most general case, K and W are both functions of r. Optimizing W gives:

$$\frac{dP}{dWdr} = JVK - \frac{2\rho J^2 \pi^2 r^4}{AW^3 K} = 0$$

$$W = \left(\frac{2\rho J^2 \pi^2 r^4}{V K^2 A} \right)^{1/3}$$

Substituting this back in gives:

$$\frac{dP}{dr} = 3 \left(\frac{\rho J^4 \pi^2 r^4 K V^2}{4A} \right)^{1/3} + \frac{2}{3} \frac{\pi^3 J^2 R r^3}{K^2}$$

Optimizing K gives:

$$\frac{dP^2}{dr dK} = \left(\frac{\rho J^4 \pi^2 r^4 V^2}{4AK^2} \right)^{1/3} - \frac{4}{3} \frac{\pi^3 J^2 R r^3}{K^3} = 0$$

$$K = \left(\frac{256}{27} \frac{\pi^7 J^2 R^3 r^5 A}{\rho V^2} \right)^{1/7}$$

$$W = \left(\frac{9}{8} \frac{J r^6 \rho^3}{R^2 A^3 V} \right)^{1/7}$$

$$\frac{dP}{dr} = \frac{7}{2} \left(\frac{\pi^2 J^{10} R r^{11} \rho^2 V^4}{12A^2} \right)^{1/7}$$

integrating with respect to r gives:

$$P = \frac{49\pi}{36} \left(\frac{J^{10} R r^{18} \rho^2 V^4}{12A^2} \right)^{1/7}$$

expressed as a fraction of the potential power, we have:

$$\frac{P}{\pi r^2 J V} = \frac{49}{36} \left(\frac{J^3 R r^4 \rho^2}{12A^2 V^3} \right)^{1/7}$$

for the parameters we have assumed, this works out to 14.9%. This P is exactly 4/7 shadow loss, 2/7 line resistance loss, and 1/7 sheet resistance loss.

In practice however, H (and therefore W) must remain constant over the entire cell, and each change in the value of K is accomplished by a ring which allows the current to be redistributed and also increases the shadow loss. If K is constant from r_1 to r_2 , the loss in that region is:

$$P = WJV K(r_1 - r_2) + \frac{\rho}{Aw^2} \frac{J^2 \pi^2}{5K} (r_1^5 - r_2^5) + \frac{\pi^3 J^2 R}{6K^2} (r_1^4 - r_2^4)$$

and the extra shadow loss due to a ring at radius r is:

$$P = 2\pi WJV.$$

The optimum K for a given r and W can be found from:

$$WJV - \frac{\rho}{Aw^2} \frac{J^2 \pi^2 r^4}{K^2} - \frac{4}{3} \frac{\pi^3 J^2 R r^3}{K^3} = 0$$

The optimum r for changing between two values of K can be found from:

$$WJV (K_1 - K_2) + \frac{\rho J^2 \pi^2 r^4}{Aw^2} \left(\frac{1}{K_1} - \frac{1}{K_2} \right) + \frac{2\pi^3 J^2 R r^3}{3} \left(\frac{1}{K_1^2} - \frac{1}{K_2^2} \right) + 2\pi WJV = 0$$

where K_1 is the number of lines in the inner ring, and K_2 in the outer ring. Since $K_1 - K_2$ is usually much greater than 2π , the last term can usually be neglected.

What these equations do not give us is the optimal W , which must be found by trial and error, and the best change in the value of K ; that is, how many rings there should be and what the values of K should be. By trial and error it was found that if K increases by a factor of 1.7 at each ring, the tradeoff between reducing the number of rings and keeping the value of K close to the optimum is about even, so this is the optimal jump in K .

In designing the grid, W and each value of K were varied, calculating the r 's and the losses each time, until a minimum for P was found (approximately 16.4%). This design has, approximately, the same 1:2:4 ratio between sheet, line and shadow losses which the theoretical minimum has.

Refinements and Limitations

1. Uncertainty exists in many of the parameters, particularly ρ and A . Fortunately, ρ and A have relatively little effect on the optimum K ($K \propto (A/\rho)^{1/7}$). They have a greater effect on the optimum plating height H , but this can be adjusted empirically after the mask is made.
2. This is a first-order approximation which assumes that the power losses combine linearly. This is true only if the losses themselves are small compared with the power output of the cell. For example, in the equation for

line resistance loss, the current should be corrected for shadow loss, and in the equation for shadow loss, the voltage should be corrected for series resistance. The first of these effects affects the equations in much the same way as a change in ρ or A , and, in fact, it is expected to largely cancel the error introduced by the fact that the assumed value of ρ is probably too low. Estimating the effect of the second yields a total power loss of 15.8%, instead of 16.4%. (Taking both into account and assuming that the value for ρ is correct yields 15.0%.)

3. Some cell designs have used branches to change the value of K , instead of complete rings. This results in a slightly reduced shadow loss, but it does not justify the loss of redundancy coupled with the extra difficulty of fabricating the mask.
4. The assumption has been made that current will always flow directly to the nearest grid line. Particularly near the center, this may not be true; the current will follow the path of least resistance. Thus, the equations for series resistance are conservative.

Symbols:

J = active area current density at maximum power point = 12.08 A/cm^2

V = maximum power point voltage = 1.056 V

W = width of lines (cm)

K = number of lines around circle

r = distance from center of cell (cm)

ρ = resistivity of metal lines = $2.6 \times 10^{-6} \Omega\text{cm}$

H = plating height (cm)

I = cell current as a function of r

R = sheet resistance = $400 \Omega/\square$

D = line spacing (cm)

A = aspect ratio = $H/W = 0.333$

P = power loss (watts)

Spire Concentrator Cell Grid Design

The grid consists of 8 tiers of radial lines, the outermost 4 tiers being connected by concentric rings. The following table gives the diameter of each ring or tier and the line spacing in each tier.

Tier No.	Inner radius (cm)	Outer radius (cm)	Number of lines	Inner spacing (μm)	Outer spacing (μm)	Shadow loss (W)	Line loss (W)	Sheet loss (W)	Total loss (W)	Total loss (%)
1	0.3725	0.5000	400	58.5	78.5	0.4554	0.0815	0.2760	0.8129	8.11
2	0.2569	0.3725	240	67.3	97.5	0.2477	0.0780	0.1156	0.4414	4.41
3	0.1588	0.2569	150	66.5	107.6	0.1314	0.0499	0.0311	0.2124	2.12
4	0.0846	0.1588	80	66.4	124.7	0.0530	0.0276	0.0055	0.0861	0.86
5	0.0427	0.0846	40	67.1	132.9	0.0150	0.0090	0.0005	0.0245	0.24
6	0.0214	0.0427	20	67.2	134.1	0.0038	0.0023	0	0.0062	0.06
7	0.0107	0.0214	10	67.2	134.5	0.0010	0.0006	0	0.0016	0.02
8	0	0.0107	5	0	134.5	0.0005	0.0002	0	0.0006	0.01
Additional shadow loss from rings									1.5856	15.83
									0.52	0.52
									16.35%	16.35%

All lines are $7\text{ }\mu\text{m}$ wide and $2.3\text{ }\mu\text{m}$ high.

The following parameters were assumed:

Current at maximum power point = 12.08 A/cm^2 (active area)
Voltage at maximum power point = 1.056 V
Resistivity of metal = $2.6 \times 10^{-6}\text{ }\Omega\text{cm}$
Sheet resistance of cell = $400\text{ }\Omega/\square$

Results:

Total shadow loss = 9.6%
Line resistance loss = 4.3%
Sheet resistance loss = 2.5%
Resulting cell J_{max} = 10.9 A/cm^2
 V_{max} = 0.983 V
Efficiency = 21.4%

REFERENCES

1. See for example sessions 1-A and 3-A of Proc. of the 18th IEEE Photovoltaic Specialists Conf., 1985.
2. J. G. Werthen, 12th Photovoltaic Concentrator Project Integration Meeting, August 1984. Sandia Report SAND84-0556, p. 34.
3. R. J. Boettcher, P. G. Borden, and M. J. Ludowise, Proc. of 16th IEEE Photovoltaic Specialists Conf., 1982, p. 1470.
4. J. C. C. Fan, C. O. Bozler and B. J. Palm, Appl. Phys. Lett. 35, 875 (1979).
5. D. L. Miller and J. S. Harris, Jr., Appl. Phys. Lett. 37, 1104 (1980).
6. S. Zwerdling, K. L. Wang and Y. C. M. Yeh, J. Solar Energy Engineering 105, 237 (1983).
7. M. J. Ludowise, J. Appl. Phys. 58, R31 (1985).
8. For a review of the literature prior to 1972, see A. G. Milnes and D. L. Feucht, Heterojunctions and Metal-Semiconductor Junctions (Academic Press, New York, 1972).
9. G. O. Ladd, Jr. and D. L. Feucht, Metallurgical Trans. 1, 609 (1970).
10. H. Kasano and S. Hosoki, J. Electrochem. Soc. 122, 112 (1975).
11. S. M. Sze, Physics of Semiconductor Devices (Wiley, New York, 1969) p. 31.
12. F. A. Trumbore, Bell Syst. Tech. J. 39, 205 (1960).
13. K. Morizane, J. Crystal Growth 38, 249 (1977).
14. B-Y. Tsaur, J. C. C. Fan, G. W. Turner, F. M. Davis and R. P. Gale, Proc. of 16th IEEE Photovoltaic Specialists Conf., 1982, p. 1143.
15. M. Kato, et al., Proc. of 18th IEEE Photovoltaic Specialists Conf., 1985.
16. H. C. Hamaker, J. Appl. Phys. 58, 2344 (1985).
17. H. C. Casey, Jr., D. D. Sell and K. W. Wecht, J. Appl. Phys. 46, 250 (1975).
18. D. L. Kendall, Semiconductors and Semimetals Vol. 4, ed. R. K. Willardson and A. C. Beer (Academic Press, 1968) p. 163.

DISTRIBUTION LIST:

Aerospace Corporation
Attn: Ed Simburger
2350 El Segundo Blvd.
El Segundo, CA 90266

California Institute
of Technology
Attn: Marc A. Nicolet
Electrical Engineering Dept.
116-81
Pasadena, CA 91125

Applied Solar Energy Corp. (4)
Attn: John Tracy
Ken Ling
Kou-I Chang
Marshal Cohen
15251 E. Don Julian Road
City of Industry, CA 91746

U. S. Dept. of Energy
ALO
Attn: D. L. Krenz
P. O. Box 5400
Albuquerque, NM 87115

ARCO Power Systems
Attn: Floyd Blake
Suite 307
7061 S. University Blvd.
Littleton, CO 80122

U. S. Dept. of Energy
Attn: John Hanson
Nuclear & Geosciences Div.
P. O. Box 5400
Albuquerque, NM 87115

Arco Solar, Inc. (5)
Attn: Ray Kosanke
Charles Gay
Kim Mitchell
Henry Yoo
Library
9351 Deering Street
Chatsworth, CA 91313

U. S. Dept. of Energy (8)
Div. of PV Energy Technologies
Attn: R. Annan
A. Krantz
M. Prince
L. Herwig (5)
1000 Independence Ave. SW
Washington, DC 20585

Arizona State University
Attn: Charles Backus
College of Engineering
Tempe, AZ 85281

ENTECH (3)
Attn: Walter Hess
Mark O'Neill
A. J. McDanal
P. O. Box 612246
DFW Airport, TX 75261

Black & Veatch (2)
Attn: Sheldon L. Levy
Larry Stoddard
11401 Lamar
P. O. Box 8405
Overland Park, KS 66211

EPRI (2)
Attn: Frank Goodman
Ed DeMeo
P. O. Box 10412
Palo Alto, CA 94303

Brooklyn College
Attn: Prof. Fred Pollak
c/o Physics Dept.
Brooklyn, NY 11210

General Dynamics/Convair
Mail Zone 56-6760
P. O. Box 83537
San Diego, CA 92138

Hughes Research Labs (2)
Attn: S. Kamath
R. Loo
3011 Malibu Canyon Road
Malibu, CA 90265

3M (4)
Attn: Sanford Cobb
235-BC05
3M Center
St. Paul, MN 55144

Intersol Power Corporation (3)
Attn: John Sanders
Derek Cass
Juris Berzins
11901 West Cedar
Lakewood, CO 80228

Martin Marietta (2)
Attn: H. C. Wroton
D. Hughes
P. O. Box 179
Denver, CO 80201

L. W. James and Associates
Attn: L. James
1525 E. County Road 58
Fort Collins, CO 80524

McDonnell Douglas (2)
Attn: David Carey
Ken Stone
5301 Bolsa Avenue
Huntington Beach, CA 92647

Jet Propulsion Lab (3)
Attn: W. Callaghan
M. Leipold
Solar Data Center
MS 502/414
4800 Oak Grove Drive
Pasadena, CA 91109

Meridian Corporation
Attn: Bradley Macaleer
5113 Leesburg Pike, Suite 700
Falls Church, VA 22041

Kopin Corporation (2)
Attn: Dr. Ronald P. Gale
Dr. J.C.C. Fan
695 Myles Standish Blvd.
Taunton, MA 02780

Microwave Associates
Attn: Joel Goodrich
South Avenue MS-116
Burlington, MA 01803

Lampert Technologies Corp.
Attn: John Mackay
P. O. Box 17478
San Diego, CA 92117

MIT/Lincoln Lab
Attn: George Turner
Box 73
Lexington, MA 02173

M/A-COM PHI (2)
Attn: Sewang Yoon
Jeff Meyer
1742 Crenshaw Blvd.
Torrance, CA 90501

Motorola
Attn: Keith Kingston
GED
8201 E. McDowell
Scottsdale, AZ 85252

MRI-SOLERAS
Attn: Matt Imamura
425 Volker Blvd.
Kansas City, MO 64110

NASA, HQ
Attn: John Loria
Code RET-1
Washington, DC 20546

NASA/Lewis Research Center (2)
Attn: Manju Goradia
Henry Curtis
c/o Dr. David Brinker, M/S 302-1
21000 Brookpark Rd.
Cleveland, OH 44135

National Technical Systems (2)
Attn: Tomasz Jannson
David Pelka
12511 Beatrice St.
Los Angeles, CA 90066

North Carolina State University
Attn: M. Hashemi
P. O. Box 50384
Raleigh, NC 27650

Oak Ridge National Lab
Attn: Steve Kaplan, Y-12 9102-2
P. O. Box Y
Oak Ridge, TN 37830

Pacific Gas & Electric (2)
Attn: Steve Hester
Tom Hoff
3400 Crow Canyon Road
San Ramon, CA 94583

Purdue University (3)
Attn: Richard Schwartz
Mark Lundstrom
Jeff Gray
School of Electrical Engineering
West Lafayette, IN 47907

Research Triangle Institute (2)
Attn: Mike LaMorte
James Hutchby
Box 12194
Research Triangle Park, NC 27709

SERA Solar Corp. (3)
Attn: Larry Anderson
Lee Christel
James Gibbons
3151 Jay Street
Santa Clara, CA 95054

SERI (5)
Attn: Jack Stone
John Benner
R. Hein
Donna Hawkens
Cecile Leboeuf
1617 Cole Blvd.
Golden, CO 80401

SERI, Library (2)
1536 Cole Blvd., Bldg. #4
Golden, CO 80401

Solarex Corporation
Attn: Ramon Dominguez
201 Perry Parkway
Gaithersburg, MD 20877

Spectrolab (3)
Attn: Jan Smith
Ron Diamond
J. Minahan
12500 Gladstone Avenue
Sylmar, CA 91342

Spire (5)
Attn: S. Tobin
R. Little
M. Spitzer
M. Nowlan
S. Rechteris
Patriots Park
Bedford, MA 01730

Stanford University (2)
Attn: Ron Sinton
Richard Swanson
McCullough 206
Stanford, CA 943405

Star Light Energy
Attn: J. Furber
135 Shadow Brook Lane
Ben Lomond, CA 95005

Stone & Webster Engineering
Attn: Duncan Moodie
245 Summer Street
Boston, MA 02107

Strategies Unlimited
201 Sand Antonio Circle
Suite 205
Mountain View, CA 94040

TRW
Attn: Robert Patterson
One Space Park
Redondo Beach, CA 90278

United Energy Technologies
Attn: Noorul Reshamwala
420 Lincoln Center Dr.
Foster City, CA 94404

University of Chicago
Attn: Joseph O'Gallagher
5640 S. Ellis Avenue
Chicago, IL 60637

University of Delaware
Attn: Allen M. Barnett
Electrical Engineering Department
Newark, DE 19711

University of Wisconsin
Attn: Prof. J. D. Wiley
Dept. of Electrical Engineering
Madison, WI 53706

UNM/NMERI
Attn: G. Leigh
Campus Box 25
Albuquerque, NM 87131

Varian Associates (4)
Attn: C. Hamaker
N. Kaminar
G. Virshup
J. Werthen

611 Hansen Way K-219
Palo Alto, CA 94303

Wright Patterson AFB
Attn: Jack Geis
AFWAL/POOC
Wright Patterson AFB, OH

1140 P. Peercy
1142 H. Weaver
1150 J. Schirber
6200 V. Dugan
6220 D. Schueler
6221 E. Boes
6221 L. Beavis
6221 J. Cannon
6221 J. Chamberlin
6221 C. Chiang
6221 T. Kerschen
6221 A. Maish
6221 E. Richards
6221 C. Stillwell
6223 G. Jones
6223 W. Bower
6223 R. Chapman
6223 T. Key
6223 D. Menicucci
6223 H. Post
6223 J. Stevens
6223 M. Thomas
6224 D. Arvizu
6224 P. Basore
6224 J. Gee (10)
6224 D. King
6224 D. Ruby
3141 S. A. Landenberger (5)
3151 W. L. Garner (3)
3154-3 C. H. Dalin (28)
For DOE/TIC
(Unlimited Release)
8024 P. W. Dean